



# Prediction of properties and optimal design of microstructure of multi-phase and multi-layer C/SiC composites

Yingjie Xu

## ► To cite this version:

Yingjie Xu. Prediction of properties and optimal design of microstructure of multi-phase and multi-layer C/SiC composites. Other. Université de Technologie de Belfort-Montbéliard; Northwestern Polytechnical University (China), 2011. English. NNT: 2011BELF0158 . tel-00625953

**HAL Id: tel-00625953**

**<https://theses.hal.science/tel-00625953>**

Submitted on 23 Sep 2011

**HAL** is a multi-disciplinary open access archive for the deposit and dissemination of scientific research documents, whether they are published or not. The documents may come from teaching and research institutions in France or abroad, or from public or private research centers.

L'archive ouverte pluridisciplinaire **HAL**, est destinée au dépôt et à la diffusion de documents scientifiques de niveau recherche, publiés ou non, émanant des établissements d'enseignement et de recherche français ou étrangers, des laboratoires publics ou privés.

Université de Technologie de Belfort-Montbéliard – UTBM

Ecole doctorale Science Pour l'Ingénieur et Microtechnique – SPIM

## **THESE en co-tutelle internationale UTBM-NPU**

Pour obtenir le grade de

### **DOCTEUR**

SPECIALITE: MECANIQUE ET CONCEPTION

## **Prediction of properties and optimal design of microstructure of multi-phase and multi-layer C/SiC composites**

Présentée et soutenue publiquement par

**Yingjie XU**

Le 08 juillet 2011 devant le jury d'examen :

Rapporteurs: **Pierre DUYSINX**, Professeur, Université de Liège, Belgique  
**Pascal LARDEUR**, ECC HDR, Université de Technologie de Compiègne, France

Examineurs: **Jan G. KORVINK**, Professeur, Université de Freiburg, Allemagne  
**Matthieu DOMASZEWSKI**, Professeur, Université de Technologie de Belfort-Montbéliard, co-directeur de thèse, France  
**Weihong ZHANG**, Professeur, Northwestern Polytechnical University, co-directeur de thèse, Chine  
**Dominique CHAMORET**, Maître de Conférences, Université de Technologie de Belfort-Montbéliard, France

# **Acknowledgements**

Firstly, I would like to thank my supervisors, Professor Matthieu Domaszewski, Professor Weihong Zhang and Dr. Dominique Chamoret for their guidance, patience and outstanding support throughout my doctoral studies.

The General Council of Territory of Belfort and China Scholarship Council are gratefully acknowledged for financially supporting my studies in France.

I would also like to extend my gratitude to the staff of laboratory M3M in UTBM and Laboratory of Engineering Simulation and Aerospace Computing in NPU who have offered their time and help over the years.

Finally, I want to thank my family and all my friends who have supported and encouraged me throughout my studies.

# **Abstract**

Carbon fiber-reinforced silicon carbide matrix (C/SiC) composite is a ceramic matrix composite (CMC) that has considerable promise for use in high-temperature structural applications. In this thesis, systematic numerical studies including the prediction of elastic and thermal properties, analysis and optimization of stresses and simulation of high-temperature oxidations are presented for the investigation of C/SiC composites.

A strain energy method is firstly proposed for the prediction of the effective elastic constants and coefficients of thermal expansion (CTEs) of 3D orthotropic composite materials. This method derives the effective elastic tensors and CTEs by analyzing the relationship between the strain energy of the microstructure and that of the homogenized equivalent model under specific thermo-elastic boundary conditions. Different kinds of composites are tested to validate the model.

Geometrical configurations of the representative volume cell (RVC) of 2-D woven and 3-D braided C/SiC composites are analyzed in details. The finite element models of 2-D woven and 3-D braided C/SiC composites are then established and combined with the strain energy method to evaluate the effective elastic constants and CTEs of these composites. Numerical results obtained by the proposed model are then compared with the results measured experimentally.

A global/local analysis strategy is developed for the determination of the detailed stresses in the 2-D woven C/SiC composite structures. On the basis of the finite element analysis, the procedure is carried out sequentially from the homogenized composite structure of the macro-scale (global model) to the parameterized detailed fiber tow model of the micro-scale (local model). The bridge between two scales is realized by mapping the global analysis result as the boundary conditions of the local tow model. The stress results by global/local method are finally compared to those by conventional finite element analyses.

Optimal design for minimizing thermal residual stress (TRS) in 1-D unidirectional C/SiC composites is studied. The finite element models of RVC of 1-D unidirectional C/SiC

composites with multi-layer interfaces are generated and finite element analysis is realized to determine the TRS distributions. An optimization scheme which combines a modified Particle Swarm Optimization (PSO) algorithm and the finite element analysis is used to reduce the TRS in the C/SiC composites by controlling the multi-layer interfaces thicknesses.

A numerical model is finally developed to study the microstructure oxidation process and the degradation of elastic properties of 2-D woven C/SiC composites exposed to air oxidizing environments at intermediate temperature ( $T < 900^{\circ}\text{C}$ ). The oxidized RVC microstructure is modeled based on the oxidation kinetics analysis. The strain energy method is then combined with the finite element model of oxidized RVC to predict the elastic properties of composites. The environmental parameters, i.e., temperature and pressure are studied to show their influences upon the oxidation behavior of C/SiC composites.

**Keywords:** C/SiC composites; Finite element method; Strain energy method; Microstructure modelling; Stress analysis; Optimization (Particle Swarm Optimization); Oxidation

# Résumé

Les matériaux composites à matrice de carbure de silicium renforcée par des fibres de carbone (C/SiC) sont des composites à matrice céramique (CMC), très prometteurs pour des applications à haute température, comme le secteur aéronautique. Dans cette thèse, sont menées des études particulières concernant les propriétés de ces matériaux : prédiction des propriétés mécanique (élastiques), analyses thermiques (optimisation des contraintes thermiques), simulation de l'oxydation à haute température.

Une méthode basée sur l'énergie de déformation est proposée pour la prédiction des constantes élastiques et des coefficients de dilatation thermiques de matériaux composites orthotropes 3D. Dans cette méthode, les constantes élastiques et les coefficients de dilatation thermique sont obtenus en analysant la relation entre l'énergie de déformation de la microstructure et celle du modèle homogénéisé équivalent sous certaines conditions aux limites thermiques et élastiques. Différents types de matériaux composites sont testés pour valider le modèle.

Différentes configurations géométriques du volume élémentaire représentatif des composites C/SiC (2D tissés et 3D tressés) sont analysées en détail. Pour ce faire, la méthode énergétique a été couplée à une analyse éléments finis. Des modèles EF des composites C/SiC ont été développés et liés à cette méthode énergétique pour évaluer les constantes élastiques et les coefficients de dilatation thermique. Pour valider la modélisation proposée, les résultats numériques sont ensuite comparés à des résultats expérimentaux.

Pour poursuivre cette analyse, une nouvelle stratégie d'analyse « globale/locale » (multi-échelle) est développée pour la détermination détaillée des contraintes dans les structures composites 2D tissés C/SiC. Sur la base de l'analyse par éléments finis, la procédure effectue un passage de la structure composite homogénéisée (Echelle macro : modèle global) au modèle détaillé de la fibre (Echelle micro : modèle local). Ce passage entre les deux échelles est réalisé à partir des résultats de l'analyse globale et des conditions aux limites du modèle local. Les contraintes obtenues via cette approche sont ensuite comparées à celles obtenues à l'aide d'une analyse EF classique.

La prise des contraintes résiduelles thermiques (contraintes d'origine thermique dans les fibres et la matrice) joue un rôle majeur dans le comportement des composites à matrices céramiques. Leurs valeurs influencent fortement la contrainte de microfissuration de la matrice. Dans cette thèse, on cherche donc à minimiser cette contrainte résiduelle thermique (TRS) par une méthode d'optimisation de type métaheuristique: Particle Swarm Optimization (PSO), Optimisation par essaims particuliers.

Des modèles éléments finis du volume élémentaire représentatif de composites 1-D unidirectionnels C/SiC avec des interfaces multi-couches sont générés et une analyse par éléments finis est réalisée afin de déterminer les contraintes résiduelles thermiques. Un schéma d'optimisation couple l'algorithme PSO avec la MEF pour réduire les contraintes résiduelles thermiques dans les composites C/SiC en optimisant les épaisseurs des interfaces multi-couches.

Un modèle numérique est développé pour étudier le processus d'oxydation de microstructure et la dégradation des propriétés élastiques de composites 2-D tissés C/SiC oxydant à température intermédiaire ( $T < 900^{\circ}\text{C}$ ). La microstructure du volume élémentaire représentatif de composite oxydé est modélisée sur la base de la cinétique d'oxydation. La méthode de l'énergie de déformation est ensuite appliquée au modèle éléments finis de la microstructure oxydé pour prédire les propriétés élastiques des composites. Les paramètres d'environnement, à savoir, la température et la pression, sont étudiées pour voir leurs influences sur le comportement d'oxydation de composites C/SiC.

**Mots clés:** Composites C/SiC; Modélisation éléments finis; Méthode de l'énergie de déformation; Modélisation de la microstructure; Analyse des contraintes; Optimisation (Particle Swarm Optimization); Oxydation.

## LIST OF FIGURES

Figure 1.1 SEM photograph of a C/SiC composite with multi-layer interfaces .....	2
Figure 1.2 SEM photograph of a C/SiC composite with multi-layer interfaces and matrices .....	2
Figure 2.1 Illustration of the RVC of composite .....	16
Figure 2.2 RVC under boundary condition 1 .....	22
Figure 2.3 RVC under boundary condition 2 .....	22
Figure 2.4 RVC under boundary condition 3 .....	22
Figure 2.5 RVC under boundary condition 4 .....	24
Figure 2.6 Homogenized equivalent model under boundary condition 1 .....	25
Figure 2.7 Homogenized equivalent model under boundary condition 5 .....	25
Figure 2.8 RVC under boundary condition 5 .....	26
Figure 2.9 RVC under boundary condition 6 .....	26
Figure 2.10 RVC under boundary condition 7 .....	27
Figure 2.11 Finite element model of the RVC for unidirectional composite .....	29
Figure 2.12 Longitudinal CTE of E-glass/epoxy unidirectional composite .....	31
Figure 2.13 Transverse CTE of E-glass/epoxy unidirectional composite .....	31
Figure 2.14 1/8 finite element model of the RVC for spherical porous alumina .....	32
Figure 2.15 Finite element model of the RVC for plain weave laminate composite .....	33
Figure 3.1 Illustration of the fabrication procedure of C/SiC composites .....	36
Figure 3.2 Geometric model of RVC of 2-D woven C/SiC composite on the fiber scale .....	37
Figure 3.3 SEM photograph of the 2-D plain woven perform .....	40
Figure 3.4 Schematic representation of the 2-D plain woven perform .....	40
Figure 3.5 Geometric model of RVC of 2-D woven C/SiC composite on the tow scale .....	41
Figure 3.6 Finite element model of RVC of 2-D woven C/SiC composite on the tow scale .....	43
Figure 3.7 Z-directional cross-section of the 3-D 4-step braided C/SiC composite .....	45
Figure 3.8 Division of the “Analysis unit” .....	46
Figure 3.9 Geometry of “Analysis unit” .....	46
Figure 3.10 Geometrical model of RVC of 3-D braided C/SiC composite on the tow scale .....	48
Figure 3.11 Finite element model of RVC of 3-D braided C/SiC composite on the tow scale .....	51
Figure 3.12 Illustration of the two-level evaluation procedure .....	52
Figure 3.13 Finite element models of RVCs of composite A .....	54
Figure 3.14 Finite element models of RVCs of composite B .....	55
Figure 3.15 Finite element models of RVCs of composite C .....	57
Figure 3.16 Finite element models of RVCs of composite D .....	58
Figure 3.17 Finite element models of RVCs of composite E .....	61
Figure 3.18 Finite element models of RVCs of composite F .....	62
Figure 4.1 Global/local model of a composite structure .....	67
Figure 4.2 Global/local stress analysis procedure of 2-D woven C/SiC laminate panel structure .....	69
Figure 4.3 Homogenized finite element model of the laminate panel .....	69
Figure 4.4 Local model and global/local interface .....	70
Figure 4.5 Illustration of bilinear interpolation .....	71
Figure 4.6 Global and local models of 2-D woven C/SiC laminate panel .....	73
Figure 4.7 RVC models of the 2-D woven C/SiC composite .....	74
Figure 4.8 Reference finite element model of the 2-D woven C/SiC laminate panel .....	77
Figure 4.9 Convergence of the maximum stresses within the tows .....	77



Figure 4.10 von Mises stress distributions over the tows .....	80
Figure 4.11 von Mises stress distributions over the first layer of matrix .....	81
Figure 4.12 von Mises stress distributions over the second layer of matrix .....	81
Figure 5.1 Transverse cross-section of the 1-D unidirectional C/SiC composites.....	85
Figure 5.2 RVC model of the 1-D unidirectional C/SiC composites .....	86
Figure 5.3 Finite element model of the RVC of C/MoSi <sub>2</sub> /SiC composite.....	87
Figure 5.4 Residual radial thermal stresses distribution for RVC model of SiC/MoSi <sub>2</sub> /SiC .....	89
Figure 5.5 Computed residual radial thermal stress and the results of cylinder model.....	89
Figure 5.6 Illustration of the variable limits handling strategy .....	95
Figure 5.7 Convergence rate for the optimization of hoop TRS .....	97
Figure 5.8 Iterations of the design variables for the case 1 .....	98
Figure 5.9 Convergence rate for the optimization of radial TRS .....	99
Figure 5.10 Iterations of the design variables for the case 2 .....	99
Figure 5.11 Convergence rate for the optimization of axial TRS .....	100
Figure 5.12 Iterations of the design variables for the case 3 .....	101
Figure 6.1 Geometry of the RVC microstructure with cracks of 2-D woven C/SiC composites .....	106
Figure 6.2 The schematic representation of the oxidation of 2-D C/SiC composite.....	108
Figure 6.3 The computational model of the reaction rate constant of carbon fiber .....	110
Figure 6.4 The void contour formed within the interface .....	112
Figure 6.5 Computed oxidation void contours at different instants .....	115
Figure 6.6 Morphologies of fiber scale RVC at different oxidation time .....	116
Figure 6.7 Illustration of the two-level evaluation procedure.....	117
Figure 6.8 Elastic modulus versus oxidation time .....	119
Figure 6.9 Elastic modulus versus temperature .....	120
Figure 6.10 Elastic modulus versus pressure .....	120

# LIST OF TABLES

Table 2.1 Boundary conditions of the RVC .....	18
Table 2.2 Comparison of computed longitudinal modulus with experimental and numerical results .....	30
Table 2.3 Properties of the constituents .....	30
Table 2.4 Computed CTE of the spherical porous alumina with different porous ratio .....	32
Table 2.5 Properties of E-glass/epoxy tow and epoxy matrix .....	33
Table 2.6 Comparison of computed results with experimental and numerical results .....	34
Table 3.1 RVC models with different characteristic parameters on the fiber scale .....	39
Table 3.2 Engineering moduli data for each material phase .....	53
Table 3.3 Effective elastic tensors evaluated on two scales of composite A .....	54
Table 3.4 Evaluated elastic moduli for composite A .....	55
Table 3.5 Effective elastic tensors evaluated on two scales of composite B .....	56
Table 3.6 Evaluated elastic moduli for composite B .....	56
Table 3.7 Effective elastic tensors evaluated on two scales of composite C .....	57
Table 3.8 Evaluated elastic moduli for composite C .....	58
Table 3.9 Effective elastic tensors evaluated on two scales of composite D .....	59
Table 3.10 Evaluated elastic moduli for composite D .....	59
Table 3.11 Properties of the constituents under various temperatures .....	60
Table 3.12 Computed CTEs of composite E under various temperatures .....	61
Table 3.13 Computed CTEs of composite F under various temperatures .....	62
Table 3.14 Comparison of computed moduli with experimental results [87] .....	63
Table 3.15 Comparison of computed CTEs with experimental results [53] .....	63
Table 4.1 Engineering modulus data for each material phase .....	75
Table 4.2 Effective elastic moduli of tow .....	75
Table 4.3 Effective elastic moduli of composite .....	76
Table 4.4 Number of elements and value of $RATIO_{GL}$ for each global grid .....	76
Table 4.5 Comparison of the CPU time (seconds) .....	78
Table 4.6 Peak stresses of global/local solution and reference solution .....	78
Table 5.1 Properties of the constituents .....	87
Table 5.2 Comparison of numerical results with experimental ones .....	88
Table 5.3 The pseudo-code for the present PSO algorithm .....	96
Table 6.1 Material constant values used for the numerical simulation .....	118
Table 6.2 Geometrical parameters of the RVC before oxidation .....	118

# CONTENTS

<b>Chapter 1: Introduction .....</b>	<b>1</b>
1.1 C/SiC composite .....	1
1.2 Numerical modelling of the properties of composite materials .....	2
1.2.1 Closed-form analytical methods .....	3
1.2.2 Finite element based methods.....	5
1.3 Investigation of C/SiC composites .....	6
1.3.1 Analysis of the mechanical and thermal properties of C/SiC composites.....	6
1.3.2 Study of the oxidation behaviors of C/SiC composites .....	9
1.4 Objective and outline of the thesis .....	11
<b>Chapter 2: Strain energy method for the prediction of the elastic/thermal properties of composite materials .....</b>	<b>14</b>
2.1 Introduction .....	14
2.2 Theory of strain energy method .....	15
2.2.1 Prediction of the effective elastic properties .....	17
2.2.2 Prediction of the effective CTEs .....	21
2.3 Numerical examples .....	29
2.3.1 Prediction of elastic modulus of unidirectional composite .....	29
2.3.2 Prediction of CTEs of unidirectional composite .....	30
2.3.3 Prediction of CTEs of spherical porous material.....	31
2.3.4 Prediction of elastic modulus and CTEs of woven composite .....	32
2.4 Conclusions .....	34
<b>Chapter 3: Microstructure modelling and prediction of effective properties of woven and braided C/SiC composites.....</b>	<b>35</b>
3.1 Introduction .....	35
3.2 Microstructure modelling of 2-D woven C/SiC composites.....	37
3.2.1 Fiber scale.....	37
3.2.2 Tow scale .....	39
3.3 Microstructure modelling of 3-D braided C/SiC composites .....	43
3.3.1 Fiber scale.....	43
3.3.2 Tow scale .....	43
3.4 Prediction of the effective properties and comparison with experimental results ..	51
3.4.1 Two level evaluation strategy .....	51
3.4.2 Prediction of the effective elastic moduli .....	53
3.4.2.1 Composite A .....	53
3.4.2.2 Composite B .....	55
3.4.2.3 Composite C .....	56

3.4.2.4 Composite D .....	58
3.4.3 Prediction of the effective CTEs .....	59
3.4.3.1 Composite E.....	60
3.4.3.2 Composite F.....	61
3.4.4 Comparison with the experimental results .....	62
3.5 Conclusions .....	64
<b>Chapter 4: Stress analysis of C/SiC composite structures using global/local approach .....</b>	<b>65</b>
4.1 Introduction .....	65
4.2 Basis of global/local stress analysis .....	66
4.2.1 Global analysis.....	67
4.2.2 Global/local interface boundary definition .....	67
4.2.3 Global/local interpolation.....	68
4.2.4 Local analysis.....	68
4.3 Global/local stress analysis strategy for 2-D woven C/SiC laminate panel structure.....	68
4.4 Numerical tests.....	72
4.4.1 Problem description .....	72
4.4.2 Evaluation of the elastic properties of the composite.....	75
4.4.3 Stress analysis results.....	76
4.5 Conclusions .....	81
<b>Chapter 5: Minimizing thermal residual stresses of C/SiC composites by using particle swarm optimization algorithm .....</b>	<b>83</b>
5.1 Introduction .....	83
5.2 Finite element analysis of TRS .....	84
5.2.1 Finite element model .....	84
5.2.2 Numerical tests .....	86
5.3 Optimization problem .....	89
5.4 Particle swarm optimization algorithm.....	90
5.4.1 Basis of particle swarm optimization algorithm .....	90
5.4.2 Parameter selection .....	92
5.4.2.1 The number of particles.....	92
5.4.2.2 The acceleration constants.....	92
5.4.2.3 The inertia weight.....	92
5.4.2.4 The termination condition .....	93
5.4.3 Variable limits handling strategy.....	93
5.4.4 Algorithm description .....	95
5.5 Results and discussion .....	96
5.5.1 Case 1: Minimization of the maximum hoop TRS .....	97
5.5.2 Case 2: Minimization of the maximum radial TRS .....	98

5.5.3 Case 3: Minimization of the maximum axial TRS.....	99
5.6 Conclusions .....	101
<b>Chapter 6: Numerical simulation of the oxidation of C/SiC composites exposed to intermediate temperature oxidizing environments .....</b>	<b>103</b>
6.1 Introduction .....	103
6.2 Modelling of the microstructure with cracks of 2-D woven C/SiC composites .....	105
6.3 Modelling of the microstructure of oxidized 2-D woven C/SiC composites .....	107
6.3.1 Determination of oxidation rates of carbon phases.....	108
6.3.2 Determination of oxidation void contour .....	111
6.3.2.1 <i>Modelling of the oxidation void contour in interface</i> .....	111
6.3.2.2 <i>Modelling of the oxidation void in fiber</i> .....	113
6.3.3 Numerical simulation of oxidized microstructure morphology .....	114
6.4 Two-level evaluation strategy of the degraded elastic properties .....	116
6.5 Numerical examples .....	118
6.5.1 Comparison with experimental results.....	118
6.5.2 Influence of temperature and pressure.....	119
6.6 Conclusions .....	121
<b>Chapter 7: Conclusions and future works .....</b>	<b>122</b>
7.1 Conclusions .....	122
7.2 Future works .....	124
<b>References.....</b>	<b>126</b>
<b>Scientific Publications .....</b>	<b>137</b>

# Chapter 1: Introduction

## 1.1 C/SiC composite

Carbon fiber reinforced silicon carbide matrix (C/SiC) composite is a ceramic matrix composite (CMC) material that has considerable promise for use in high-temperature structural applications. The applications proposed in this report are concerned primarily in aerospace and include nozzles, nozzle ramps, leading edges, thermal protection systems, thrusters, turbines, and body flaps [1-7]. Some applications not specific to aerospace technologies include brakes, heat shields, outer flaps of turbojet engines, and hot gas path components [8-10]. The main interest of C/SiC composites compared to super alloy concern their material properties. Indeed, the beneficial material properties of C/SiC composites, compared with those of super alloys, include higher strength to density ratio, lighter weight, higher temperature capability, and improved thermal shock resistance. Besides, compared with carbon fiber reinforced carbon matrix (C/C) composites, the oxidation resistance of C/SiC composites is greatly improved due to the protection of the non-oxide silicon carbide (SiC) matrix.

Typically, a C/SiC composite consists of following multi-phase material constitutes: carbon fiber, pyrolytic carbon (PyC) interface and SiC matrix. Especially as the interface or the matrix is composed of multi-layered alternate PyC and SiC phases, a distinct multi-phase materials distribution can be observed within C/SiC composites. The multi-layered spatial architectures and the multi-phase materials distribution in the interface and matrix have several key functions including crack deflection, load transfer and stress relaxation [11-12], which could partially prevent the crack propagation in the interface and matrix and hence improve the toughness of C/SiC composites. Figure 1.1 shows the scanning electron microscope (SEM) photograph of a C/SiC composite with multi-layered interfaces [13]. It can be observed that multi-layered alternate PyC and SiC interfaces are distributed between the fiber and matrix. Figure 1.2 shows the SEM photograph of a C/SiC composite with multi-layered interfaces and matrices [14]. The interface and matrix of the composite are both

composed of alternate SiC (white color) and PyC (black color) phases. As shown in Figure 1.2, the multi-layered matrices are distributed around the tows. Within the tows, the multi-layered interfaces are distributed around the fibers.

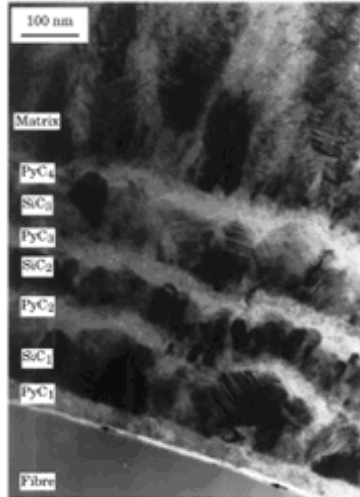


Figure 1.1 SEM photograph of a C/SiC composite with multi-layer interfaces

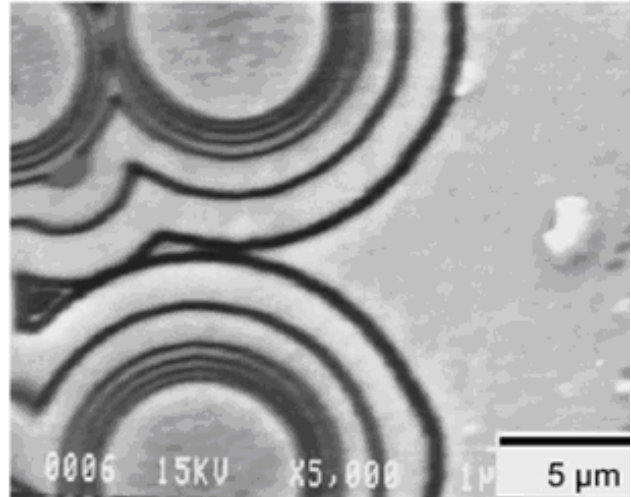


Figure 1.2 SEM photograph of a C/SiC composite with multi-layer interfaces and matrices

## 1.2 Numerical modelling of the properties of composite materials

Complicated spatial architecture and material heterogeneity are basic characteristics of composite materials constituting the challenge to understand their physical and mechanical behaviors. Discovery of the intrinsic relations between the effective properties and the complex materials microstructure is thus the key for practical applications of composites and development of advanced materials. With rapidly growing computational modeling capability, the numerical analysis has become an important means of understanding the behavior of composite materials. An appropriately introduced representative volume cell (RVC) or unit cell that captures the major features of the underlying composite microstructure is usually the first step into such an analysis.

The two most popularly employed fiber reinforced composites in modern engineering applications are 2-D woven and 3-D braided composites. Such composites have received a great amount of consideration in the literature, and much exists in the way of modelling the

complicated woven/braided composites microstructure, predicting the elastic moduli, strength, thermal properties, and stress analysis techniques. However, these studies are generally applied for the traditional polymer and metal matrix composites and do not capture the unique characteristics of C/SiC composites, such as the multi-layered spatial architectures and the multi-phase materials distribution in the C/SiC composites with multi-layered interfaces or matrices.

Numerical methods currently available in the literature for predicting the effective properties of 2-D woven and 3-D braided composites may be considered as belonging to two groups: closed-form analytical methods and finite element based methods.

### **1.2.1 Closed-form analytical methods**

Closed-form analytical methods are based on the closed-form solution of mathematical models applied to very simplified RVC models. These methods are computationally efficient but not readily applicable to obtain an accurate detailed stress/strain field of the composite due to their inherent limitation in accurately modelling the composite microstructure. The representative closed-form analytical methods for 2-D woven composites include mainly the laminate theory-based model and the cells method. Fiber inclination model, fabric geometry model and volume averaging model are the typical closed-form analytical methods used for 3-D braided composites.

In the 1980s, Ishikawa and Chou [15-19] firstly presented three analytical models for the stiffness and strength investigation of 2-D woven composites based on the classical laminate theory: mosaic model, fiber undulation model and bridging model. Mosaic model treated the woven composite as an assemblage of asymmetric cross-ply laminates. Fiber undulation model was developed based on the mosaic model and considered the undulation and continuity characteristics of the fibers in woven composites which were omitted in the mosaic model. However, fiber undulation model took into account fiber continuity and undulation only in the fill direction but ignored the warp direction. Bridging model broke up the RVC model into interlaced regions, whose in-plane stiffness was predicted by fiber undulation model, and non-interlaced regions, which were modeled as cross-ply laminates. Based on the



fiber undulation model, Scida et al. [20] proposed a laminate theory-based analytical model which considered the fiber continuity and undulation in both the fill and warp directions to predict the elastic and failure properties of woven composites.

Tabiei and Jiang [21-23], Tanov and Tabiei [24-25] developed cells method to predict the properties of 2-D woven composites. Within the model, a representative volume cell was assumed. Using the iso-stress and iso-strain assumptions the constitutive equations were averaged along the thickness direction. The cell was then divided into many subcells and an averaging was performed again by assuming uniform stress distribution in each subcell to obtain the effective stress-strain relations of the subcell. Then these relations were combined to get the effective stresses and strains in the whole cell.

Yang et al. [26] proposed the fiber inclination model based on a modified laminate theory to predict the elastic properties of 3-D braided composites. The unit cell used for the analysis was assumed to be composed of an assemblage of inclined unidirectional laminate. The idealized unit cell was described as fiber bundles oriented in four body diagonal directions. All the yarns in one direction were assumed to form inclined laminate after matrix impregnation. The rest of the analysis was explained as an extension of the fiber undulation model developed by Ishikawa and Chou [16]. In this analysis, contributions of pure matrix regions to the stiffness matrices were neglected. Sun and Qiao [27] developed and extended this fiber inclination model to analyze the strength properties of 3-D braided composites.

Whyte [28] proposed the fabric geometry model based on a modified laminate theory to predict the properties of 3-D braided composites. This model considered the fibers and matrix as a group of rectilinear bars with various spatial orientations. Once the whole group of bars had been characterized, the composite global stiffness matrix, therefore all the elastic constants, were obtained by adding the contributions of single bars that should have transverse isotropy. In the calculation of axial stiffness, some errors were found for small braiding angle values.

The volume averaging model [29-30] used a weighted average of the results obtained with the fabric geometry model. After the group of bars had been characterized, according to the fabric geometry model, the stiffness matrix was obtained as a weighted average of the single beam contributions to global stiffness, where the weights used were the volume fractions of

every beam. The weights might appropriately be defined to take into account tow cross-sectional characteristics. They were completely ignored in the fabric geometry model.

### **1.2.2 Finite element based methods**

Finite element based methods involve the use of the 3-D finite element method to analyze the mechanical and thermal behavior and determine the effective properties of woven and braided composites. In general, finite element based methods require the development of a detailed RVC model that truly takes into account the microstructural architecture of the composite. Since a detailed RVC finite element model usually involves thousands of elements, finite element based methods are computationally costly compared with closed-form analytical methods. The advantage of finite element based methods is their ability in predicting the detailed stress/strain fields of composites especially the woven/braided composites with complex microstructures. Two types of finite element based methods are mainly used in literature: direct finite element analysis under the specified displacement boundary conditions, and homogenization method combined with finite element analysis.

The direct finite element analysis has been extensively used to determine the mechanical properties of woven and braided composites [31-36]. In such an approach, a finite model of the RVC which took into account the periodical microstructure of the composite and truly simulated the spatial configuration of the tows and matrix was firstly established. The periodical displacement boundary conditions were then imposed on the finite element model in order to satisfy forces continuity and displacements compatibility on the opposite faces of the RVC. The specified displacement boundary conditions, such as the tensile and shear displacements, were imposed in the finite element model. The properties of the composites were finally determined by the finite element analysis results of the stresses and strains of the RVC model. Based on the direct finite element analysis, Srirengan and Whitcomb [37-38] proposed a global/local technique to determine the detailed stress field of a 2-D woven composite. The analysis was carried out in two stages: a global analysis was performed using only a few elements to discretize an entire material. Homogenized material properties obtained via the direct finite element analysis were used which macroscopically account for

the heterogeneity in the material. To obtain detailed stress distribution, a local analysis was performed which accounts for the tows and the matrix discretely.

Homogenization method is based on the mathematical theory of two-scale asymptotic expansion [39]. Concerning the composite with periodic microstructure, the two scales are a macroscale representing the composite structure and a microscale representing the periodic microstructure in the heterogeneous composite. The homogenization process uses asymptotic techniques to express the macroscopic variations of dependent variables in terms of the microscale variations of the geometric and material variables. This transforms the governing differential equation into a series of coupled boundary value problems of successively higher orders, defined in the microscale [40-41]. The solution of each successive boundary value problem acts as a non-homogeneous term in the next higher order boundary value problem. The boundary conditions of the RVC are determined from periodicity and loading conditions. This technique combined with finite element analysis has been exploited by many researchers for obtaining accurate effective (macroscale) properties of woven and braided composites. Dasgupta et al. [42] calculated effective thermo-mechanical and thermal properties of woven composites. Carvelli and Poggi [43] investigated the macroscopic mechanical behavior of woven composites. Two levels of homogenization were performed in their study. The homogenization theory was firstly applied to the tows considered as unidirectional fiber reinforced composites, then to the woven composites with homogenized tows. Feng and Wu [44] used this method to predict the effective modulus of 3-D braided composites. Dong and Feng [45] conducted the numerical predictions of the tensile strength of 3-D braided composites.

## **1.3 Investigation of C/SiC composites**

### **1.3.1 Analysis of the mechanical and thermal properties of C/SiC composites**

C/SiC composite technologies are being developed and advanced with the notion that they will find widespread use in the high-temperature structural applications especially in the

aerospace industries. However, since C/SiC composite is still a relatively new class of materials, characterization studies of the properties of C/SiC composites have been limited compared to such materials as polymer and metal matrix composites. Future C/SiC composite structures will possess rather complex shapes requiring various architectures, variations in local thickness, and local curvature, which may also lead to processing non-uniformities throughout a given structure. Needless to say, in order to design such composite structures, the mechanical and thermal expansion properties of C/SiC composites need to be well understood.

A considerable amount of experimental researches have been done on the mechanical and thermal behaviors of C/SiC composites. Camus et al. [46] investigated the mechanical responses of 2-D woven C/SiC composites subjected to uniaxial tensile and compressive loadings. An extended non-linear stress-strain response and a multi-stage development of damage involving transverse matrix microcracking, bundle/matrix and inter-bundle debonding as well as thermal residual stress release were evidenced.

Bouazzaoui et al. [47] used an ultrasonic method to investigate the non-linear mechanical behavior of 2-D woven C/SiC composites. Two damage modes were emphasized that transverse microcracks were characterized by a deterministic accumulation and a random development of longitudinal micro cracking, i.e. fiber/matrix and bundle/matrix debonding.

Inghels and Lamon [48-49] carried out experimental studies at room temperature to investigate the mechanical behaviors of a 2-D woven C/SiC composite. The tensile and bending tests of the specimen permitted the identification of the damaging process in C/SiC composite. The analysis of the mechanical behavior considered separately the reversible behaviour, which is the response of the material to a loading, and the residual behaviour resulting from mechanical damage.

Wang et al. [50] characterized the tensile behavior of a 2-D woven C/SiC composite by monotonic and loading/unloading tests. The quantitative analysis of the hysteresis behavior was performed in terms of constituent properties such as interfacial sliding stress and thermal residual stress between fibers and matrix. The composite showed markedly non-linear behavior with evident hysteresis loops, appreciable residual strains and continuously decreasing moduli.

Ji et al. [51] studied the loading-unloading properties of 3-D braided C/SiC composites at ambient temperature by three-point bending experiments with single-edge notch beam specimens. The loading-unloading displacement curves of 3-D C/SiC composites exhibited typically a non-linearity feature. A large residual displacement existed after unloading due to the pulling-out and incomplete recovery of the fiber and/or fiber bundles.

Cheng et al. [52] characterized the influence of the heat treatments on the thermal expansion behavior of C/SiC composites. The different expansion behavior of the composites was qualitatively analyzed before and after different heat treatments. It was indicated that the thermal expansion behavior of the composites was changed after heat treatment due to the increase of thermal stability and the change of thermal stress and microstructure of the materials.

Thermal expansion behavior of C/SiC composites with three different preform architectures including 1-D unidirectional, 2-D woven and 3-D braided C/SiC composites was investigated by Zhang et al [53] from room temperature to 1400 °C. The experimental results indicated that CTEs of 1-D unidirectional and 3-D braided C/SiC composites changed in a similar way due to the similar distribution of interfacial thermal stress and the same controlling factors in the same temperature ranges. Different behaviors were observed in the investigation of CTE of 2-D woven C/SiC composites.

Kumar et al. [54] investigated the thermal expansion behavior of 3-D stitched C/SiC composites. Coefficient of thermal expansion (CTE) of the composites was determined in in-plane and through-thickness directions in the temperature range from room temperature to 1050°C. An extensive microstructure study was also carried out to understand the thermal expansion behavior of the composites. It was found out that CTE behavior is closely related to the composition of the composite which, in turn, depends upon siliconization conditions.

Although the experimental studies have provided insight into the physics of mechanical and thermal expansion behaviors of C/SiC composites, the complexity, the time and cost associated with processing and testing C/SiC composites make it considerably cumbersome to characterize the material properties. Especially as designing the C/SiC composites structures, an efficient evaluation of the material properties is needed. Numerical modelling of the properties of C/SiC composite can control the properties in both a deterministic and

probabilistic manner and they can help to in better understanding the physical mechanisms, extending the material properties databases and efficient designing the composites structures. Owing to the fact that C/SiC composites have just been developed in recent decades, the numerical characterization study was quite limited [55-56]. Systematical studies of numerical modelling of the elastic and thermal expansion properties of C/SiC composites have not been discussed in literature yet.

### **1.3.2 Study of the oxidation behaviors of C/SiC composites**

The susceptibility of the carbon fibers and PyC interfaces to oxidation [57-59] has hindered the long-term reusable applications of C/SiC composites in high temperature oxidizing environments. Because the as-fabricated micro-cracks in the SiC matrix act as oxygen transport paths, the exposed carbon fibers and interfaces are susceptible to the oxidation, which leads to strength reduction and component failure. It is therefore necessary to assess the oxidation mechanisms and kinetics of C/SiC composites when exposed to severe service conditions.

Until now, much effort has been made to study the oxidation behavior of C/SiC composites. Understanding the oxidation mechanisms is the basis to broaden the applications as high temperature structure materials in oxidizing environments. Experimental researches showed that the oxidation kinetics of C/SiC composites can be divided into three domains [60-62]: at the low temperature range ( $T < 800^{\circ}\text{C}$ ), the rate of the reaction between carbon and oxygen dominates the oxidation kinetics and forms a uniform degradation of carbon reinforcement; at the intermediate temperature range ( $800^{\circ}\text{C} < T < 1100^{\circ}\text{C}$ ), the oxidation is dominated by gas diffusion through the matrix micro-cracks, resulting in a non-uniform degradation of carbon phases; at the high temperature range ( $T > 1100^{\circ}\text{C}$ ), because micro-cracks are sealed by the silicon dioxide and the oxidation is controlled by oxygen diffusion through the silicon dioxide, the oxidation mainly takes place on materials surfaces. Singh and Srivastava [63] investigated the effect of oxidation on elastic modulus of C/SiC composites with the exposure of oxy-acetylene gas flame in open atmosphere. The experimental results clearly indicated that the maximum tensile and elastic modulus of composites decreased with the oxidation time.

Note that the above experimental studies were all conducted in an unstressed state. However, the oxidation of the composite in unstressed and stressed states might be very different according to Halbig et al. [64-65]. They conducted the oxidation tests of C/SiC composites exposed to an external mechanical stress. The stressed oxidation results showed that the crack-closing effects were greatly diminished and the oxidation regime was similar to that of bare carbon fiber.

Due to the complexity, time consuming and experiment cost, various numerical oxidation models have been developed to study the physics of the oxidation process in C/SiC composites. Zhang et al. [66] developed a model to predict the oxidation behavior of ceramic-carbon composite based on the kinetic theory of gas diffusion and a linear parabolic oxidation process. Eckel et al. [67] proposed a similar model to determine the oxidation recession rate of a single carbon fiber embedded in a non-reactive matrix by simulating the diffusion of oxygen to the carbon fiber through a crack in the matrix. Halbig et al. [68-69] adopted Eckel's model to simulate the fiber surface recession in C/SiC specimens and presupposed the crack extension through the specimen gage section bridged by an array of continuous carbon fibers. Sullivan [70] developed a mathematical theory to predict the oxidation behavior of C/SiC composite structures, by assuming the C/SiC material was a homogeneous, orthotropic porous medium with a solid skeleton. The theory was derived from the mechanics of the flow of ideal gas through a porous solid. Although these oxidation models provide insight into the physics of oxidation of C/SiC composites, these approaches are mostly limited to the weight loss evaluation as well as the influence of environment on the weight loss behavior of composites. Vignoles et al. [71-73] modeled the behavior of a 3-D C/C composite during gaseous oxidation in steady state from the microscopic scale up to the macroscopic one. The geometrical morphologies of oxidized carbon components (fiber, interface and matrix) were modeled respectively based on a general model for receding surfaces under a first-order gasification process coupled to mass transfer by diffusion. This is the rare numerical study which investigates the oxidation behaviors of composites from the viewpoint of microstructural morphology modelling, although only the C/C composite is studied.

Concerning C/SiC composites, existing numerical approaches are not readily applicable to

model the complex morphology of oxidized material microstructures. Besides, these methods are unable to predict the degraded stiffness and strength of oxidized materials as a function of time and environment parameters. Especially as far as an accurate evaluation of degraded properties is concerned, an accurate modelling of the oxidized microstructure morphology and the efficient prediction of the degradation of material properties become a challenging topic.

## 1.4 Objective and outline of the thesis

The objective of this thesis is to present a systematic numerical study of C/SiC composites, which includes:

- The modelling of the complex microstructures with multi-layered spatial architectures and the multi-phase materials and prediction of the effective elastic and thermal properties of C/SiC composites.
- A detailed stress analysis of the C/SiC composite structures.
- The determination of the thermal residual stress (TRS) of C/SiC composites and the optimal design to minimize the TRS.
- A numerical simulation of the oxidation behavior of C/SiC composites in oxidizing environments.

The accurate and efficient predictive theory is required for the determination of thermo-elastic properties of C/SiC composites. In **Chapter 2**, a new finite element based method strain energy method is developed for the prediction of the effective elastic constants and coefficient of thermal expansion (CTE) of composite materials. This model is based on the relationship established between the strain energy of the microstructure and that of the homogenized equivalent model under specific thermo-elastic boundary conditions. Different kinds of composites are tested to validate the model.

**Chapter 3** studies the microstructure modeling technique and the evaluation of effective elastic constants and CTEs of C/SiC composites. The 2-D woven and 3-D braided C/SiC composites which are widely used in engineering are concerned in this chapter. In order to extend the application of the modeling technique, the most complicated condition, i.e. the



modeling of composites with multi-layered interfaces and matrices is studied. The geometrical configurations of the RVC microstructure of composites are analyzed and mathematical relations among different geometrical parameters are derived. Based on the above analysis, the finite element models of 2-D woven and 3-D braided C/SiC composites are established and combined with the strain energy method, respectively to evaluate the effective elastic constants and CTEs of composites. Numerical results obtained by the proposed model are then compared with the results measured experimentally.

An accurate detailed stress analysis is essential for designing the C/SiC composite structures. The finite element method is a common tool for the detailed stress analysis. However, the conventional finite element analysis is computationally challenging due to the complex architecture of the multi-phase and multi-layered microstructure of C/SiC composites. An effective global/local analysis strategy is employed to determine local stresses in the C/SiC composite structures in **Chapter 4**. On the basis of the finite element analysis, the procedure is carried out sequentially from the homogenized composite structure of the macro-scale to the parameterized detailed fiber tow model of the micro-scale. The bridge between two scales is realized by mapping the global analysis result as the boundary conditions of the local tow model and hence the influence of the global model refinement on the computing accuracy of local stress is particularly addressed. To verify the computing results of such a bottom-up global/local analysis, we use a refined finite element mesh of the composite structure whose solution is considered as the standard of comparison. The proposed approach is finally applied to a 2-D woven C/SiC composite panel.

The thermal residual stresses (TRS) induced in C/SiC composites with multi-layered interfaces or matrices when cooling down from the processing temperature, have a significant influence on the mechanical behavior and lifetime of composites. To achieve an excellent thermal-mechanical performance of C/SiC composites, it is necessary to analyze and design the microstructure for an optimized TRS distribution. Such a study is presented in **Chapter 5** by synergizing finite element analysis and a particle swarm optimization (PSO) algorithm.

The oxidation behavior of C/SiC composites in oxidizing environments is simulated by modeling the oxidized microstructure morphology and predicting the degraded elastic properties in **Chapter 6**. The oxidized RVC microstructure is firstly modeled based on the

oxidation kinetics analysis and compared with the experimentally observed morphology. The strain energy method is then combined with the oxidized RVC microstructure modeling technique to predict the elastic properties of a C/SiC composite in air oxidizing environment. The evaluated results are validated in comparison to experimental data presented in literature. Moreover, the environmental parameters, i.e., temperature and pressure are studied to show their influences upon the oxidation behavior of C/SiC composites.

Final conclusions of the work and recommendations for future investigation are made in

**Chapter 7.**

## **Chapter 2: Strain energy method for the prediction of the elastic/thermal properties of composite materials**

### **2.1 Introduction**

Elastic properties and coefficients of thermal expansion are important physical properties of composite materials used in high-temperature environment. The exact prediction of these effective properties is essential to design the composite materials and understand the mechanical and thermal behaviors. Generally, two approaches are taken into account to obtain the global effective properties of composite materials: (a) experimental modelling and (b) numerical modelling. The experimental modelling utilizes the experimental data from standard coupon specimens to build a constitutive equation [74]. The numerical modeling typically uses the representative volume cell (RVC) or unit cell technique combined with the known material properties of fiber and matrix to determine the overall behavior of the composite [75-76]. The experimental program required to evaluate various material constants and functions in the macroscopic constitutive equation is relatively costly and time-consuming [77]. The numerical modelling is based on the known properties of the constituents and the assumption that the composite possesses a periodic structure. Thus, a RVC model is firstly constructed depending on the geometry and material phases of the composite. The properties of the composite are then obtained through an analysis of the RVC either by closed-form analytical [15-30] or finite element-based methods [31-45].

Actually, closed-form analytical methods are not readily applicable to the composites with complicated microstructures, e.g., the C/SiC composites with multi-layered interfaces or matrices due to their inherent limitation in accurately modelling the composite microstructure. In contrast, the finite element-based methods, homogenization method combined with finite element analysis and direct finite element analysis under the specified displacement boundary conditions, have the generality of being able to characterize the effective properties of complicated microstructures. However, the practical implementation of the homogenization

method is sophisticated due to the complexity of the mathematical formulation. To some extent, this complexity may influence the efficient application of the method. Comparatively, direct finite element analysis demonstrates its simplicity in numerical implementation. However, the underlying relation between the coefficient of thermal expansion (CTE) and the elastic properties cannot be revealed by this approach.

In this chapter, an alternative finite element-based method strain energy method is developed for the prediction of the effective elastic properties and CTEs of composite materials. This method is based on the relationship established between the strain energy of the microstructure and that of the homogenized equivalent model under specific thermo-elastic boundary conditions. Expressions in closed-form of the effective CTEs in terms of the strain energy and effective elastic properties are derived. Different kinds of composites are tested to validate the method. Representative RVC models with specific boundary conditions are used to evaluate effective elastic properties and CTEs that are compared with available results obtained numerically and experimentally.

## 2.2 Theory of strain energy method

In the present work, the relationship between the strain energy of RVC and homogenized equivalent model is studied for 3-D orthotropic materials. To make things clear, consider a RVC model with heterogeneous microstructure depicted in Figure 2.1a. It consists of two material phases (the dark color represent the fiber while the light color represent the matrix) and can be regarded as a homogenized equivalent model depicted in Figure 2.1b.

The macroscopic behaviors of the microstructure can be characterized by the effective stress tensor  $\bar{\sigma}$  and strain tensor  $\bar{\epsilon}$  over the homogeneous equivalent model

$$\bar{\sigma} = 1/V \int_V \sigma dV \quad (2.1)$$

$$\bar{\epsilon} = 1/V \int_V \epsilon dV \quad (2.2)$$

$V$  is the volume of the microstructure and  $\sigma$ ,  $\epsilon$  are respectively the stress tensor and strain tensor of the microstructure.

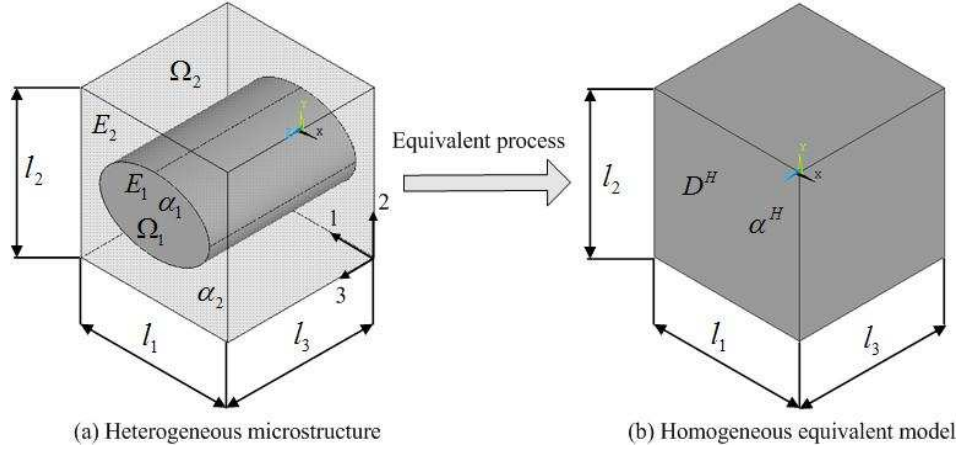


Figure 2.1 Illustration of the RVC of composite

In the elastic regime, the effective stresses  $\bar{\sigma}$  and strains  $\bar{\epsilon}$  are interrelated by the effective stiffness matrix  $D^H$

$$\bar{\sigma} = D^H \bar{\epsilon} \quad (2.3)$$

In the thermo-elastic regime, the effective stresses  $\bar{\sigma}$  and strains  $\bar{\epsilon}$ , correspond to

$$\bar{\sigma} = D^H (\bar{\epsilon} - \alpha^H \Delta T) \quad (2.4)$$

where  $\alpha^H$  denotes the effective thermal expansion coefficient matrix, and  $\Delta T$  is the variation in temperature.

Consider the case of three-dimensional orthotropic materials,  $D^H$  and  $\alpha^H$  can be written as

$$D^H = \begin{bmatrix} D_{1111}^H & D_{1122}^H & D_{1133}^H & 0 & 0 & 0 \\ D_{1122}^H & D_{2222}^H & D_{2233}^H & 0 & 0 & 0 \\ D_{1133}^H & D_{2233}^H & D_{3333}^H & 0 & 0 & 0 \\ 0 & 0 & 0 & D_{1212}^H & 0 & 0 \\ 0 & 0 & 0 & 0 & D_{2323}^H & 0 \\ 0 & 0 & 0 & 0 & 0 & D_{3131}^H \end{bmatrix} \quad (2.5)$$

$$\alpha^H = [\alpha_{11}^H \quad \alpha_{22}^H \quad \alpha_{33}^H]^T \quad (2.6)$$

### 2.2.1 Prediction of the effective elastic properties

In the elastic regime, the elastic strain energy  $W_E$  of the microstructure can be expressed as

$$\begin{aligned} W_E &= \int_V \boldsymbol{\sigma}^T \boldsymbol{\varepsilon} dV \\ &= \int_V (\sigma_{11}\varepsilon_{11} + \sigma_{22}\varepsilon_{22} + \sigma_{33}\varepsilon_{33} + \sigma_{12}\varepsilon_{12} + \sigma_{23}\varepsilon_{23} + \sigma_{31}\varepsilon_{31}) dV \end{aligned} \quad (2.7)$$

It can be demonstrated that the strain energy related to the microstructure is equal to that of the homogeneous equivalent model under uniformly distributed loading boundary conditions [41] such that

$$\begin{aligned} W_E &= \overline{\boldsymbol{\sigma}}^T \overline{\boldsymbol{\varepsilon}} V \\ &= (\overline{\sigma}_{11}\overline{\varepsilon}_{11} + \overline{\sigma}_{22}\overline{\varepsilon}_{22} + \overline{\sigma}_{33}\overline{\varepsilon}_{33} + \overline{\sigma}_{12}\overline{\varepsilon}_{12} + \overline{\sigma}_{23}\overline{\varepsilon}_{23} + \overline{\sigma}_{31}\overline{\varepsilon}_{31}) V \end{aligned} \quad (2.8)$$

With the help of specific boundary conditions, the combination of equation (2.3) and equation (2.8) can be used to deduce the effective stiffness matrix  $\mathbf{D}^H$  for the RVC. Suppose a unit initial strain is imposed in direction 1, i.e.  $\overline{\boldsymbol{\varepsilon}}^{(1)} = (1 \ 0 \ 0 \ 0 \ 0 \ 0)^T$ . The corresponding boundary condition is depicted in Table 2.1. Note that the superscript (1) represents the first load case. The corresponding average stress is then obtained by equation (2.3):

$$\overline{\boldsymbol{\sigma}}^{(1)} = (D_{1111}^H \ D_{1122}^H \ D_{1133}^H \ 0 \ 0 \ 0)^T \quad (2.9)$$

By replacing  $\overline{\boldsymbol{\sigma}}^{(1)}$  and  $\overline{\boldsymbol{\varepsilon}}^{(1)}$  into equation (2.8), one obtains the following expression of the strain energy

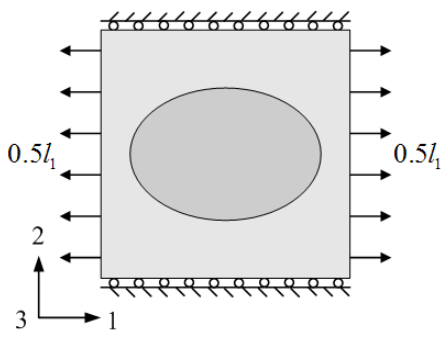
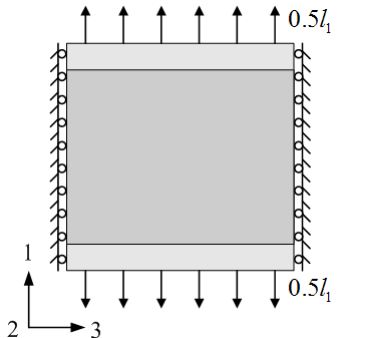
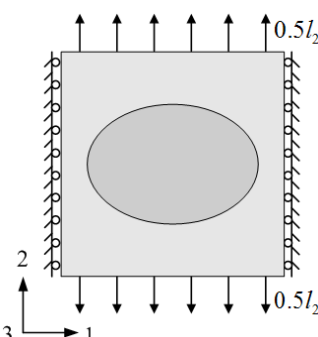
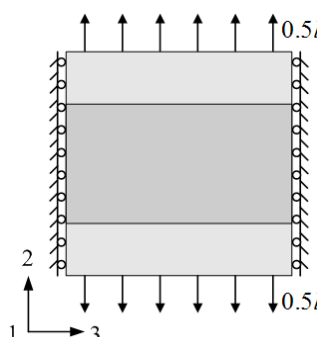
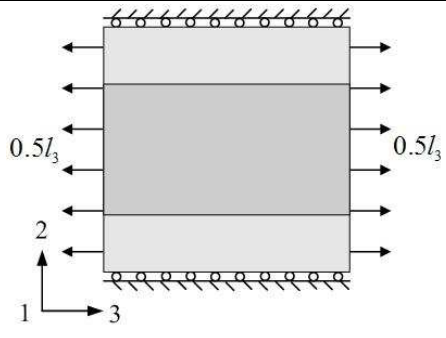
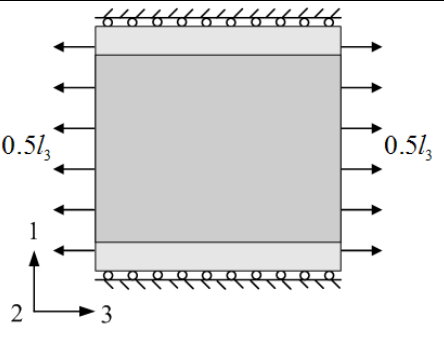
$$W_E^{(1)} = \overline{\boldsymbol{\sigma}}^{(1)T} \overline{\boldsymbol{\varepsilon}}^{(1)} V = D_{1111}^H V \quad (2.10)$$

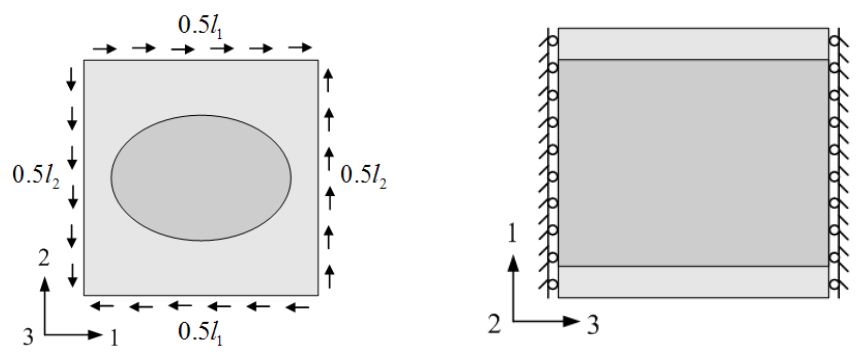
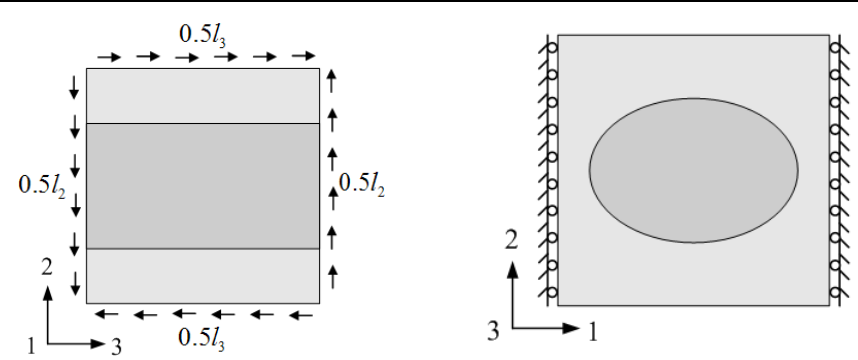
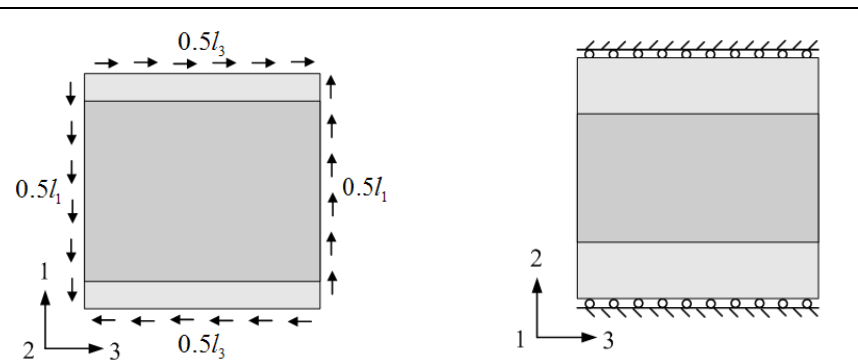
The coefficient  $D_{1111}^H$  can be derived

$$D_{1111}^H = W_E^{(1)} / V \quad (2.11)$$

In the same way, demonstrations can be made for other coefficients and all the results are summarized in Table 2.1.

Table 2.1 Boundary conditions of the RVC

Load case 1		
Boundary condition	 	<p>View of the RVC along direction 3</p> <p>View of the RVC along direction 2</p>
Coefficient	$D_{1111}^H = W_E^{(1)} / V$	
Load case 2		
Boundary condition	 	<p>View of the RVC along direction 3</p> <p>View of the RVC along direction 1</p>
Coefficient	$D_{2222}^H = W_E^{(2)} / V$	
Load case 3		
Boundary condition	 	<p>View of the RVC along direction 1</p> <p>View of the RVC along direction 2</p>
Coefficient	$D_{3333}^H = W_E^{(3)} / V$	

Load case 4		
Boundary condition	 <p>View of the RVC along direction 3</p> <p>View of the RVC along direction 2</p>	
Coefficient	$D_{1212}^H = W_E^{(4)} / V$	
Load case 5		
Boundary condition	 <p>View of the RVC along direction 1</p> <p>View of the RVC along direction 3</p>	
Coefficient	$D_{2323}^H = W_E^{(5)} / V$	
Load case 6		
Boundary condition	 <p>View of the RVC along direction 2</p> <p>View of the RVC along direction 1</p>	
Coefficient	$D_{3131}^H = W_E^{(6)} / V$	



Load case 7		
Boundary condition		
	View of the RVC along direction 3	View of the RVC along direction 2
Coefficient	$D_{1122}^H = W_E^{(7)} / 2V - D_{1111}^H / 2 - D_{2222}^H / 2$	
Load case 8		
Boundary condition		
	View of the RVC along direction 1	View of the RVC along direction 3
Coefficient	$D_{2233}^H = W_E^{(8)} / V - D_{2222}^H / 2 - D_{3333}^H / 2$	
Load case 9		
Boundary condition		
	View of the RVC along direction 2	View of the RVC along direction 1
Coefficient	$D_{1133}^H = W_E^{(9)} / 2V - D_{1111}^H / 2 - D_{3333}^H / 2$	

In conclusion, the effective stiffness matrix can be written as

$$\begin{bmatrix}
\frac{W_E^{(1)}}{V} & \frac{W_E^{(7)} - W_E^{(2)} - W_E^{(1)}}{2V} & \frac{W_E^{(9)} - W_E^{(3)} - W_E^{(1)}}{2V} & 0 & 0 & 0 \\
& \frac{W_E^{(2)}}{V} & \frac{W_E^{(8)} - W_E^{(3)} - W_E^{(2)}}{2V} & 0 & 0 & 0 \\
& & \frac{W_E^{(3)}}{V} & 0 & 0 & 0 \\
& & & \frac{W_E^{(4)}}{V} & 0 & 0 \\
& & & & \frac{W_E^{(5)}}{V} & 0 \\
sym & & & & & \frac{W_E^{(6)}}{V}
\end{bmatrix} \quad (2.12)$$

The elastic modulus can be derived by inverting the above matrix. In practice, the considered RVC will be discretized as a finite element model, on which the initial strain and periodic conditions will be imposed to evaluate the strain energy. Here, the finite element discretizations and analyses are all implemented by *ANSYS* finite element software.

### 2.2.2 Prediction of the effective CTEs

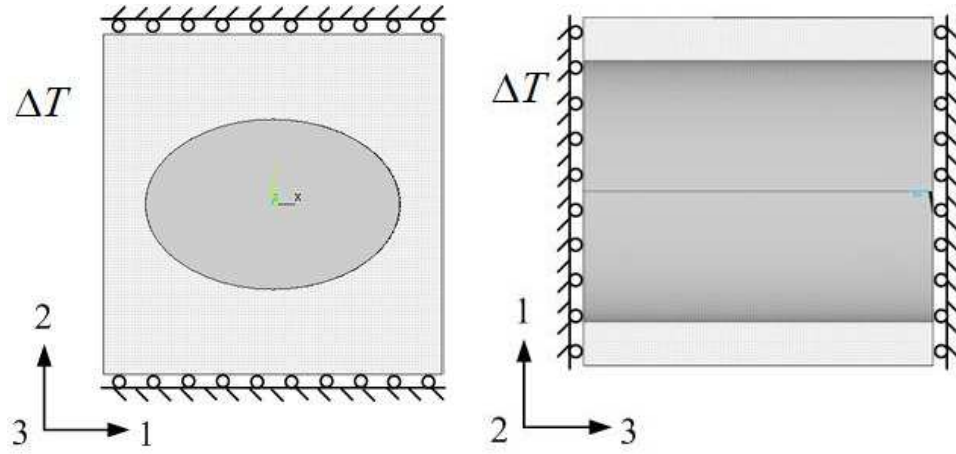
According to equation (2.4), the relationship between effective stress and strain in the thermal regime can be expressed as

$$\begin{aligned}
\bar{\sigma}_{11} &= D_{1111}^H (\bar{\epsilon}_{11} - \alpha_{11}^H \Delta T) + D_{1122}^H (\bar{\epsilon}_{22} - \alpha_{22}^H \Delta T) + D_{1133}^H (\bar{\epsilon}_{33} - \alpha_{33}^H \Delta T) \\
\bar{\sigma}_{22} &= D_{1122}^H (\bar{\epsilon}_{11} - \alpha_{11}^H \Delta T) + D_{2222}^H (\bar{\epsilon}_{22} - \alpha_{22}^H \Delta T) + D_{2233}^H (\bar{\epsilon}_{33} - \alpha_{33}^H \Delta T) \\
\bar{\sigma}_{33} &= D_{1133}^H (\bar{\epsilon}_{11} - \alpha_{11}^H \Delta T) + D_{2233}^H (\bar{\epsilon}_{22} - \alpha_{22}^H \Delta T) + D_{3333}^H (\bar{\epsilon}_{33} - \alpha_{33}^H \Delta T)
\end{aligned} \quad (2.13)$$

The strain energy related to the microstructure corresponds to

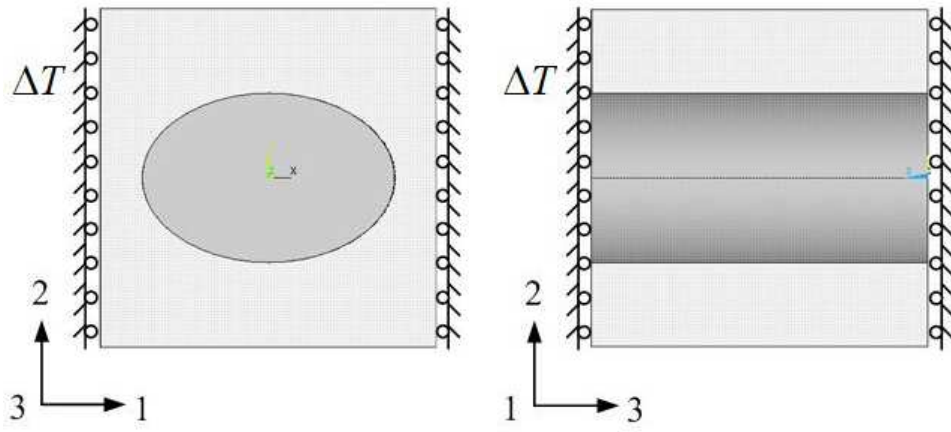
$$W_T = \int_{\Omega} \boldsymbol{\sigma}^T \boldsymbol{\epsilon} d\Omega \quad (2.14)$$

Now, consider the following three kinds of boundary conditions depicted in Figures 2.2-2.4, respectively.



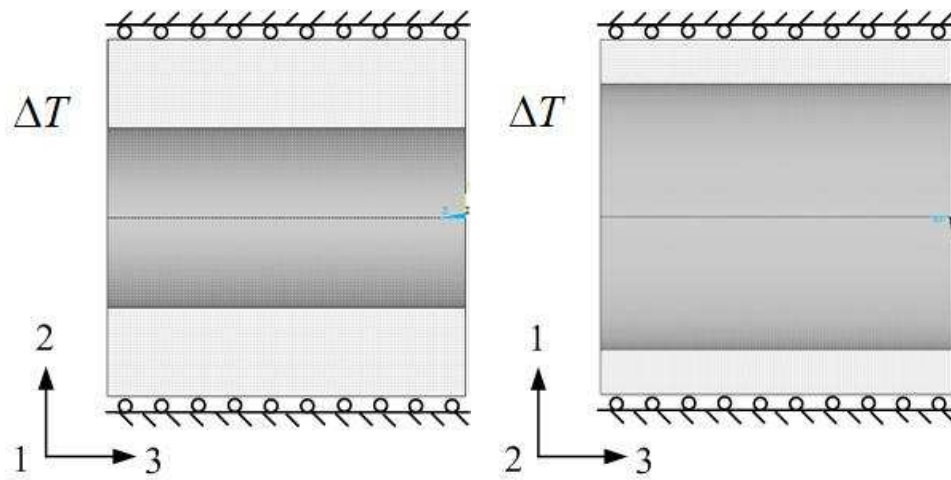
(a) View of the RVC along direction 3 (b) View of the RVC along direction 2

Figure 2.2 RVC under boundary condition 1



(a) View of the RVC along direction 3 (b) View of the RVC along direction 1

Figure 2.3 RVC under boundary condition 2



(a) View of the RVC along direction 1 (b) View of the RVC along direction 2

Figure 2.4 RVC under boundary condition 3

Boundary condition 1 corresponds to

$$\bar{\sigma}_{11}^{(1)} = 0, \quad \bar{\varepsilon}_{22}^{(1)} = 0, \quad \bar{\varepsilon}_{33}^{(1)} = 0 \quad (2.15)$$

Note that the superscript (1) represents the number of boundary condition. The RVC is restricted to move in directions 2 and 3. It is only free to move along direction 1 but planes  $x_1 = 0$  and  $x_1 = l_1$  have to remain planar and parallel to preserve the compatibility with adjacent cells. Finally, the substitution of equation (2.15) into equation (2.13) gives rise to the following expressions

$$\begin{aligned} \bar{\varepsilon}_{11}^{(1)} &= \alpha_{11}^H \Delta T + \frac{D_{1122}^H}{D_{1111}^H} \alpha_{22}^H \Delta T + \frac{D_{1133}^H}{D_{1111}^H} \alpha_{33}^H \Delta T \\ \bar{\sigma}_{22}^{(1)} &= \left( \frac{D_{1122}^H D_{1122}^H}{D_{1111}^H} - D_{2222}^H \right) \alpha_{22}^H \Delta T + \left( \frac{D_{1122}^H D_{1133}^H}{D_{1111}^H} - D_{2233}^H \right) \alpha_{33}^H \Delta T \\ \bar{\sigma}_{33}^{(1)} &= \left( \frac{D_{1133}^H D_{1122}^H}{D_{1111}^H} - D_{2233}^H \right) \alpha_{22}^H \Delta T + \left( \frac{D_{1133}^H D_{1133}^H}{D_{1111}^H} - D_{3333}^H \right) \alpha_{33}^H \Delta T \end{aligned} \quad (2.16)$$

For the other two boundary conditions depicted in Figures 2.3-2.4, the same demonstrations can be made to find following expressions

$$\begin{aligned} \bar{\varepsilon}_{22}^{(1)} &= \alpha_{22}^H \Delta T + \frac{D_{1122}^H}{D_{2222}^H} \alpha_{11}^H \Delta T + \frac{D_{2233}^H}{D_{2222}^H} \alpha_{33}^H \Delta T \\ \bar{\sigma}_{11}^{(1)} &= \left( \frac{D_{1122}^H D_{1122}^H}{D_{2222}^H} - D_{1111}^H \right) \alpha_{11}^H \Delta T + \left( \frac{D_{1122}^H D_{2233}^H}{D_{2222}^H} - D_{1133}^H \right) \alpha_{33}^H \Delta T \\ \bar{\sigma}_{33}^{(1)} &= \left( \frac{D_{2233}^H D_{1122}^H}{D_{2222}^H} - D_{1133}^H \right) \alpha_{11}^H \Delta T + \left( \frac{D_{2233}^H D_{2233}^H}{D_{2222}^H} - D_{3333}^H \right) \alpha_{33}^H \Delta T \end{aligned} \quad (2.17)$$

$$\begin{aligned} \bar{\varepsilon}_{33}^{(1)} &= \alpha_{33}^H \Delta T + \frac{D_{1133}^H}{D_{3333}^H} \alpha_{11}^H \Delta T + \frac{D_{2233}^H}{D_{3333}^H} \alpha_{22}^H \Delta T \\ \bar{\sigma}_{11}^{(1)} &= \left( \frac{D_{1133}^H D_{1133}^H}{D_{3333}^H} - D_{1111}^H \right) \alpha_{11}^H \Delta T + \left( \frac{D_{1133}^H D_{2233}^H}{D_{3333}^H} - D_{1122}^H \right) \alpha_{22}^H \Delta T \\ \bar{\sigma}_{22}^{(1)} &= \left( \frac{D_{2233}^H D_{1133}^H}{D_{3333}^H} - D_{1122}^H \right) \alpha_{11}^H \Delta T + \left( \frac{D_{2233}^H D_{2233}^H}{D_{3333}^H} - D_{2222}^H \right) \alpha_{22}^H \Delta T \end{aligned} \quad (2.18)$$

By analogy, consider now the models with mechanical boundary conditions. Figure 2.5 shows boundary condition 4 for which the displacement  $u_1$  and fiber/matrix interface force  $f$  are imposed. This model is equivalent to that under boundary condition 1 provided that

$$u_1 = \left( \alpha_{11}^H \Delta T + \frac{D_{1122}^H}{D_{1111}^H} \alpha_{22}^H \Delta T + \frac{D_{1133}^H}{D_{1111}^H} \alpha_{33}^H \Delta T \right) l_1 \quad (2.19)$$

$$f = \int_S \left[ \mathbf{D}(E_1) \boldsymbol{\alpha}(\alpha_1) \Delta T - \mathbf{D}(E_2) \boldsymbol{\alpha}(\alpha_2) \Delta T \right] ds \quad (2.20)$$

where  $S$  denotes the interfacial area between two material phases.

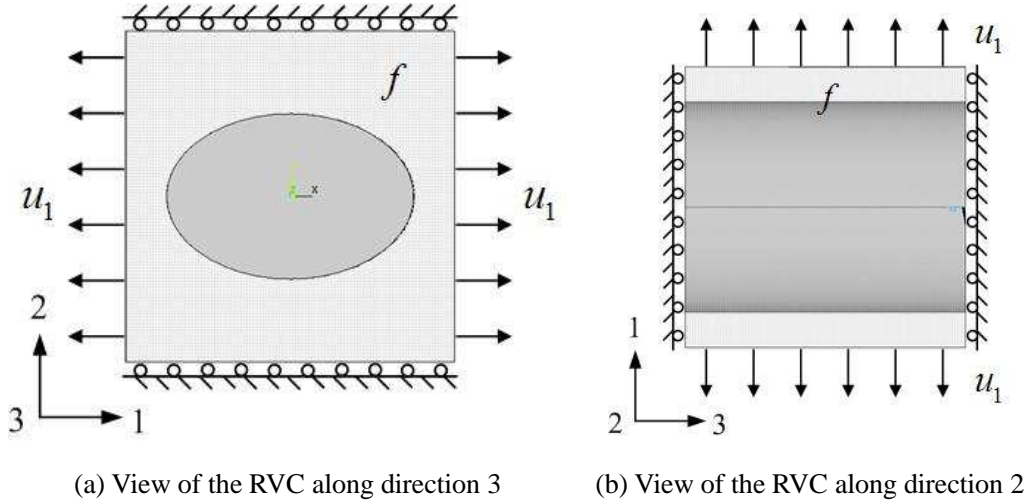


Figure 2.5 RVC under boundary condition 4

This relation implies that the strain energies of RVC under both two boundary conditions are equivalent

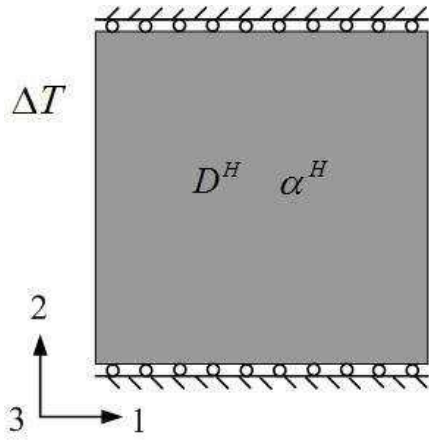
$$W_{TR}^{(1)} = W_{TR}^{(4)} \quad (21)$$

where  $W_{TR}^{(1)}$  and  $W_{TR}^{(4)}$  indicate the strain energy of RVC under boundary condition 1 and 4, respectively.

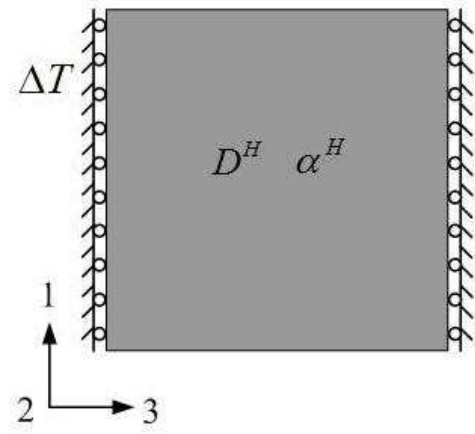
Similar demonstration can be made. The equivalent model under boundary condition 1 (depicted in Figure 2.6) has the same deformation field as that under boundary condition 5 (depicted in Figure 2.7), and the strain energies of equivalent model under these two boundary conditions are equivalent

$$W_{TH}^{(1)} = W_{TH}^{(5)} \quad (2.22)$$

where  $W_{TH}^{(1)}$  and  $W_{TH}^{(5)}$  refer to the strain energy of homogeneous equivalent model under boundary condition 1 and 5, respectively.

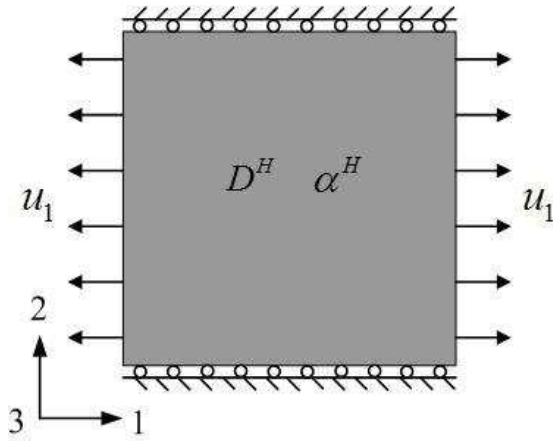


(a) View of the homogenized equivalent model along direction 3

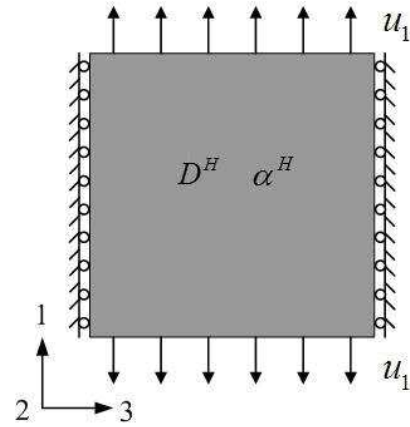


(b) View of the homogenized equivalent model along direction 2

Figure 2.6 Homogenized equivalent model under boundary condition 1



(a) View of the homogenized equivalent model along direction 3



(b) View of the homogenized equivalent model along direction 2

Figure 2.7 Homogenized equivalent model under boundary condition 5

The strain energy of RVC under boundary condition 5 (depicted in Figure 2.8),  $W_{TR}^{(5)}$ , can be expressed as

$$W_{TR}^{(5)} = W_{TH}^{(5)} \quad (2.23)$$

The comparison between equation (2.23) and (2.22) results in

$$W_{TR}^{(5)} = W_{TH}^{(1)} \quad (2.24)$$

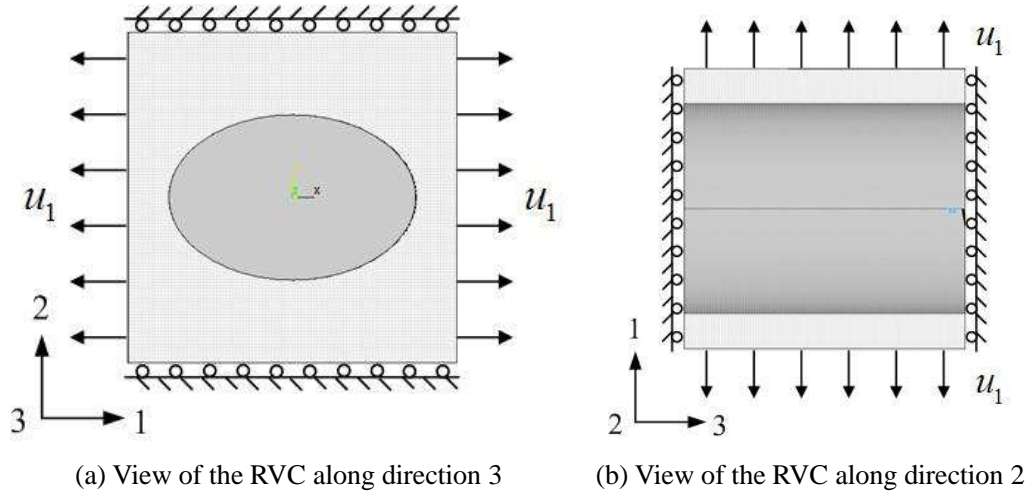


Figure 2.8 RVC under boundary condition 5

Boundary conditions 6 and 7, as illustrated in Figures 2.9-2.10, are then imposed on the RVC respectively. The interface force  $f$  denoted in Figure 2.10 is equivalent to that caused by the thermal deformation under boundary condition 6. Hence, the strain energies of RVC under both two boundary conditions are equivalent

$$W_{TR}^{(6)} = W_{TR}^{(7)} \quad (2.25)$$

where  $W_{TR}^{(6)}$  and  $W_{TR}^{(7)}$  refer to the strain energy of RVC under boundary condition 6 and 7, respectively.

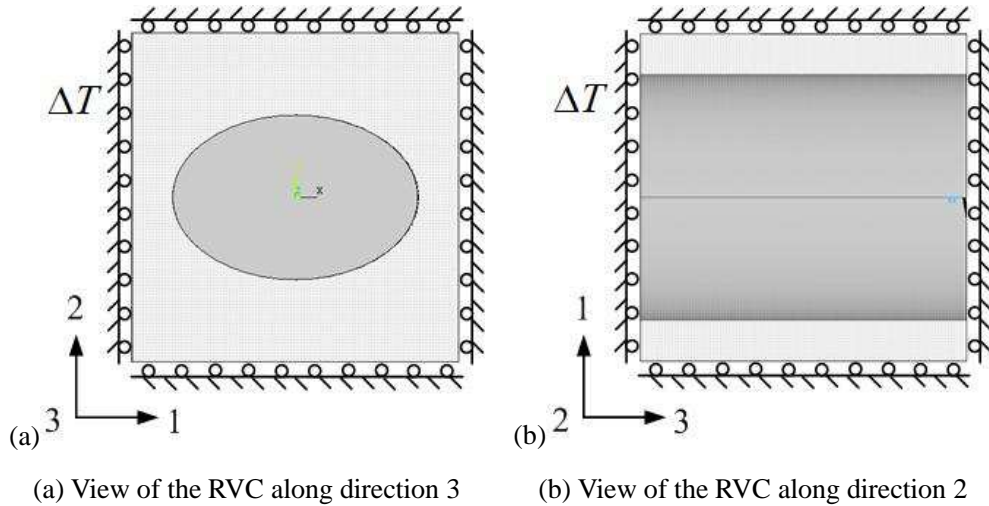


Figure 2.9 RVC under boundary condition 6

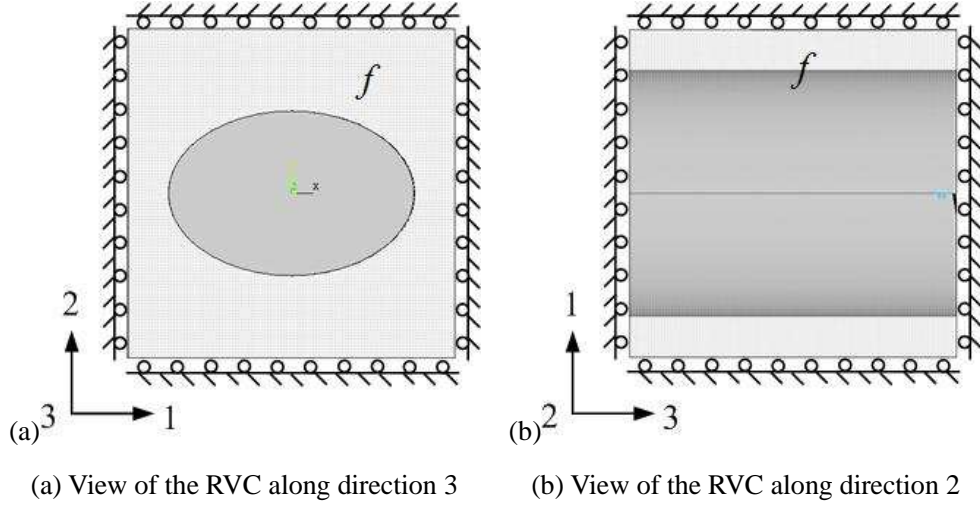


Figure 2.10 RVC under boundary condition 7

Considering the RVC under boundary conditions 4, 5 and 7, one can explicitly derive the following expression

$$W_{TR}^{(5)} + W_{TR}^{(7)} = W_{TR}^{(4)} \quad (2.26)$$

Then, the relation between the strain energy of RVC and homogeneous equivalent model under boundary condition 1 can be obtained by substituting equations (2.21), (2.24) and (2.25) into equation (2.26)

$$W_{TR}^{(1)} = W_{TR}^{(6)} + W_{TH}^{(1)} \quad (2.27)$$

The same demonstrations can be made to obtain the relationship between the strain energy of RVC and homogeneous equivalent model under boundary condition 2

$$W_{TR}^{(2)} = W_{TR}^{(6)} + W_{TH}^{(2)} \quad (2.28)$$

and boundary condition 3

$$W_{TR}^{(3)} = W_{TR}^{(6)} + W_{TH}^{(3)} \quad (2.29)$$

The strain energy of homogeneous equivalent model under boundary conditions 1, 2 and 3 can be easily determined as:

$$W_{TH}^{(1)} = D_{1111}^H \left( \alpha_{11}^H \Delta T + \frac{D_{1122}^H}{D_{1111}^H} \alpha_{22}^H \Delta T + \frac{D_{1133}^H}{D_{1111}^H} \alpha_{33}^H \Delta T \right)^2 V \quad (2.30)$$

$$W_{TH}^{(2)} = D_{2222}^H \left( \alpha_{22}^H \Delta T + \frac{D_{1122}^H}{D_{2222}^H} \alpha_{11}^H \Delta T + \frac{D_{2233}^H}{D_{2222}^H} \alpha_{33}^H \Delta T \right)^2 V \quad (2.31)$$



$$W_{TH}^{(3)} = D_{3333}^H \left( \alpha_{33}^H \Delta T + \frac{D_{1133}^H}{D_{3333}^H} \alpha_{11}^H \Delta T + \frac{D_{2233}^H}{D_{3333}^H} \alpha_{22}^H \Delta T \right)^2 V \quad (2.32)$$

note that  $V$  is the volume of RVC. By replacing  $W_{TH}^{(1)}$ ,  $W_{TH}^{(2)}$  and  $W_{TH}^{(3)}$  into equations (2.27), (2.28) and (2.20), respectively, one obtains the following expressions

$$W_{TR}^{(1)} - W_{TR}^{(6)} = D_{1111}^H \left( \alpha_{11}^H \Delta T + \frac{D_{1122}^H}{D_{1111}^H} \alpha_{22}^H \Delta T + \frac{D_{1133}^H}{D_{1111}^H} \alpha_{33}^H \Delta T \right)^2 V \quad (2.33)$$

$$W_{TR}^{(2)} - W_{TR}^{(6)} = D_{2222}^H \left( \alpha_{22}^H \Delta T + \frac{D_{1122}^H}{D_{2222}^H} \alpha_{11}^H \Delta T + \frac{D_{2233}^H}{D_{2222}^H} \alpha_{33}^H \Delta T \right)^2 V \quad (2.34)$$

$$W_{TR}^{(3)} - W_{TR}^{(6)} = D_{3333}^H \left( \alpha_{33}^H \Delta T + \frac{D_{1133}^H}{D_{3333}^H} \alpha_{11}^H \Delta T + \frac{D_{2233}^H}{D_{3333}^H} \alpha_{22}^H \Delta T \right)^2 V \quad (2.35)$$

Solving equations (2.33)-(2.35) finally yield the effective CTEs of RVC:

$$\alpha_{11}^H = \frac{\left( \frac{D_{1122}^H}{D_{1111}^H} \frac{D_{2233}^H}{D_{2222}^H} - \frac{D_{1133}^H}{D_{1111}^H} \right) \left( \frac{D_{2233}^H}{D_{3333}^H} Q - R \right) - \left( \frac{D_{2233}^H}{D_{3333}^H} \frac{D_{2233}^H}{D_{2222}^H} - 1 \right) \left( \frac{D_{1122}^H}{D_{1111}^H} Q - P \right)}{\left( \frac{D_{1122}^H}{D_{1111}^H} \frac{D_{2233}^H}{D_{2222}^H} - \frac{D_{1133}^H}{D_{1111}^H} \right) \left( \frac{D_{2233}^H}{D_{3333}^H} \frac{D_{1122}^H}{D_{2222}^H} - \frac{D_{1133}^H}{D_{3333}^H} \right) - \left( \frac{D_{2233}^H}{D_{3333}^H} \frac{D_{2233}^H}{D_{2222}^H} - 1 \right) \left( \frac{D_{1122}^H}{D_{1111}^H} \frac{D_{1122}^H}{D_{2222}^H} - 1 \right)} \quad (2.36)$$

$$\alpha_{22}^H = \frac{\left( \frac{D_{1122}^H}{D_{2222}^H} \frac{D_{1133}^H}{D_{1111}^H} - \frac{D_{2233}^H}{D_{2222}^H} \right) \left( \frac{D_{1133}^H}{D_{3333}^H} P - R \right) - \left( \frac{D_{1133}^H}{D_{3333}^H} \frac{D_{1133}^H}{D_{1111}^H} - 1 \right) \left( \frac{D_{1122}^H}{D_{2222}^H} P - Q \right)}{\left( \frac{D_{1122}^H}{D_{2222}^H} \frac{D_{1133}^H}{D_{1111}^H} - \frac{D_{2233}^H}{D_{2222}^H} \right) \left( \frac{D_{1133}^H}{D_{3333}^H} \frac{D_{1122}^H}{D_{1111}^H} - \frac{D_{2233}^H}{D_{3333}^H} \right) - \left( \frac{D_{1133}^H}{D_{3333}^H} \frac{D_{1133}^H}{D_{1111}^H} - 1 \right) \left( \frac{D_{1122}^H}{D_{2222}^H} \frac{D_{1122}^H}{D_{1111}^H} - 1 \right)} \quad (2.37)$$

$$\alpha_{33}^H = \frac{\left( \frac{D_{1133}^H}{D_{3333}^H} \frac{D_{1122}^H}{D_{1111}^H} - \frac{D_{2233}^H}{D_{3333}^H} \right) \left( \frac{D_{1122}^H}{D_{2222}^H} P - Q \right) - \left( \frac{D_{1122}^H}{D_{2222}^H} \frac{D_{1122}^H}{D_{1111}^H} - 1 \right) \left( \frac{D_{1133}^H}{D_{3333}^H} P - R \right)}{\left( \frac{D_{1133}^H}{D_{3333}^H} \frac{D_{1122}^H}{D_{1111}^H} - \frac{D_{2233}^H}{D_{3333}^H} \right) \left( \frac{D_{1122}^H}{D_{2222}^H} \frac{D_{1133}^H}{D_{1111}^H} - \frac{D_{2233}^H}{D_{2222}^H} \right) - \left( \frac{D_{1122}^H}{D_{2222}^H} \frac{D_{1122}^H}{D_{1111}^H} - 1 \right) \left( \frac{D_{1133}^H}{D_{3333}^H} \frac{D_{1133}^H}{D_{1111}^H} - 1 \right)} \quad (2.38)$$

where  $P = \sqrt{\frac{W_{TR}^{(1)} - W_{TR}^{(6)}}{D_{1111}^H (\Delta T)^2 V}}$ ,  $Q = \sqrt{\frac{W_{TR}^{(2)} - W_{TR}^{(6)}}{D_{2222}^H (\Delta T)^2 V}}$  and  $R = \sqrt{\frac{W_{TR}^{(3)} - W_{TR}^{(6)}}{D_{3333}^H (\Delta T)^2 V}}$ . Regarding the

above equations, an important point to be noted is that the explicit closed-form expressions can be established between the effective CTEs and the elastic tensors by virtue of the strain energy method. In contrast, the other finite element-based methods, i.e. the homogenization method and finite element analysis, are both incapable of reflecting this relation explicitly.

In practice, the considered RVC will be discretized into a finite element model on which the above four boundary conditions 1, 2, 3 and 6 will be imposed to evaluate the corresponding

strain energies.

## 2.3 Numerical examples

In this section, several applications of strain energy method are presented. Two representative fiber-reinforced composite models including unidirectional and woven composite and a spherical porous composite model are studied. The effective elastic properties and CTEs are computed by means of strain energy method and compared with the results reported in the literature.

### 2.3.1 Prediction of elastic modulus of unidirectional composite

A unidirectional composite is firstly studied to validate the proposed approach with the help of the data in literature. Figure 2.11 shows the finite element model of the RVC with a 60% fiber volume fraction. Similar finite element models are created for other volume fractions. The matrix and the fiber are considered as isotropic materials, and its elastic properties are:  $E_f = 413.7GPa$ ,  $\nu_f = 0.2$  and  $E_m = 4.137GPa$ ,  $\nu_m = 0.35$ , respectively [78].

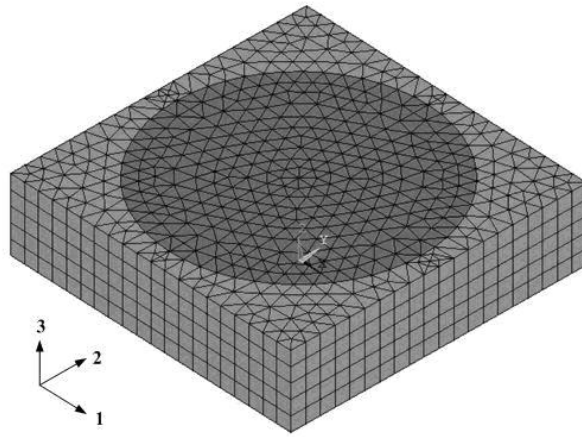


Figure 2.11 Finite element model of the RVC for unidirectional composite

Table 2.2 lists the numerically obtained longitudinal modulus against the experimental data and numerical values evaluated by homogenization method in [78]. It can be seen that the predicted results match well with the experiments and numerical results.

Table 2.2 Comparison of computed longitudinal modulus with experimental and numerical results

$V_f$	Strain energy method	Homogenization method [70]	Experiment [70]
	$E_{33}$ (GPa)	$E_{33}$ (GPa)	$E_{33}$ (GPa)
0.20	86.05	84.39	80.67
0.50	229.41	227.45	207.54
0.60	249.88	247.8	246.15
0.65	270.39	268.51	244.77

Note:  $V_f$  is the volume fraction of fiber.

### 2.3.2 Prediction of CTEs of unidirectional composite

The effective CTEs of an E-glass/epoxy unidirectional composite are predicted in this section. The finite element model of the RVC is shown in Figure 2.11. The properties of the constituents are taken from the literature [79] and are given in Table 2.3.

Table 2.3 Properties of the constituents

	E (GPa)	G (GPa)	$\nu$	$\alpha \cdot 10^{-6}/^{\circ}\text{C}$
E-glass fiber	72	40	0.2	5
Epoxy matrix	3.5	1.3	0.35	52.5

The present numerical results are compared with the experimental data and numerical results obtained by the analytical method “Chamis equation” (Note that the details about “Chamis equation” were discussed in the literature [79]). The longitudinal and transverse CTEs are shown in Figure 2.12 and Figure 2.13, respectively. It can be observed that the differences between the longitudinal CTEs predicted by the strain energy model and “Chamis equation” are negligible. All of the models are in good agreement with the experimental data for longitudinal CTE. For the transverse CTE, the results of strain energy model are in much better agreement with the experimental data than “Chamis equation”.

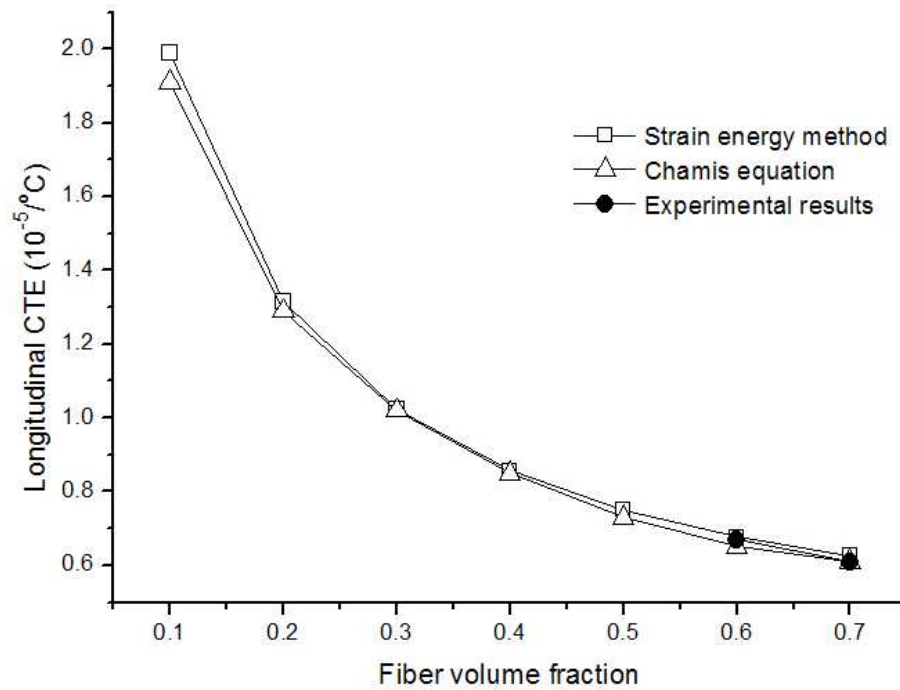


Figure 2.12 Longitudinal CTE of E-glass/epoxy unidirectional composite

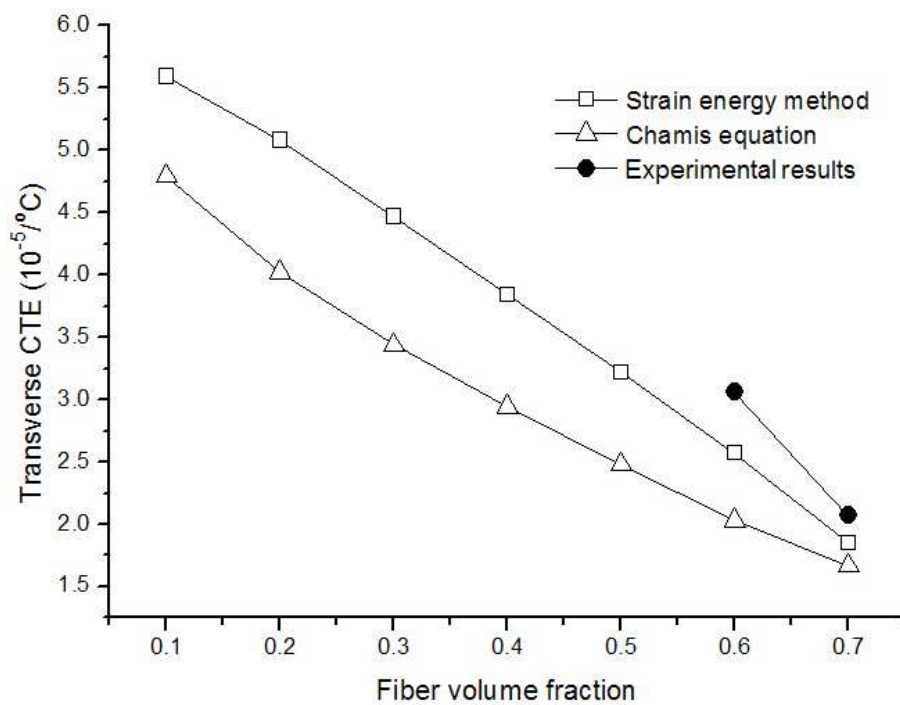


Figure 2.13 Transverse CTE of E-glass/epoxy unidirectional composite

### 2.3.3 Prediction of CTEs of spherical porous material

In this section, the effective CTE of the spherical porous alumina are predicted. The finite

element model of the unit cell with a 50% porosity is shown in Figure 2.14. The properties of alumina are listed here

$$E = 413.7 \text{ GPa}, \quad \nu = 0.2, \quad \alpha = 23.6 \times 10^{-6} / K$$

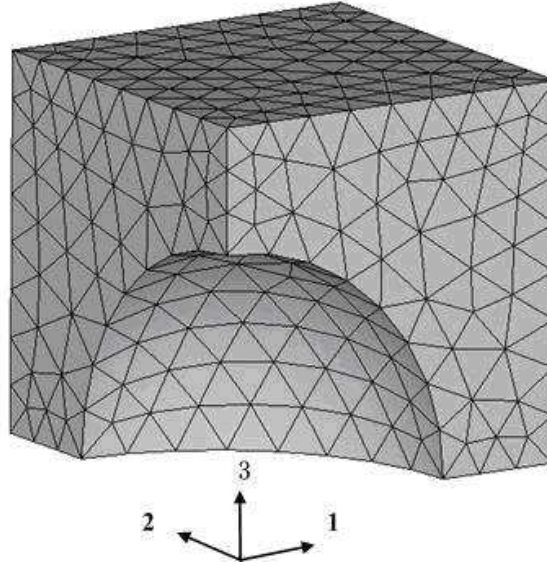


Figure 2.14 1/8 finite element model of the RVC for spherical porous alumina

The effective CTE computed by the strain energy method is given in Table 2.4. As only one solid phase is involved, it can be seen that the CTE is always equal to that of alumina and not influenced by the porosity, which is consistent with the physics.

Table 2.4 Computed CTE of the spherical porous alumina with different porous ratio

$f_p$	0.1	0.2	0.3	0.4	0.5	0.6	0.7	0.8
$\alpha_H$	23.6051	23.6143	23.6086	23.6099	23.6107	23.6122	23.6019	23.6085

Note:  $f_p$  is the porosity ratio, and  $\alpha_H$  denotes the effective CTE.

### 2.3.4 Prediction of elastic modulus and CTEs of woven composite

2-D plain weave is the most commonly used reinforcement form in woven fabric composites. An E-glass/epoxy plain weave laminates composite studied by Dasgupta et al. [42] is taken into account. The laminates consist of 35% E-glass fiber with the fiber volume fraction within

the tow of 65%. Given these two volume fractions, the tow volume fraction ( $V_{tow}$ ) within the unit cell is 53.85%, which is calculated by the ratio of the overall fiber volume fraction (35%) to the fiber volume fraction in the tow (65%). Material properties of the E-glass/epoxy tow and epoxy matrix are given in Table 2.5.

Table 2.5 Properties of E-glass/epoxy tow and epoxy matrix

	$E_{11}$ (GPa)	$E_{33}$ (GPa)	$G_{12}$ (GPa)	$G_{23}$ (GPa)	$\nu_{12}$	$\nu_{23}$	$\alpha_{11}$ ( $10^{-6}/^{\circ}C$ )	$\alpha_{33}$ ( $10^{-6}/^{\circ}C$ )
E-glass/epoxy tow	17.16	46.16	3.539	4.941	0.27	0.099	32.5	7.83
Epoxy matrix	3.45	3.45	1.259	1.259	0.37	0.37	69.0	69.0

The finite element model of the RVC for plain weave laminate composite is shown in Figure 2.15.

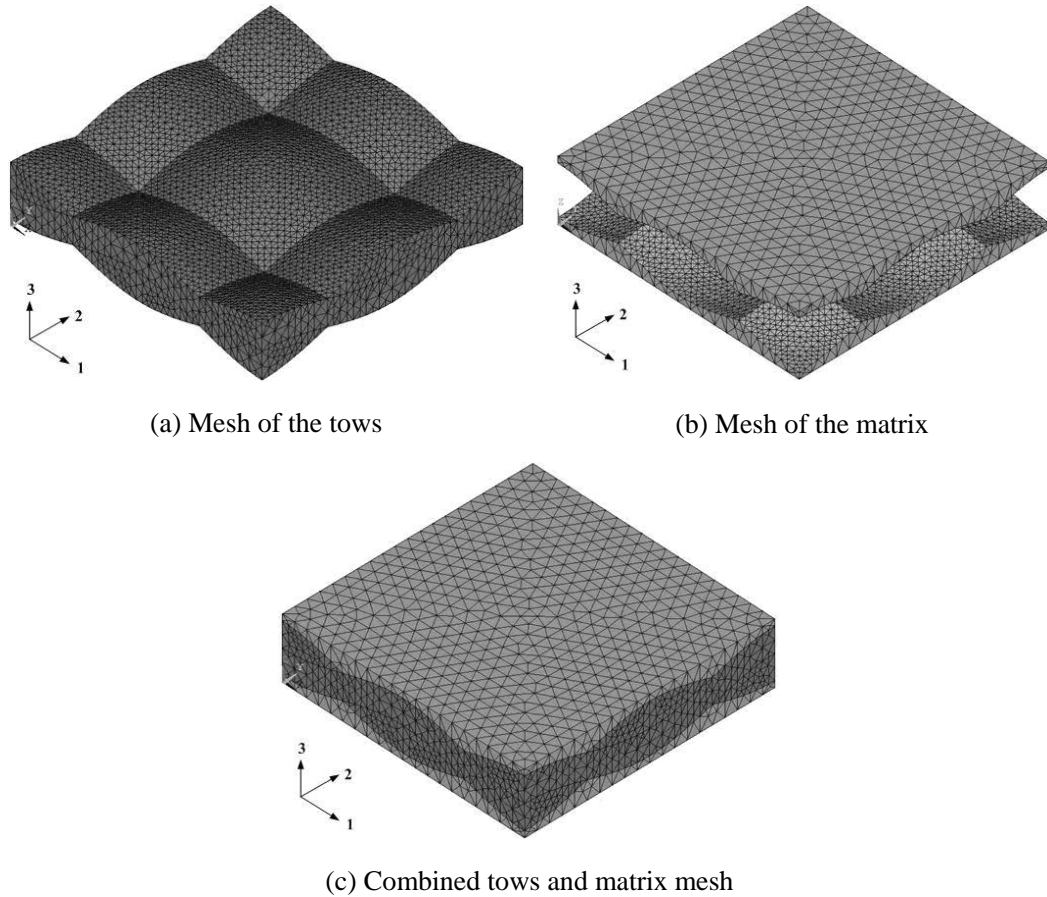


Figure 2.15 Finite element model of the RVC for plain weave laminate composite

Table 2.6 lists the numerically obtained elastic modulus and CTEs against experimental

results and numerical values evaluated by homogenization method in the literature [42]. It can be seen that the computed results are globally in agreement with both the experimental results and numerical ones. However, because the present RVC model does not precisely coincide with the microstructure geometry modeled in the literature [42], the results computed by the present method are a little higher than homogenization results.

Table 2.6 Comparison of computed results with experimental and numerical results

	Strain energy method	Homogenization method [42]	Experiment [42]
$E_{11}, E_{22}$ (GPa)	21.16	19.7	18.8
$\alpha_{11}, \alpha_{22}$ ( $10^{-6}/^{\circ}\text{C}$ )	18.37	17.6	15.0
$\alpha_{33}$ ( $10^{-6}/^{\circ}\text{C}$ )	56.34	54.2	58.1

## 2.4 Conclusions

In this chapter, an alternative finite element-based method using strain energy model is proposed for the numerical prediction of the effective elastic properties and CTEs of 3-D orthotropic composite materials. The significance of this method lies in its simplicity in numerical implementation compared with the homogenization method. In addition, by applying the strain energy model, the closed-form expressions between the effective CTEs and the elastic tensors can be established explicitly, which cannot be achieved by the homogenization method and finite element analysis. To assess the accuracy of strain energy method, two representative fiber-reinforced composite models including unidirectional, woven and a spherical porous composite model are studied. All of the results are in good agreement with the available experimental data and results of other numerical methods.

## **Chapter 3: Microstructure modelling and prediction of effective properties of woven and braided C/SiC composites**

### **3.1 Introduction**

Exact prediction of the effective properties plays an important role in the application and design of C/SiC composites. The key issue involved in the predicting studies is the exact modelling of the microstructure of RVC for C/SiC composites. As is known, C/SiC composites especially the composites with multi-layer interfaces or matrices have very complex microstructures due to the multi-layer architecture in its geometrical configuration and the large heterogeneity of multi-phase materials. For this reason, the effective properties of C/SiC composites depend upon many parameters such as the geometrical variations including fabric architecture (woven or braided fabric) and thicknesses of interfaces and matrix layers.

In this chapter, the C/SiC composites with multi-layer interfaces and matrices are considered. The interface and matrix are both composed of multi-layer alternate PyC and SiC phases. Figure 3.1 illustrates the fabricating procedure of C/SiC composites in a bottom-up sequence. Firstly, square or hexagonal arrangements of carbon fibers whose diameters are several microns constitute the tow. Secondly, the tows are interlaced to form the woven or braided preform according to different braiding techniques. Finally, the composite structure is obtained by means of the following isothermal chemical vapor infiltration (CVI) processes [80-81]:

- Alternate infiltration of PyC and SiC into the preform to generate the interfaces. The multi-layer interfaces consisting of PyC and SiC are formed around the fiber, as shown in Figure 3.1a.
- Alternate infiltration of PyC and SiC into the preform to generate the matrix. The multi-layer matrices consisting of PyC and SiC are firstly formed around the



interfaces and then formed around the tow after the spaces within the tow are filled up by the matrix, which is illustrated in Figure 3.1b.

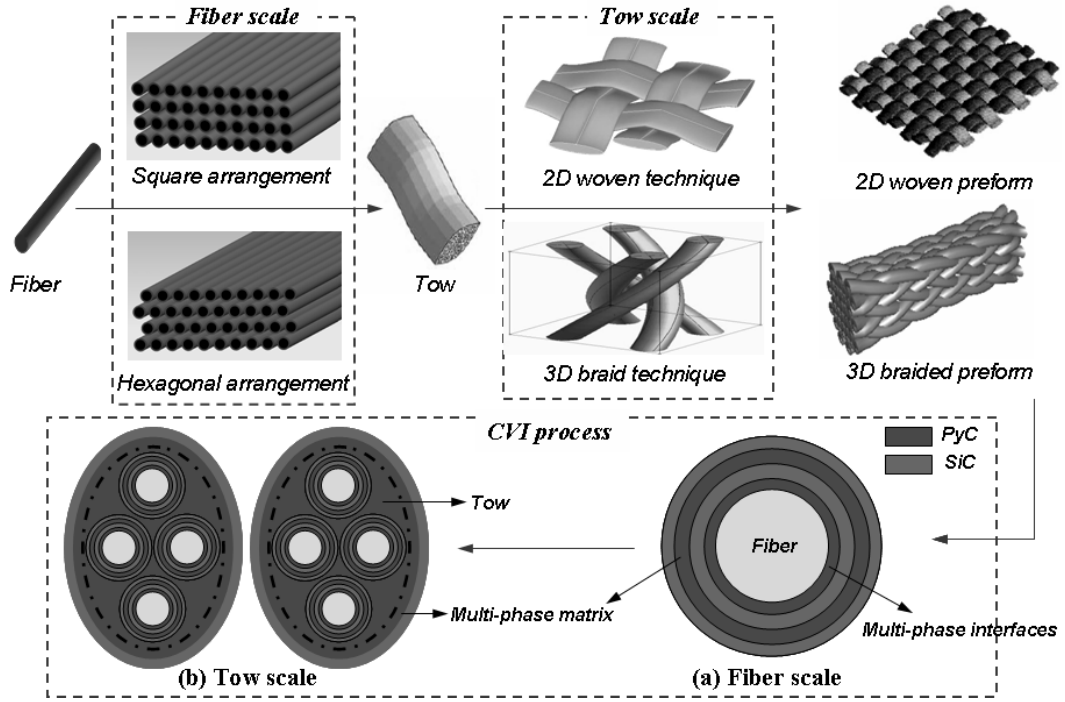


Figure 3.1 Illustration of the fabrication procedure of C/SiC composites

Regarding the forming process and the materials distribution, the RVC model of the C/SiC composites must involve two scales: fiber scale and tow scale. The first scale concerns the modelling of RVC for tows and the second scale concerns the modelling of RVC for woven or braided composites. Consequently, two levels of numerical analysis are performed to predict the properties of C/SiC composites:

- On the fiber scale, a finite element model is built to obtain the effective properties of the fiber-scale RVC, and the results are used for the tows that are treated as a homogeneous transversely isotropic material.
- On the tow scale, based on the obtained effective properties of tows, a finite element model of the tow-scale RVC is created to evaluate effective properties of the composites.

In this chapter, the RVC microstructures of 2-D woven and 3-D braided C/SiC composites with multi-layer interfaces and matrices are firstly modeled. The geometrical configurations of the microstructures are analyzed and mathematical relationships among different

geometrical parameters are derived on each scale. The strain energy method is then applied to evaluate the effective elastic moduli and CTEs of composites sequentially from fiber scale to tow scale. Numerical results are finally compared with the experimental data.

## 3.2 Microstructure modelling of 2-D woven C/SiC composites

### 3.2.1 Fiber scale

Here, the fiber scale concerns the tows which are considered as unidirectional fiber reinforced composites with multi-layer interfaces and matrices. As seen in Figure 3.2a, a hexagonal arrangement of fibers is assumed in this study. Figure 3.2b shows a RVC model with two layers of interfaces and two layers of matrices.

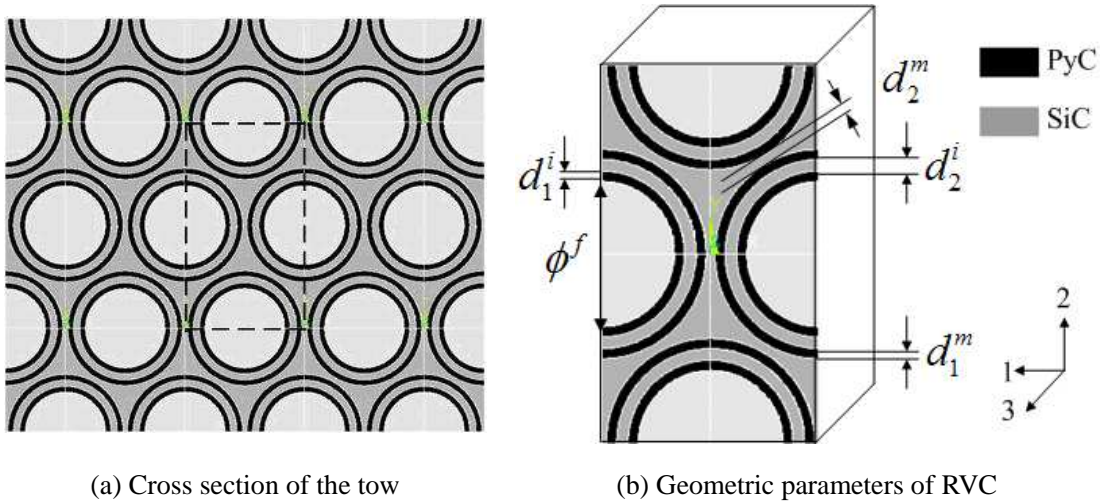


Figure 3.2 Geometric model of RVC of 2-D woven C/SiC composite on the fiber scale

A RVC model with  $n^i$  layers of interfaces and  $n^m$  layers of matrices can be adequately described by the following characteristic parameters:

- fiber diameter:  $\phi^f$
- layer thickness of interfaces :  $d_j^i$  ( $j = 1, 2, \dots, n^i$ )
- layer thickness of matrices :  $d_j^m$  ( $j = 1, 2, \dots, n^m$ )

Denote  $V_{fiber}^{Fiber}$ ,  $V_{interface,j}^{Fiber}$  and  $V_{matrix,j}^{Fiber}$  to be the fiber volume fraction, the  $j$ th interface

layer volume fraction (  $j=1, 2, \dots, n^i$  ) and the  $j$ th matrix layer volume fraction (  $j=1, 2, \dots, n^m$  ) for the RVC model on the fiber scale, respectively. According to Figure 3.2b, following expressions can be then derived to evaluate the volume fractions of fiber, interfaces and matrix layers

$$V_{fiber}^{Fiber} = \frac{\pi(\phi^f)^2}{2\sqrt{3}\left(\phi^f + 2\sum_{k=1}^{n^i} d_k^i + 2\sum_{k=1}^{n^m-1} d_k^m + d_{n^m}^m\right)^2} \quad (3.1)$$

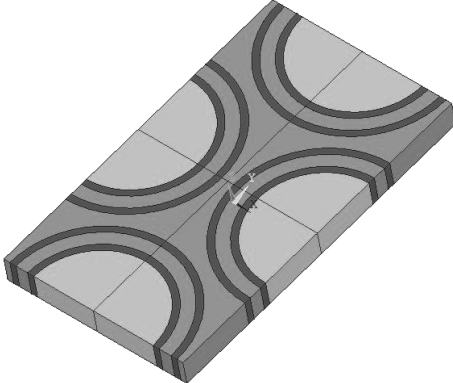
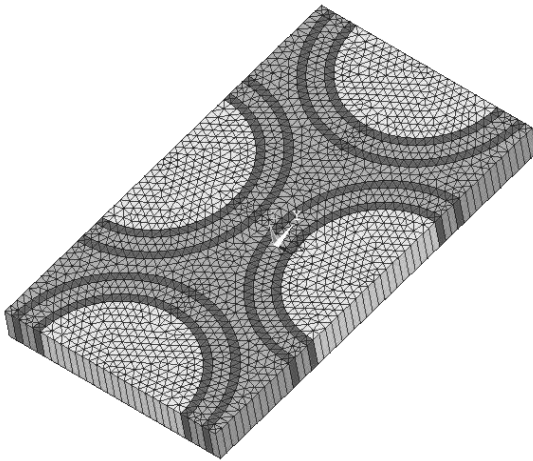
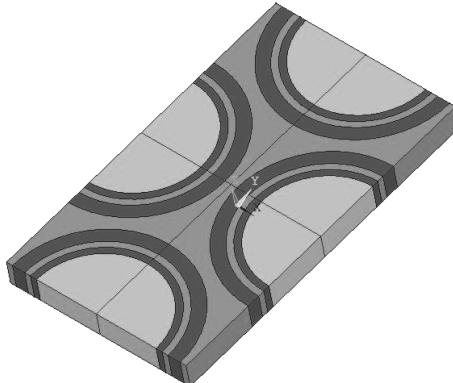
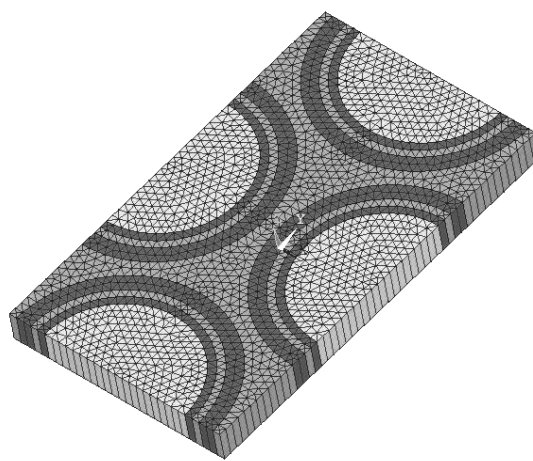
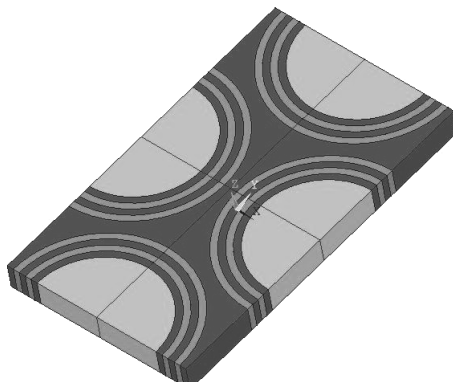
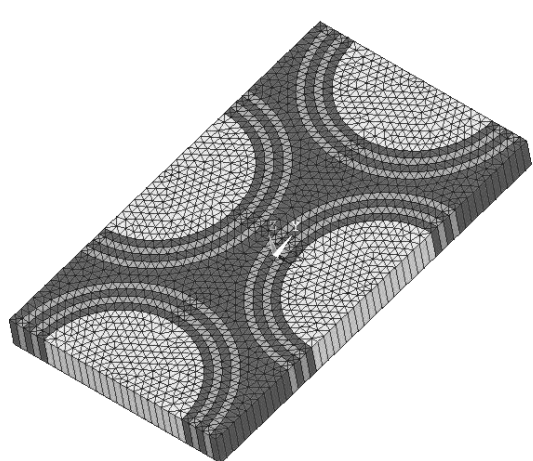
$$V_{interface,j}^{Fiber} = \frac{\pi\left(\phi^f + \sum_{k=1}^j d_k^i\right)^2 - \pi\left(\phi^f + \sum_{k=1}^{j-1} d_k^i\right)^2}{2\sqrt{3}\left(\phi^f + 2\sum_{k=1}^{n^i} d_k^i + 2\sum_{k=1}^{n^m-1} d_k^m + d_{n^m}^m\right)^2}, \quad j \leq n^i \quad (3.2)$$

$$V_{matrix,j}^{Fiber} = \frac{\pi\left(\phi^f + \sum_{k=1}^{n^i} d_k^i + \sum_{k=1}^j d_k^m\right)^2 - \pi\left(\phi^f + \sum_{k=1}^{n^i} d_k^i + \sum_{k=1}^{j-1} d_k^m\right)^2}{2\sqrt{3}\left(\phi^f + 2\sum_{k=1}^{n^i} d_k^i + 2\sum_{k=1}^{n^m-1} d_k^m + d_{n^m}^m\right)^2}, \quad j < n^m \quad (3.3)$$

$$V_{matrix,j}^{Fiber} = \frac{2\sqrt{3}\left(\phi^f + 2\sum_{k=1}^{n^i} d_k^i + 2\sum_{k=1}^{n^m-1} d_k^m + d_{n^m}^m\right)^2 - \pi\left(\phi^f + \sum_{k=1}^{n^i} d_k^i + \sum_{k=1}^{j-1} d_k^m\right)^2}{2\sqrt{3}\left(\phi^f + 2\sum_{k=1}^{n^i} d_k^i + 2\sum_{k=1}^{n^m-1} d_k^m + d_{n^m}^m\right)^2}, \quad j = n^m \quad (3.4)$$

Table 3.1 lists the geometric and finite element models for three fiber-scale RVCs with different characteristic parameters. The fiber diameters of the RVCs are all  $10\mu m$ . Here, twenty-node prismatic solid element SOLID95 of *ANSYS* software is used for the finite element discretization.

Table 3.1 RVC models with different characteristic parameters on the fiber scale

Geometric model ( $\mu m$ )	Finite element model
 <p><math>d_1^i = 0.5, d_2^i = 1.0, d_1^m = 0.5, d_2^m = 1.0</math></p>	
 <p><math>d_1^i = 0.5, d_2^i = 0.5, d_1^m = 1.0, d_2^m = 1.0</math></p>	
 <p><math>d_1^i = 0.5, d_2^i = 0.5, d_1^m = 0.5, d_2^m = 0.5, d_3^m = 1.0</math></p>	

### 3.2.2 Tow scale

The tow scale concerns the modelling of RVC for 2-D plain woven composites. 2-D plain

woven fabric is the most commonly used reinforcement form in 2-D woven fabric composites. Plain woven fabric is formed by interlacing (weaving) of tows. The tows in the longitudinal direction are known as warp tows. The tows in the transverse direction are known as fill tows. Figures 3.3 and 3.4 respectively shows the scanning electron microscope (SEM) photograph and the schematic representation of a typical 2-D plain woven perform.

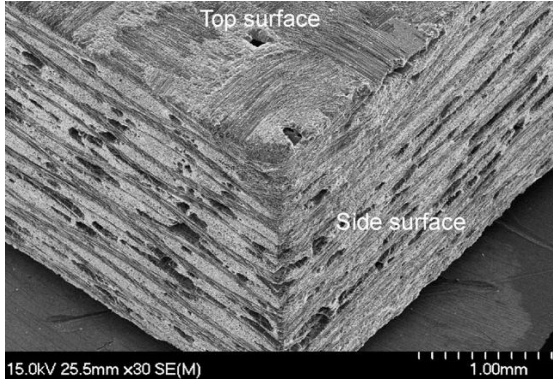


Figure 3.3 SEM photograph of the 2-D plain woven perform

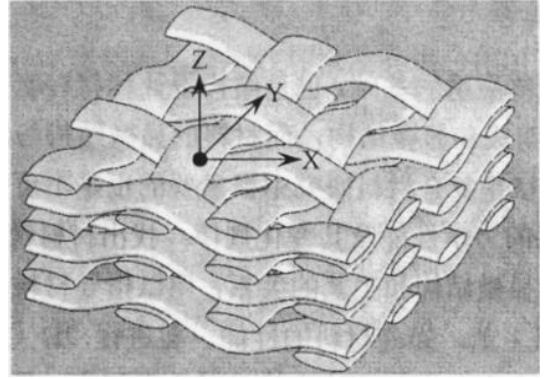


Figure 3.4 Schematic representation of the 2-D plain woven perform

Due to the geometrical complexity of the multi-layer woven architecture, following assumptions are adopted to simplify the finite element modelling and improve the computing efficiency:

- Cross-sections of the fill and warp tows are assumed to be rectangular.
- The undulating form is approximated by a single average undulation angle with the horizontal plane.

Figure 3.5 shows the geometric model of RVC on the tow scale consisting of three layers of matrices. Related geometric parameters are: width of warp tow  $a_w$ , width of fill tow  $a_f$ , thickness of warp tow  $h_w$ , thickness of fill tow  $h_f$ , thicknesses of the first and second matrices  $t_1^m$  and  $t_2^m$ , average undulation angle with the horizontal plane  $\theta$ .

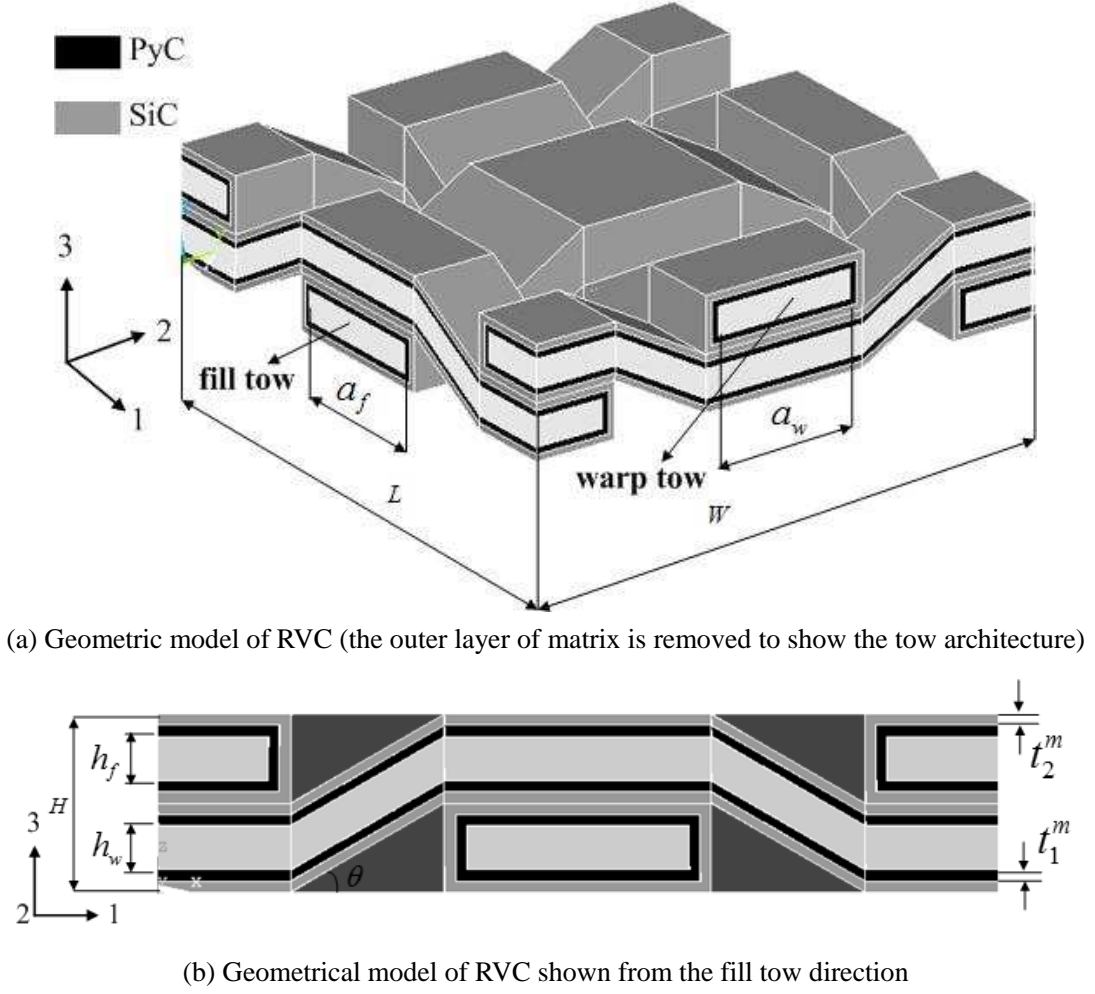


Figure 3.5 Geometric model of RVC of 2-D woven C/SiC composite on the tow scale

In a general case, the RVC model of 2-D woven C/SiC composites with  $n^m$  layers of matrices on the tow scale can be adequately described by the following characteristic parameters:

- the width of warp tow:  $a_w$ ,
- the width of fill tow:  $a_f$ ,
- the thickness of warp tow:  $h_w$ ,
- the thickness of fill tow:  $h_f$ ,
- the average undulation angle with the horizontal plane  $\theta$ ,
- the thickness of each matrix layer  $t_j^m$  ( $j = 1, 2, \dots, n^m - 1$ ).

Length ( $L$ ), width ( $W$ ) and height ( $H$ ) of the RVC can be expressed as follows

$$\begin{aligned}
 L &= 2[a_f + 2\sum_{j=1}^{n^m-1} t_j^m] + 2\left(h_w + \sum_{j=1}^{n^m-1} t_j^m\right) / \tan \theta \\
 W &= 2[a_w + 2\sum_{j=1}^{n^m-1} t_j^m] + 2\left(h_f + \sum_{j=1}^{n^m-1} t_j^m\right) / \tan \theta \\
 H &= h_f + h_w + 4\sum_{j=1}^{n^m-1} t_j^m
 \end{aligned} \tag{3.5}$$

Denote  $V_{tow}^{Tow}$  and  $V_{matrix,j}^{Tow}$  to be the tow volume fraction and the  $j$ th matrix layer volume fraction ( $j = 1, 2, \dots, n^m$ ) for the RVC model on the tow scale, respectively. According to Figure 3.5 and classical geometrical properties,  $V_{tow}^{Tow}$  and  $V_{matrix,j}^{Tow}$  can be obtained as

$$V_{tow}^{Tow} = \frac{4a_w h_w \left[ a_w + h_w + 2\sum_{k=1}^{n^m-1} t_k^m (1 + ctg\theta) \right]}{LWH} + \frac{4a_f h_f \left[ a_f + h_f + 2\sum_{k=1}^{n^m-1} t_k^m (1 + ctg\theta) \right]}{LWH} \tag{3.6}$$

$$\begin{aligned}
 V_{matrix,j}^{Tow} &= \frac{4\left(a_w + 2\sum_{k=1}^j t_k^m\right)\left(h_w + 2\sum_{k=1}^j t_k^m\right)\left[a_w + h_w + 4\sum_{k=1}^j t_k^m + 2\sum_{k=1}^j t_k^m (1 + ctg\theta)\right]}{LWH} + \\
 &\quad \frac{4\left(a_f + 2\sum_{k=1}^j t_k^m\right)\left(h_f + 2\sum_{k=1}^j t_k^m\right)\left[a_f + h_f + 4\sum_{k=1}^j t_k^m + 2\sum_{k=1}^j t_k^m (1 + ctg\theta)\right]}{LWH}, j < n^m
 \end{aligned} \tag{3.7}$$

$$V_{matrix,j}^{Tow} = 1 - V_{tow}^{Tow} - \sum_{k=1}^{n^m-1} V_{matrix,k}^{Tow}, \quad j = n^m \tag{3.8}$$

On the tow scale, the finite element model of RVC with three layers of matrices is depicted in Figure 3.6. Here, ten-node tetrahedral solid element SOLID187 is used for the discretization. The finite element models of both tows and matrices are shown, respectively.



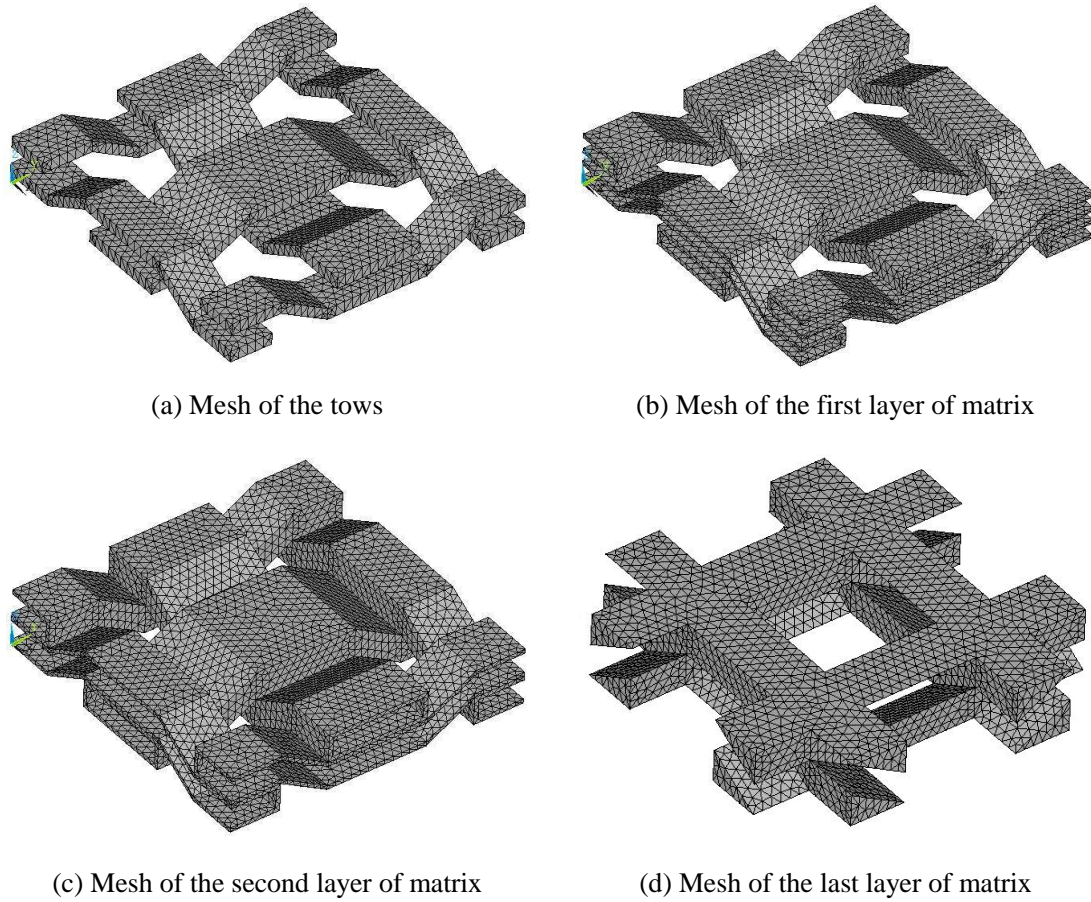


Figure 3.6 Finite element model of RVC of 2-D woven C/SiC composite on the tow scale

### 3.3 Microstructure modelling of 3-D braided C/SiC composites

#### 3.3.1 Fiber scale

In fact, the fiber-scale RVC model of 3-D braided C/SiC composites is the same as that of 2-D woven C/SiC composites. Hence, the details of the microstructural modelling of the RVC, which can be referred in the above section, are not discussed here.

#### 3.3.2 Tow scale

Over the last decades, extensive investigations have been mainly carried out [82-86] about the modelling of 3-D braided composites. 4-step method is widely used as the basic forming technique of 3-D braiding composites. In the 4-step braiding process, the braider tows are intertwined through their relative displacements. The braiding pattern is termed 1×1 because



of the identical distance traveled by all the rows or columns in each step. Four steps of motion constitute one machine cycle which will braid the tows. As these steps of motion are repeated, the tows move throughout the cross-section and are interlaced to form the braided structure. More details about the 4-step braiding process can be found in the literature [82, 85].

Due to the geometrical complexity of braided composite, following assumptions were introduced by Xu et al. [35] to simplify the finite element modeling and improve the computing efficiency:

- The tow cross-section is hexagonal and identical for all the tows.
- The braiding process is quite stable so that the braided structure is uniform and all the tows are straight within the braided preform.

Here, the problem is concerned with the modeling of 3-D braided composites with multi-layer matrices that have a microstructure much complex due to the spatial multi-layer architecture and the large heterogeneity of multi-phase materials. With the extension of above assumptions, a RVC model for 3-D braided C/SiC composites with multi-layer matrices is presented for the first time.

As illustrated in Figure 3.7, three parameters  $a$ ,  $b$  and  $\beta$  are basically needed to define a hexagonal cross-section of the tow. Furthermore, the Z-directional cross-section of the 3-D braided C/SiC composite is depicted in Figure 3.7 where the multi-layer matrices are removed to show the interlaced tow architecture. The RVC model is indicated with a solid rectangular frame.

It was demonstrated [85] that all the interlaced tows of the 3-D 4-step braided composites are distributed within two families of planes that are orthogonal to each other and have an orientation of  $\pm 45^\circ$  with respect to the preform surface of  $XOZ$ . Meanwhile, both families consist of a set of parallel planes as shown in Figure 3.7. Within these planes, the distribution characteristics of tows are distinct. For this reason, an “analysis unit” marked by a dotted rectangular frame in Figure 3.7 is created within the local coordinate system  $O'X'Y'Z'$  to favor the geometrical analysis of braided preform. Within the “analysis unit”, the interlaced tows are distributed within the mutually perpendicular plane families and parallel to the

surfaces of “analysis unit”. Compared with the RVC model, it is easier to describe the geometry of braided preform by using the “analysis unit”. The link between “analysis unit” and RVC model is illustrated in Figure 3.7. In practice, the “analysis unit” will be firstly created and the RVC model can be obtained via Boolean operation.

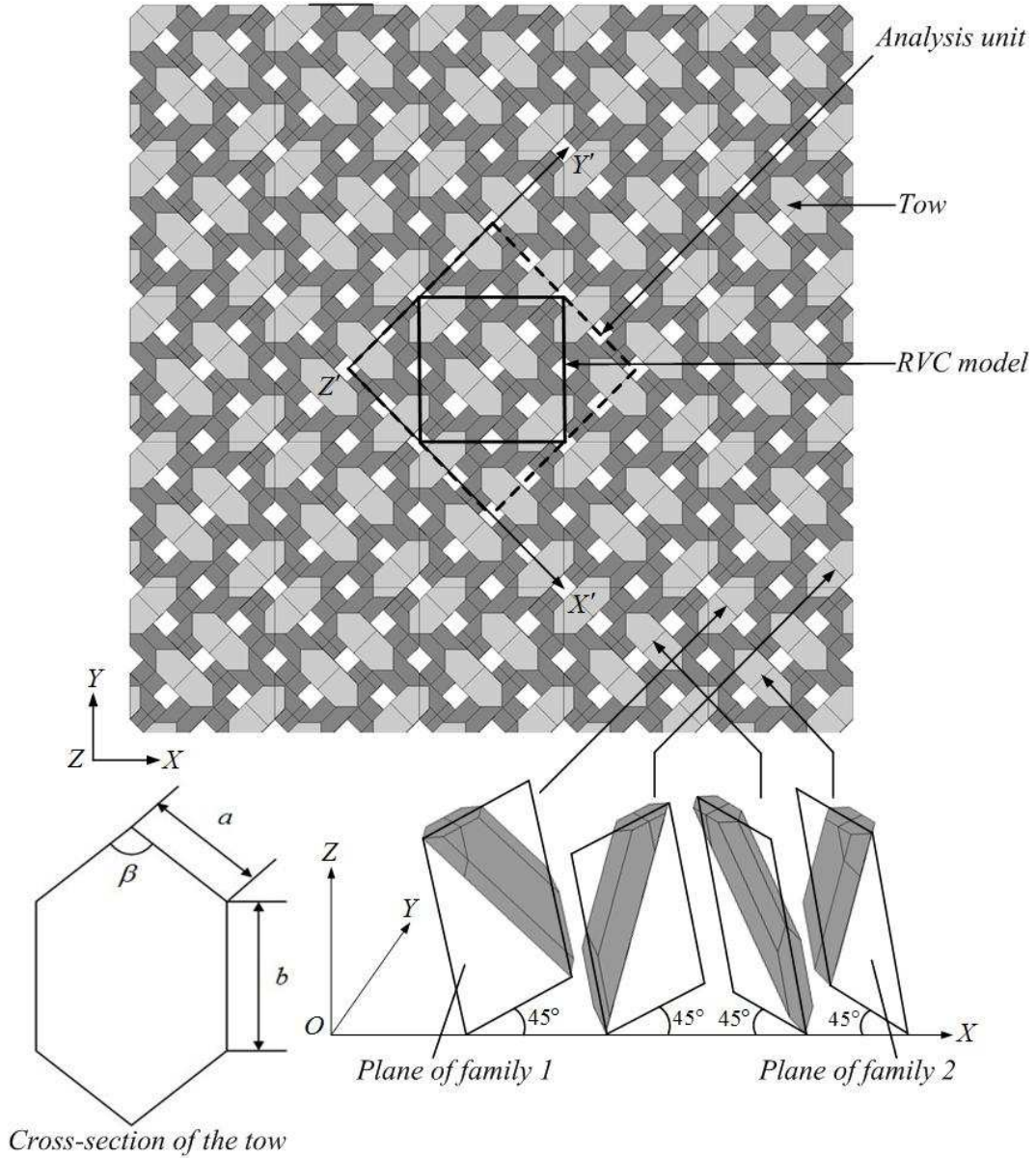


Figure 3.7 Z-directional cross-section of the 3-D 4-step braided C/SiC composite

As shown in Figure 3.8, the “analysis unit” can be further divided into eight equal cuboids and only two of them are non-identical cuboids (denoted as sub-cell A and sub-cell B, respectively) which can be re-assembled into the “analysis unit” in an alternating manner. Inside the “analysis unit”, the tow axes indicated with thick solid lines in Figure 3.8b and

Figure 3.8c are all straight and do not intersect each other in the space.

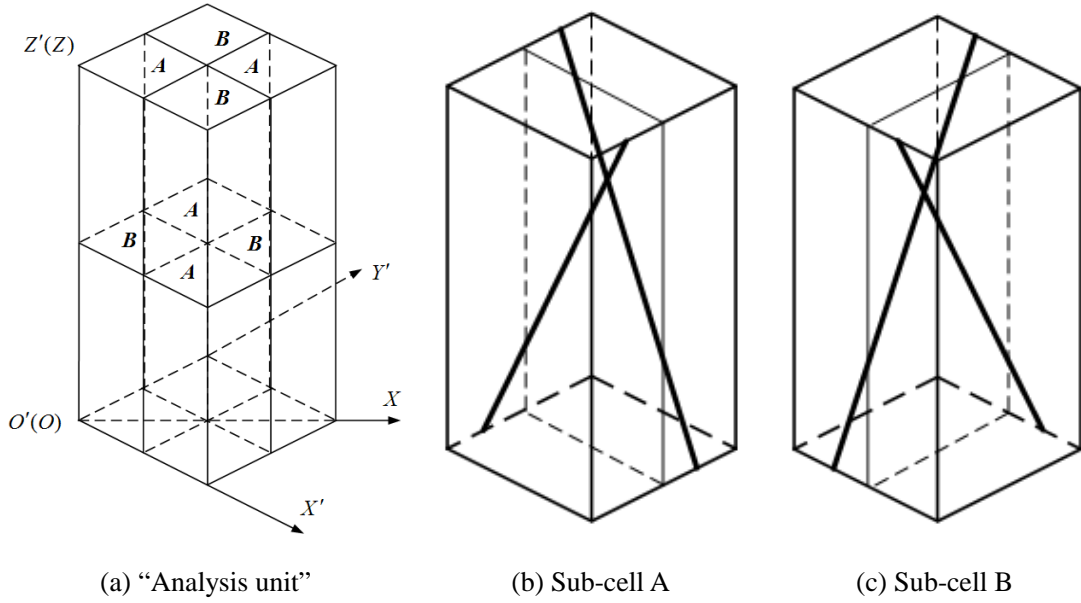


Figure 3.8 Division of the "Analysis unit"

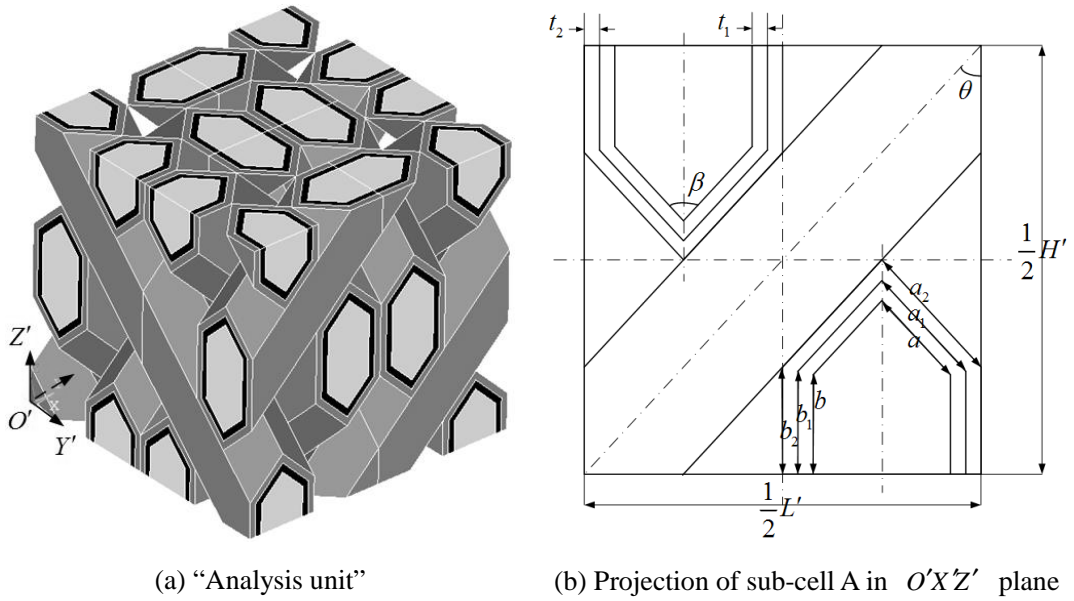


Figure 3.9 Geometry of "Analysis unit"

The geometrical characteristics of the "analysis unit" can be obtained from the sub-cell analysis. Figure 3.9a shows the "analysis unit" of the 3-D 4-step braided C/SiC composite consisting of three layers of matrices (different colors represent different material phases). Note that the last layer of the matrix is removed to show the internal tow architecture. Sub-cell A is illustrated in Figure 3.9b. Related geometric parameters are:  $\theta$ , braiding angle;

$a$ ,  $b$  and  $\beta$ , parameters of the cross-section of tows;  $a_1$ ,  $b_1$ ,  $a_2$  and  $b_2$ , parameters of the cross-section of the first and second matrix layers;  $t_1^m$  and  $t_2^m$ , thicknesses of the first and second layers of matrices;  $L'$  and  $H'$ , length and height of the “analysis unit”.

From Figure 3.9b, we have the following geometric relation

$$\beta = 2\theta \quad (3.9)$$

For the cross-section of the first and second matrix layers,  $a_1$  and  $a_2$  can be expressed in terms of  $\theta$ ,  $a$ ,  $t_1^m$  and  $t_2^m$  as follows

$$a_1 = a + t_1^m \left( \frac{1}{\tan \theta} + \tan \frac{1}{2} \theta \right) \quad (3.10)$$

$$a_2 = a + (t_1^m + t_2^m) \left( \frac{1}{\tan \theta} + \tan \frac{1}{2} \theta \right) \quad (3.11)$$

For the cross-sections of the matrix layers and tows,  $b_1$ ,  $b_2$  and  $b$  can be obtained in terms of  $\theta$ ,  $a$ ,  $t_1^m$  and  $t_2^m$

$$b_2 = \left( a + (t_1^m + t_2^m) \left( \tan \theta + \tan \frac{1}{2} \theta \right) \right) \cos \theta \quad (3.12)$$

$$b_1 = \left( a + (t_1^m + t_2^m) \left( \tan \theta + \tan \frac{1}{2} \theta \right) \right) \cos \theta - t_2^m \tan \frac{1}{2} \theta \quad (3.13)$$

$$b = \left( a + (t_1^m + t_2^m) \left( \tan \theta + \tan \frac{1}{2} \theta \right) \right) \cos \theta - (t_1^m + t_2^m) \tan \frac{1}{2} \theta \quad (3.14)$$

The length and width of the “analysis unit” are expressed as

$$L' = 4 \left( a + (t_1^m + t_2^m) \left( \frac{1}{\tan \theta} + \tan \frac{1}{2} \theta \right) \right) \sin \theta \quad (3.15)$$

$$H' = 8 \left( a + (t_1^m + t_2^m) \left( \frac{1}{\tan \theta} + \tan \frac{1}{2} \theta \right) \right) \cos \theta \quad (3.16)$$

Obviously, length ( $L$ ) and width ( $H$ ) of the RVC model can be written as

$$L = 2\sqrt{2} \left( a + (t_1^m + t_2^m) \left( \frac{1}{\tan \theta} + \tan \frac{1}{2} \theta \right) \right) \sin \theta \quad (3.17)$$

$$H = 8 \left( a + (t_1^m + t_2^m) \left( \frac{1}{\tan \theta} + \tan \frac{1}{2} \theta \right) \right) \cos \theta \quad (3.18)$$

The corresponding RVC model is illustrated in Figure 3.10.

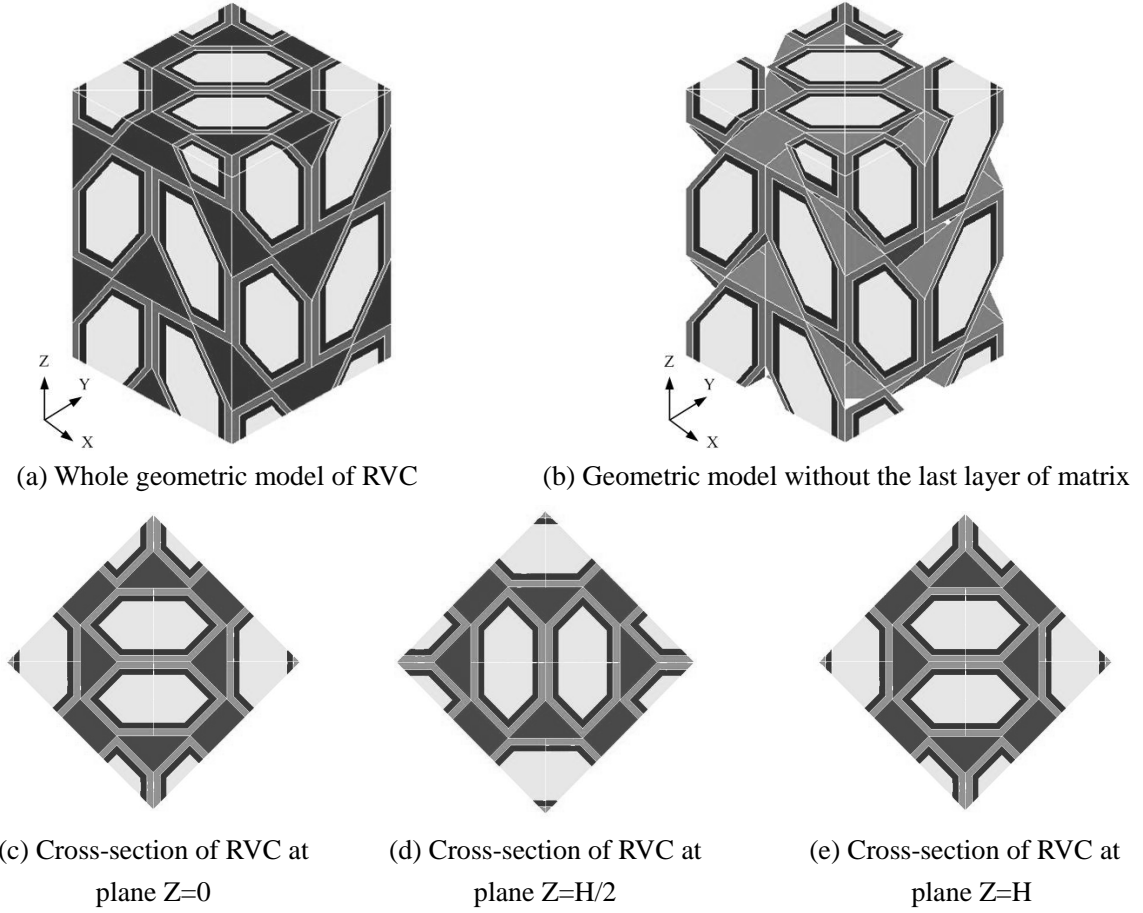


Figure 3.10 Geometrical model of RVC of 3-D braided C/SiC composite on the tow scale

It can be demonstrated that the braiding angle  $\theta$ , tow cross-section parameter  $a$  and each layer thickness of the matrix  $t_j^m$  ( $j=1, 2, \dots, n^m-1$ ) can be used to adequately describe the RVC model with  $n^m$  layers of matrices. With reference to equations (3.10)-(3.18), related geometric parameters are

$$b = \left( a + \sum_{k=1}^{n^m-1} t_k^m \left( \tan \theta + \tan \frac{1}{2} \theta \right) \right) \cos \theta - \sum_{k=1}^{n^m-1} t_k^m \tan \frac{1}{2} \theta \quad (3.19)$$

$$a_j = a + \sum_{k=1}^j t_k^m \left( \frac{1}{\tan \theta} + \tan \frac{1}{2} \theta \right) \quad (3.20)$$

$$b_j = \left( a + \sum_{k=1}^{n^m-1} t_k^m \left( \tan \theta + \tan \frac{1}{2} \theta \right) \right) \cos \theta - \left( \sum_{k=1}^{n^m-1} t_k^m - \sum_{k=1}^j t_k^m \right) \tan \frac{1}{2} \theta \quad (3.21)$$

$$L = 2\sqrt{2} \left( a + \sum_{k=1}^{n^m-1} t_k^m \left( \frac{1}{\tan \theta} + \tan \frac{1}{2} \theta \right) \right) \sin \theta \quad (3.22)$$

$$H = 8 \left( a + \sum_{k=1}^{n^m-1} t_k^m \left( \frac{1}{\tan \theta} + \tan \frac{1}{2} \theta \right) \right) \cos \theta \quad (3.23)$$

Note that  $a_j$  and  $b_j$  are parameters associated with the cross-section of the  $j$ th ( $j = 1, 2, \dots, n^m - 1$ ) matrix layer.

Now, denote  $V_{tow}^{Tow}$  and  $V_{matrix,j}^{Tow}$  to be the tow volume fraction and the  $j$ th matrix layer volume fraction ( $j = 1, 2, \dots, n^m$ ) for the RVC model on the tow scale, respectively. According to Figure 3.7,  $V_{tow}^{Tow}$  and  $V_{matrix,j}^{Tow}$  can be obtained as

$$V_{tow}^{Tow} = A_{tow} / A_c \quad (3.24)$$

$$V_{matrix,j}^{Tow} = A_{matrix,j} / A_c \quad (3.25)$$

where  $A_{tow}$  and  $A_{matrix,j}$  are the cross-section areas of the tow and the  $j$ th matrix layer along the braid-direction, respectively.  $A_c$  is the Z-directional cross-section area of RVC model.

$$\begin{aligned} A_{tow} &= 4 \left( 2a^2 \sin \theta \cos \theta + 2ab \sin \theta \right) \tan \theta \\ &= 8a \frac{\sin^2 \theta}{\cos \theta} \left( a \cos \theta + \left( a + \sum_{k=1}^{n^m-1} t_k^m \left( \tan \theta + \tan \frac{1}{2} \theta \right) \right) \cos \theta - \sum_{k=1}^{n^m-1} t_k^m \tan \frac{1}{2} \theta \right) \end{aligned} \quad (3.26)$$

$$\begin{aligned} A_c &= L^2 \\ &= 8 \left( a + \sum_{k=1}^{n^m-1} t_k^m \left( \frac{1}{\tan \theta} + \tan \frac{1}{2} \theta \right) \right)^2 \sin^2 \theta \end{aligned} \quad (3.27)$$

$$\begin{aligned} A_{matrix,j} &= 4 \left( 2a_j^2 \sin \theta \cos \theta + 2a_j b_j \sin \theta \right) \tan \theta - A_{tow} \\ &= 8a_j \frac{\sin^2 \theta}{\cos \theta} \left( a_j \cos \theta + \left( a + \sum_{k=1}^{n^m-1} t_k^m \left( \tan \theta + \tan \frac{1}{2} \theta \right) \right) \cos \theta \right. \\ &\quad \left. - \sum_{k=1}^{n^m-1} t_k^m \tan \frac{1}{2} \theta \right) - A_{tow}, \quad j = 1 \end{aligned} \quad (3.28)$$

$$\begin{aligned}
 A_{matrix,j} &= 4(2a_j^2 \sin \theta \cos \theta + 2a_j b_j \sin \theta) \tan \theta - A_{matrix,j-1} \\
 &= 8a_j \frac{\sin^2 \theta}{\cos \theta} \left( a_j \cos \theta + \left( a + \sum_{k=1}^{n^m-1} t_k^m \left( \tan \theta + \tan \frac{1}{2} \theta \right) \right) \cos \theta \right. \\
 &\quad \left. - \left( \sum_{k=1}^{n^m-1} t_k^m - \sum_{k=1}^j t_k^m \right) \tan \frac{1}{2} \theta \right) - A_{matrix,j-1}, \quad 2 \leq j \leq n^m - 1
 \end{aligned} \tag{3.29}$$

$$A_{matrix,j} = A_c - A_{tow} - \sum_{k=1}^{n^m-1} A_{matrix,k}, \quad j = n^m \tag{3.30}$$

By replacing  $A_{tow}$ ,  $A_{matrix,j}$  and  $A_c$  into equations (3.24) and (3.25), one obtains volume fractions of tow and matrix layers for the RVC model on the tow scale.

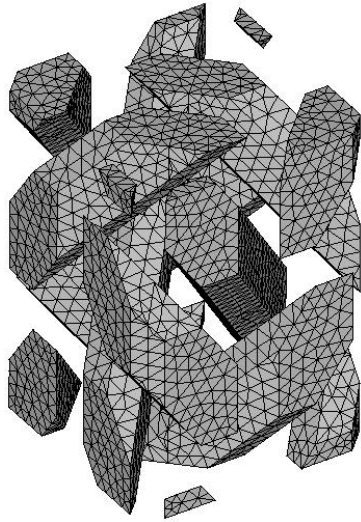
$$V_{tow}^{Tow} = \frac{a \left( a \cos \theta + \left( a + \sum_{k=1}^{n^m-1} t_k^m \left( \tan \theta + \tan \frac{1}{2} \theta \right) \right) \cos \theta - \sum_{k=1}^{n^m-1} t_k^m \tan \frac{1}{2} \theta \right)}{\left( a + \sum_{k=1}^{n^m-1} t_k^m \left( \frac{1}{\tan \theta} + \tan \frac{1}{2} \theta \right) \right)^2 \cos \theta} \tag{3.31}$$

$$\begin{aligned}
 V_{matrix,j}^{Tow} &= \frac{a \left( a \cos \theta + \left( a + \sum_{k=1}^{n^m-1} t_k^m \left( \tan \theta + \tan \frac{1}{2} \theta \right) \right) \cos \theta - \sum_{k=1}^{n^m-1} t_k^m \tan \frac{1}{2} \theta \right)}{\left( a + \sum_{k=1}^{n^m-1} t_k^m \left( \frac{1}{\tan \theta} + \tan \frac{1}{2} \theta \right) \right)^2 \cos \theta} \\
 &\quad - V_f^{tow}, \quad j = 1
 \end{aligned} \tag{3.32}$$

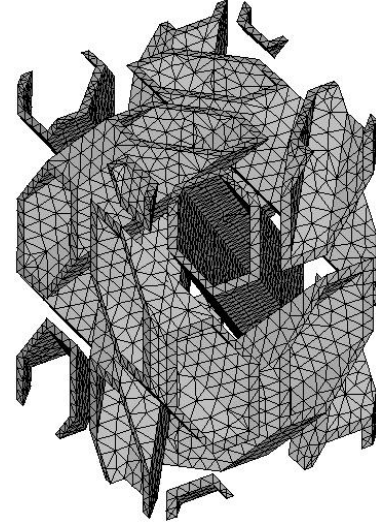
$$\begin{aligned}
 V_{matrix,j}^{Tow} &= \frac{a_j \left( a_j \cos \theta + \left( a + \sum_{k=1}^{n^m-1} t_k^m \left( \tan \theta + \tan \frac{1}{2} \theta \right) \right) \cos \theta - \left( \sum_{k=1}^{n^m-1} t_k^m - \sum_{k=1}^j t_k^m \right) \tan \frac{1}{2} \theta \right)}{\left( a + \sum_{k=1}^{n^m-1} t_k^m \left( \frac{1}{\tan \theta} + \tan \frac{1}{2} \theta \right) \right)^2 \cos \theta} \\
 &\quad - V_{matrix,j-1}^{Tow}, \quad 2 \leq j \leq n^m - 1
 \end{aligned} \tag{3.33}$$

$$V_{matrix,j}^{Tow} = 1 - V_{tow}^{Tow} - \sum_{k=1}^{n^m-1} V_{matrix,k}^{Tow}, \quad j = n^m \tag{3.34}$$

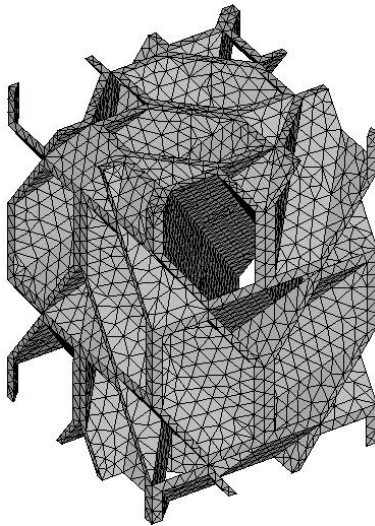
On the tow scale, the finite element model of RVC is depicted in Figure 3.11. Here, ten-node tetrahedral solid element SOLID187 is used for the discretization and the finite element models of both tows and matrices are shown, respectively.



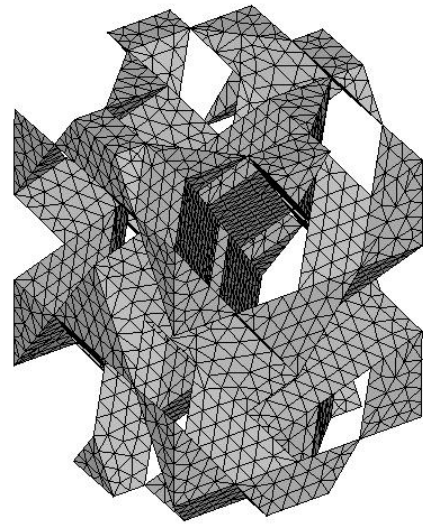
(a) Finite element model of the tow



(b) Finite element model of the first layer of the matrix



(c) Finite element model of the second layer of the matrix



(d) Finite element model of the last layer of the matrix

Figure 3.11 Finite element model of RVC of 3-D braided C/SiC composite on the tow scale

## 3.4 Prediction of the effective properties and comparison with experimental results

### 3.4.1 Two level evaluation strategy

Considering the two-scale characteristics of the RVC microstructures of C/SiC composites, the two-level evaluation strategy is used for the prediction of the effective properties. To



highlight the presentation, a flowchart is shown in Figure 3.12 to illustrate the stages involved in the two-level evaluation procedure.

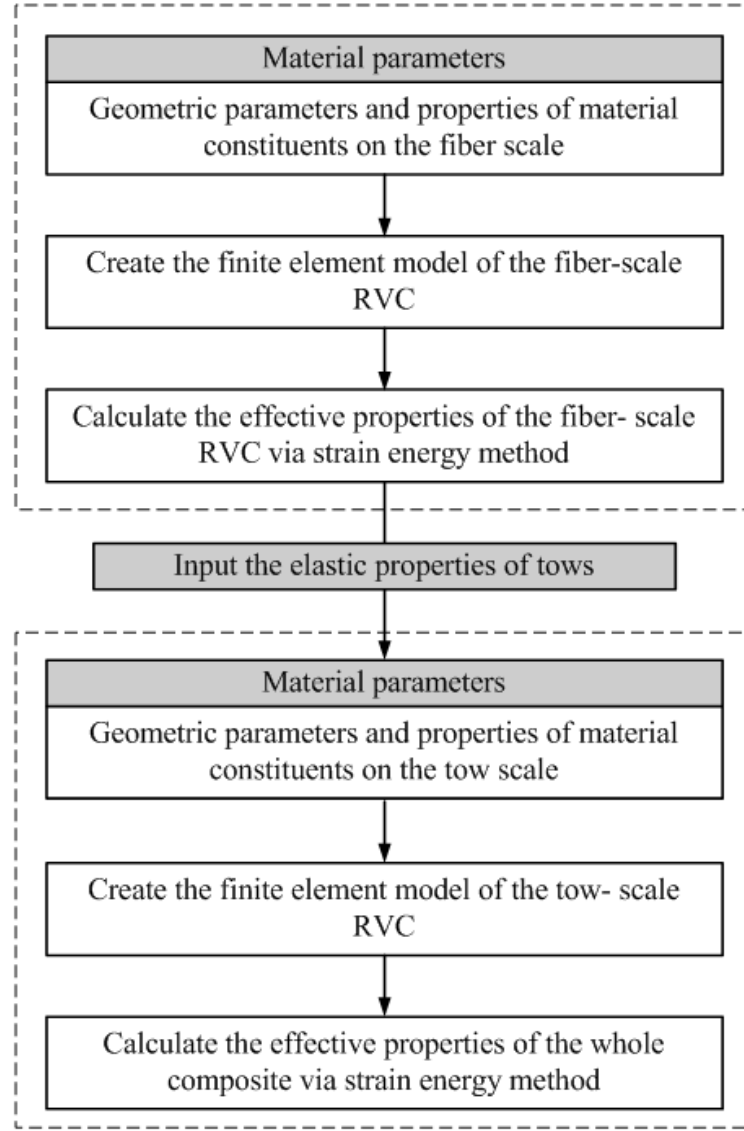


Figure 3.12 Illustration of the two-level evaluation procedure

- (a) On the fiber scale, finite element model of the RVC is built according to the geometrical parameters, i.e. the fiber diameter, numbers of interfaces and matrices layers and thicknesses of layers, and the properties of fiber, interfaces and matrices. The strain energy method (**chapter 2**) is then adopted to calculate the effective properties and the results are further used for the fiber tows that are treated as a homogeneous transversely isotropic material.
- (b) On the tow scale, the obtained properties of fiber tows through the first level of evaluation

and the properties of multi-layer matrices are combined with the geometrical parameters (the geometric size of tow's cross-section, the braiding angle and the matrix layers thicknesses) to generate the finite element model of the RVC. The strain energy method (**chapter 2**) is then adopted to evaluate effective properties of the whole composite.

### 3.4.2 Prediction of the effective elastic moduli

Two kinds of 2-D woven C/SiC samples (composites A and B) and two kinds of 3-D braided C/SiC samples (composites C and D) were prepared, respectively [87]. The in-plane (along directions 1 and 2, as shown in Figure 3.5a) extensional moduli of 2-D woven C/SiC samples and the through-thickness (along direction 3, i.e. direction Z shown in Figure 3.10a) extensional moduli of 3-D braided C/SiC samples were experimentally measured [87].

For each material phase, engineering moduli data taken from [87] are listed in Table 3.2 and the units of the modulus are all in GPa.

Table 3.2 Engineering moduli data for each material phase

	Extensional modulus			Shear modulus			Poisson ratio		
	$E_{11}$	$E_{22}$	$E_{33}$	$G_{12}$	$G_{23}$	$G_{13}$	$\nu_{12}$	$\nu_{23}$	$\nu_{13}$
Carbon fiber	22	22	220	7.75	4.8	4.8	0.42	0.12	0.12
PyC interface	12	12	30	4.3	2.0	2.0	0.4	0.12	0.12
SiC matrix	350	-	-	145.8			0.2	-	-

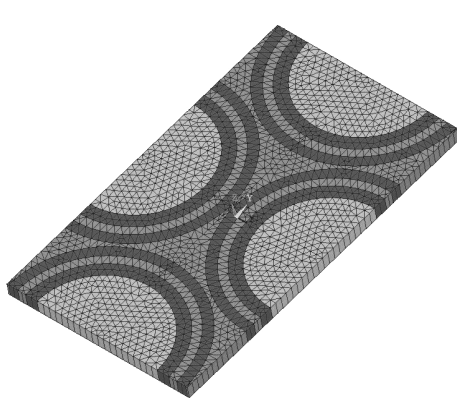
According to the infiltration processing time and volume fractions of constituent materials given in [87], geometrical parameters describing the two-scale RVC models of all the five composite samples are evaluated respectively. The finite element models of the RVCs are then generated and the effective elastic moduli of composite samples are computed by using the two-level evaluation strategy.

#### 3.4.2.1 Composite A

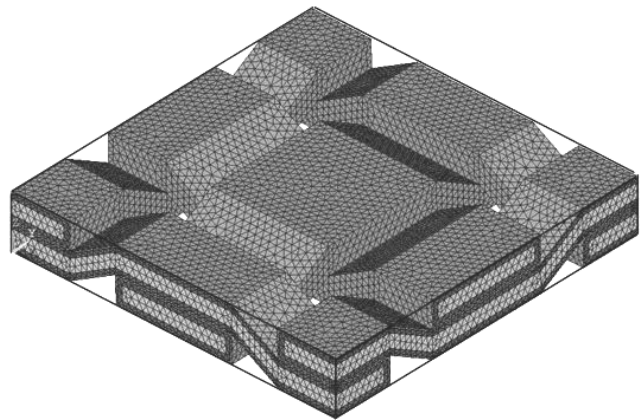
The finite element model of fiber-scale RVC model of composite A, depicted in Figure 3.13a, consists of two layers of alternate PyC and SiC interfaces and two layers of alternate PyC and SiC matrices. The values of the geometric parameters of the fiber-scale RVC are:  $\phi^f = 10\mu m$ ,

$$d_1^i = 0.95\mu m, \quad d_2^i = 0.66\mu m, \quad d_1^m = 0.75\mu m, \quad d_2^m = 0.28\mu m.$$

The finite element model of tow-scale RVC model of composite A, depicted in Figure 3.13b, consists of three layers of matrices made up of alternate PyC and SiC. The values of the geometric parameters of the tow-scale RVC are:  $a_w = a_f = 40mm$ ,  $h_w = h_f = 40mm$ ,  $\theta = 20^\circ$ ,  $t_1^m = 1.33mm$ ,  $t_2^m = 0.27mm$ .



(a) Fiber-scale RVC



(b) Tow-scale RVC (the outer layer of matrix is removed to show the tow architecture)

Figure 3.13 Finite element models of RVCs of composite A

The effective elastic tensors evaluated on two scales are listed in Table 3.3.

Table 3.3 Effective elastic tensors evaluated on two scales of composite A

Effective elastic tensors						
Fiber-scale (GPa)	51.7698					<i>sym</i>
	28.2846	51.7698				
	34.6923	34.6923	237.7509			
	0	0	0	11.7059		
	0	0	0	0	16.6635	
	0	0	0	0	0	16.6635
	142.5331					<i>sym</i>
Tow-scale (GPa)	28.0285	142.5331				
	23.3828	23.3828	63.8773			
	0	0	0	27.5855		
	0	0	0	0	14.6752	
	0	0	0	0	0	14.6752

Table 3.4 shows the predicted elastic moduli for composite A (the units of the moduli are all in GPa).

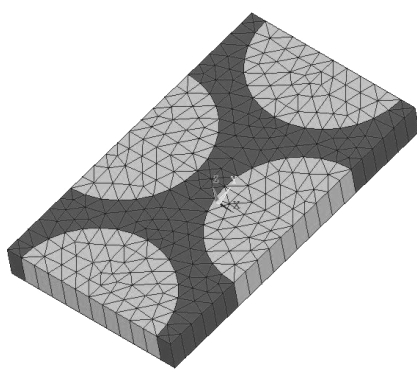
Table 3.4 Evaluated elastic moduli for composite A

In-plane extensional modulus		Through-thickness extensional modulus	Shear modulus			Poisson ratio		
$E_{11}$	$E_{22}$	$E_{33}$	$G_{12}$	$G_{23}$	$G_{31}$	$\nu_{12}$	$\nu_{23}$	$\nu_{13}$
131.1	131.1	57.5	27.6	14.7	14.7	0.15	0.31	0.31

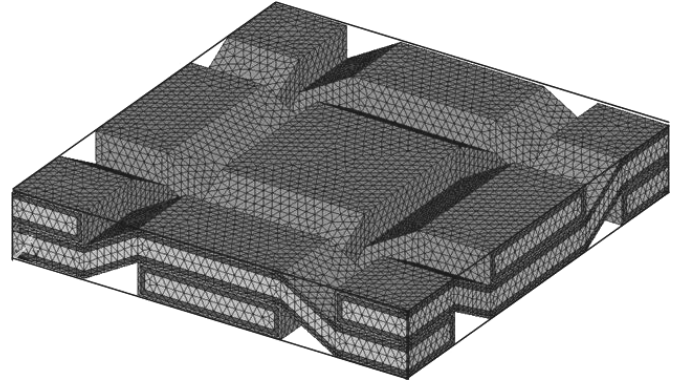
### 3.4.2.2 Composite B

The finite element model of fiber-scale RVC model of composite B, depicted in Figure 3.14a, consists only of one layer of PyC interface. The values of the geometric parameters of the fiber-scale RVC are:  $\phi^f = 10\mu m$ ,  $d_1^i = 2.0\mu m$ .

The finite element model of tow-scale RVC model of composite B, depicted in Figure 3.14b, consists of three layers of matrices made up of alternate PyC and SiC. The values of the geometric parameters of the tow-scale RVC are:  $a_w = a_f = 40mm$ ,  $h_w = h_f = 40mm$ ,  $\theta = 20^\circ$ ,  $t_1^m = 1.15mm$ ,  $t_2^m = 0.45mm$ .



(a) Fiber-scale RVC



(b) Tow-scale RVC (the outer layer of matrix is removed to show the tow architecture)

Figure 3.14 Finite element models of RVCs of composite B

The effective elastic tensors evaluated on two scales are listed in Table 3.5.

Table 3.5 Effective elastic tensors evaluated on two scales of composite B

Effective elastic tensors						
Fiber-scale (GPa)	27.1726					<i>sym</i>
	14.8055	27.1726				
	38.1594	38.1594	221.5768			
	0	0	0	6.1435		
	0	0	0	0	3.4023	
	0	0	0	0	0	3.4023
Tow-scale (GPa)	144.5562					<i>sym</i>
	33.2428	144.5562				
	24.7596	24.7596	61.6499			
	0	0	0	27.1362		
	0	0	0	0	13.0841	
	0	0	0	0	0	13.0841

Table 3.6 shows the predicted elastic moduli for composite B (the units of the moduli are all in GPa).

Table 3.6 Evaluated elastic moduli for composite B

In-plane extensional modulus		Through-thickness extensional modulus	Shear modulus			Poisson ratio		
$E_{11}$	$E_{22}$	$E_{33}$	$G_{12}$	$G_{23}$	$G_{31}$	$\nu_{12}$	$\nu_{23}$	$\nu_{13}$
130.6	130.6	54.8	27.1	13.1	13.1	0.17	0.33	0.33

### 3.4.2.3 Composite C

The finite element model of fiber-scale RVC model of composite C, depicted in Figure 3.15a, consists of two layers of alternate PyC and SiC interfaces and two layers of alternate PyC and SiC matrices. The values of the geometric parameters of the fiber-scale RVC are:  $\phi^f = 10\mu m$ ,  $d_1^i = 0.95\mu m$ ,  $d_2^i = 0.66\mu m$ ,  $d_1^m = 0.75\mu m$ ,  $d_2^m = 0.28\mu m$ .

The finite element model of tow-scale RVC model of composite C, depicted in Figure 3.15b, consists of three layers of matrices made up of alternate PyC and SiC. The values of the geometric parameters of the tow-scale RVC are:  $a = 5mm$ ,  $\theta = 22^\circ$ ,  $t_1^m = 0.815mm$ ,  $t_2^m = 0.31mm$ .

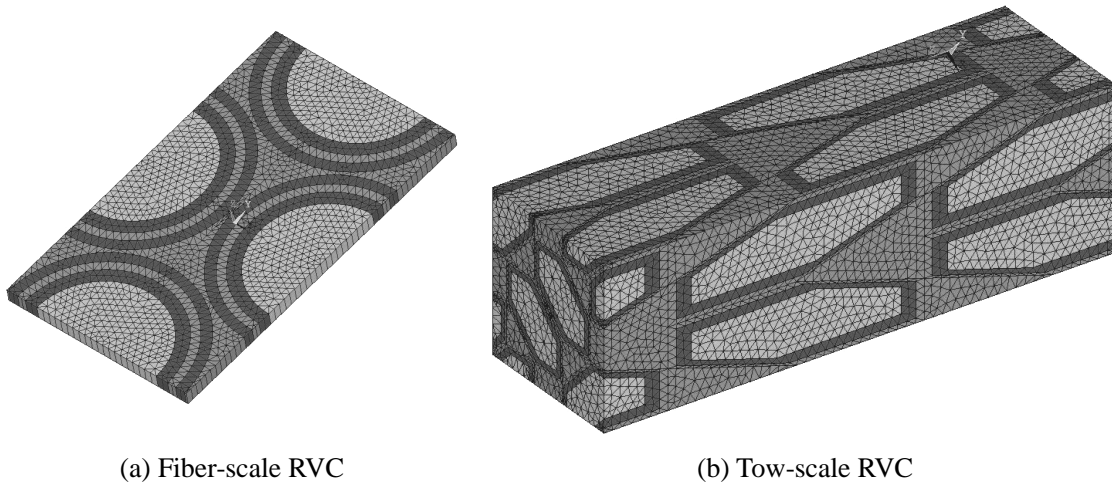


Figure 3.15 Finite element models of RVCs of composite C

The effective elastic tensors evaluated on two scales are listed in Table 3.7.

Table 3.7 Effective elastic tensors evaluated on two scales of composite C

Effective elastic tensors						
Fiber-scale (GPa)	51.7698					<i>sym</i>
	28.2846	51.7698				
	34.6923	34.6923	237.7509			
	0	0	0	11.7059		
	0	0	0	0	16.6635	
	0	0	0	0	0	16.6635
Tow-scale (GPa)	82.1278					<i>sym</i>
	33.3848	82.1278				
	35.5079	35.5079	185.8855			
	0	0	0	25.8121		
	0	0	0	0	37.1791	
	0	0	0	0	0	37.1791

Table 3.8 shows the predicted elastic moduli for composite C (the units of the moduli are all in GPa).

Table 3.8 Evaluated elastic moduli for composite C

In-plane extensional modulus		Through-thickness extensional modulus	Shear modulus			Poisson ratio		
$E_{11}$	$E_{22}$	$E_{33}$	$G_{12}$	$G_{23}$	$G_{31}$	$\nu_{12}$	$\nu_{23}$	$\nu_{13}$
65.9	65.9	164.1	25.8	37.2	37.2	0.35	0.12	0.12

#### 3.4.2.4 Composite D

The finite element model of fiber-scale RVC model of composite D, depicted in Figure 3.16a, consists only of one layer of PyC interface. The values of the geometric parameters of the fiber-scale RVC are:  $\phi^f = 10\mu m$ ,  $d_1^i = 2.0\mu m$ .

The finite element model of tow-scale RVC model of composite D, depicted in Figure 3.16b, consists of three layers of matrices made up of alternate PyC and SiC. The values of the geometric parameters of the tow-scale RVC are:  $a = 5mm$ ,  $\theta = 22^\circ$ ,  $t_1^m = 0.815mm$ ,  $t_2^m = 0.31mm$ .

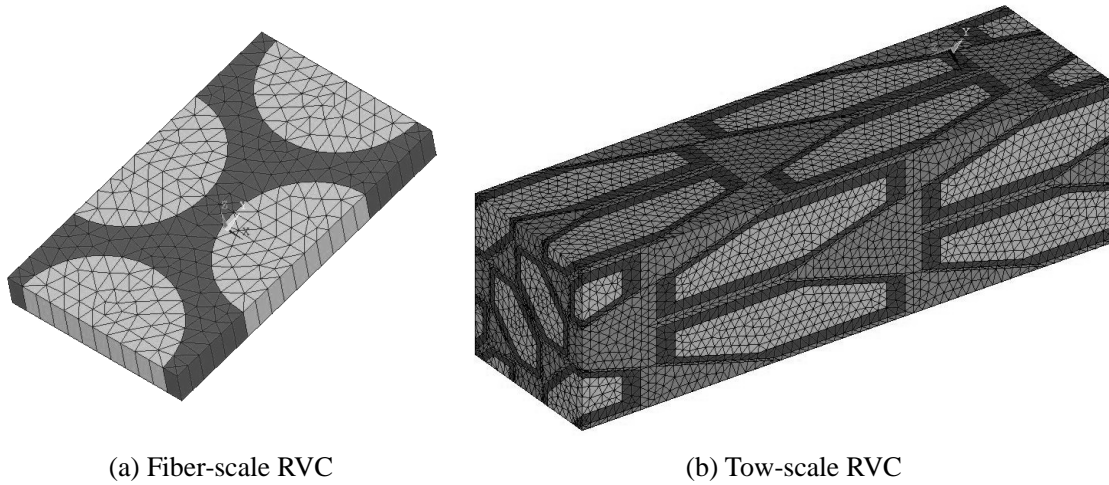


Figure 3.16 Finite element models of RVCs of composite D

The effective elastic tensors evaluated on two scales are listed in Table 3.9.

Table 3.9 Effective elastic tensors evaluated on two scales of composite D

Effective elastic tensors						
Fiber-scale (GPa)	27.1726					<i>sym</i>
	14.8055	27.1726				
	38.1594	38.1594	221.5768			
	0	0	0	6.1435		
	0	0	0	0	3.4023	
	0	0	0	0	0	3.4023
Tow-scale (GPa)	69.1071					<i>sym</i>
	27.8815	69.1071				
	33.6150	33.6150	169.4743			
	0	0	0	21.4189		
	0	0	0	0	31.6233	
	0	0	0	0	0	31.6233

Table 3.10 shows the predicted elastic moduli for composite D (the units of the moduli are all in GPa).

Table 3.10 Evaluated elastic moduli for composite D

In-plane extensional modulus		Through-thickness extensional modulus	Shear modulus			Poisson ratio		
$E_{11}$	$E_{22}$	$E_{33}$	$G_{12}$	$G_{23}$	$G_{31}$	$\nu_{12}$	$\nu_{23}$	$\nu_{13}$
55.2	55.2	146.2	21.4	31.6	31.6	0.34	0.13	0.13

### 3.4.3 Prediction of the effective CTEs

A 2-D woven C/SiC sample (composite E) and a 3-D braided C/SiC sample (composite F) were prepared [53]. The in-plane coefficient of thermal expansion (CTE) of composite E and the in-plane and through-thickness CTEs of composite F under different temperatures were investigated experimentally [53]. The thermo-elastic properties of the constituents under various temperatures are summarized in Table 3.11. The units of the modulus and CTE are in GPa and  $10^{-6}/^{\circ}\text{C}$ , respectively.



Table 3.11 Properties of the constituents under various temperatures

		Extensional modulus		Shear modulus		Poisson ratio		CTEs	
		$E_{11}, E_{22}$	$E_{33}$	$G_{12}$	$G_{23}, G_{31}$	$\nu_{12}$	$\nu_{23}, \nu_{31}$	$\alpha_{11}, \alpha_{22}$	$\alpha_{33}$
200°C	Carbon fiber	22	220	7.75	4.8	0.4	0.12	8.85	0.0
	SiC matrix	350	350	145.8	145.8	0.2	0.2	1.9	1.9
500°C	Carbon fiber	22	220	7.75	4.8	0.4	0.12	8.85	1.5
	SiC matrix	350	350	145.8	145.8	0.2	0.2	3.7	3.7
700°C	Carbon fiber	22	220	7.75	4.8	0.4	0.12	8.85	1.5
	SiC matrix	350	350	145.8	145.8	0.2	0.2	4.6	4.6
800°C	Carbon fiber	22	220	7.75	4.8	0.4	0.12	8.85	1.5
	SiC matrix	350	350	145.8	145.8	0.2	0.2	4.9	4.9

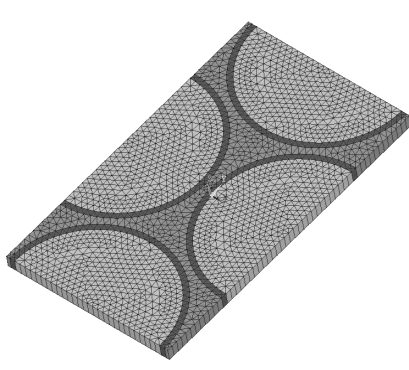
According to the infiltration processing time and volume fractions of constituent materials given in [53], geometrical parameters describing the RVC models of both two samples are evaluated respectively. Two-scale RVC finite element models are established and effective CTEs of composites are obtained based on the sequential computation from the fiber scale to the tow scale.

#### 3.4.3.1 Composite E

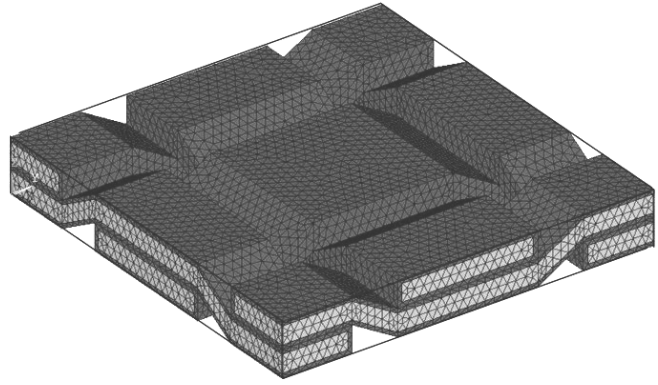
The finite element model of fiber-scale RVC model of composite E, depicted in Figure 3.17a, consists of one layer of PyC interface and one layer of SiC matrix. The values of the geometric parameters of the fiber-scale RVC are:  $\phi^f = 10\mu m$ ,  $d_1^i = 0.35\mu m$ ,  $d_1^m = 0.5\mu m$ .

The finite element model of tow-scale RVC model of composite E, depicted in Figure 3.17b, consists of two layers of matrices made up of alternate PyC and SiC. The values of the geometric parameters of the tow-scale RVC are:  $a_w = a_f = 40mm$ ,  $h_w = h_f = 40mm$ ,

$\theta = 20^\circ$ ,  $t_1^m = 0.65mm$ .



(a) Fiber-scale RVC



(b) Tow-scale RVC (the outer layer of matrix is removed to show the tow architecture)

Figure 3.17 Finite element models of RVCs of composite E

Table 3.12 shows the predicted in-plane CTEs of composite E under various temperatures.

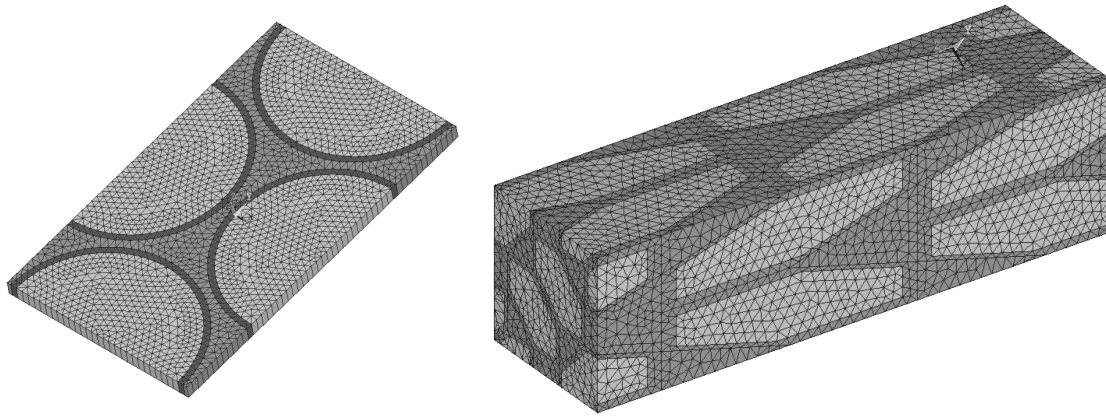
Table 3.12 Computed CTEs of composite E under various temperatures

	200°C	500°C	700°C	800°C
$\alpha_{11}, \alpha_{22} (10^{-6}/^{\circ}\text{C})$	1.05	3.13	4.26	5.17

#### 3.4.3.2 Composite F

The finite element model of fiber-scale RVC model of composite F, depicted in Figure 3.18a, consists of one layer of PyC interface and one layer of SiC matrix. The values of the geometric parameters of the fiber-scale RVC are:  $\phi^f = 10\mu\text{m}$ ,  $d_1^i = 0.35\mu\text{m}$ ,  $d_1^m = 0.5\mu\text{m}$ .

The finite element model of tow-scale RVC model of composite F, depicted in Figure 3.18b, consists of two layers of matrices made up of alternate PyC and SiC. The values of the geometric parameters of the tow-scale RVC are:  $a = 5\text{mm}$ ,  $\theta = 22^{\circ}$ ,  $t_1^m = 0.5\text{mm}$ .



(a) Fiber-scale RVC

(b) Tow-scale RVC

Figure 3.18 Finite element models of RVCs of composite F

Table 3.13 shows the predicted CTEs of composite F under various temperatures.

Table 3.13 Computed CTEs of composite F under various temperatures

	200°C	500°C	700°C	800°C
$\alpha_{11}, \alpha_{22} (10^{-6}/^{\circ}\text{C})$	3.31	4.63	5.18	5.38
$\alpha_{33} (10^{-6}/^{\circ}\text{C})$	1.79	3.26	3.64	3.77

### 3.4.4 Comparison with the experimental results

Tables 3.14 and 3.15 show the comparisons of measured and predicted elastic moduli and CTEs for the various samples respectively. It can be seen that the predicted results are in global agreement with the experimental data. The comparison proves that the proposed model and method is validated for the prediction of elastic and thermal expansion properties of C/SiC composites. However, it should be pointed out that because rudimental cavities generated within the composite for emission of large infiltrated by-products during the infiltration are not considered in this paper, there are some differences between numerical and experimental results.

Table 3.14 Comparison of computed moduli with experimental results [87]

Sample	In-plane extensional modulus		Through-thickness extensional modulus	
		$E_{11}, E_{22}$ (GPa)		$E_{33}$ (GPa)
A	Prediction	131.1		
	Experiment	109.3		
	Error	16.6%		
B	Prediction	130.6		
	Experiment	108.1		
	Error	17.2%		
C	Prediction			164.1
	Experiment			146.2
	Error			10.9%
D	Prediction			144.1
	Experiment			134.0
	Error			10.1%

Table 3.15 Comparison of computed CTEs with experimental results [53]

Sample			200°C	500°C	700°C	800°C
E	$\alpha_{11}, \alpha_{22}$ ( $10^{-6}/^{\circ}\text{C}$ )	Prediction	1.05	3.13	4.26	5.17
		Experiment	1.12	3.76	4.85	5.79
		Error	6.3%	16.8%	12.2%	10.7%
	$\alpha_{11}, \alpha_{22}$ ( $10^{-6}/^{\circ}\text{C}$ )	Prediction	3.31	4.63	5.18	5.38
		Experiment	3.76	5.31	6.08	6.53
		Error	11.9%	12.8%	14.8	17.6%
F	$\alpha_{33}$ ( $10^{-6}/^{\circ}\text{C}$ )	Prediction	1.79	3.26	3.64	3.77
		Experiment	1.67	3.02	3.98	4.70
		Error	7.2%	7.4%	8.5%	19.8%

### 3.5 Conclusions

In this chapter, microstructure modeling and prediction of the effective properties for 2-D woven and 3-D braided composites with multi-layer interfaces and matrices are presented. Due to the complex architecture of the microstructure, geometric parameters are defined in a closed-form to describe the microstructure configuration. The strain energy method is adopted as an efficient computation approach and effective moduli and CTEs are obtained based on the sequential computation from the fiber scale to the tow scale. The comparison with the experimental results shows the validity of the present model and method.

## **Chapter 4: Stress analysis of C/SiC composite structures using global/local approach**

### **4.1 Introduction**

Accurate detailed stress analysis is the basis of understanding the failure mechanisms and designing the component parts for the practical structures. With rapidly growing computational modelling capability, the finite element method becomes a common tool for an accurate detailed stress analysis. However, the application of composite materials in engineering structures introduces important complexity to the stress analysis. Owing to the complex fiber-tow geometry of composites, a reasonably discrete finite element model often requires a large number of three-dimensional elements even for a small portion of the composite structures. Motivated by this situation, the global/local methods [88] that allow contextual and multi-scale analysis of complex structures in an efficient and accurate manner are applied in the detailed stress analysis of composite structures.

Generally speaking, global/local stress analysis methodology is a procedure that allows the determination of local detailed stress states for specific regions of a structure using information obtained from an independent global stress analysis. The development of such a procedure has been underway for several decades. Many researchers implemented effectively the detailed stress analysis procedure of complex composite structures, such as woven composite laminates using the global/local method [88-94]. In fact, the stress analysis is carried out at two stages: a global analysis and a local analysis. A global analysis accounts for the macroscopic heterogeneity on the basis of the homogenized model and a relatively coarse mesh is used. To obtain detailed stress distributions in the microstructure, a local analysis is further performed at the level of the representative volume cell (RVC) by using information obtained from the global stress analysis.

Due to the multi-layer architecture of geometrical configuration and the large heterogeneity of multi-phase materials, the detailed stress analysis of structures built of C/SiC composites

with multi-layer interfaces or matrices are significantly more complex than those of other traditional composites. Owing to the fact that C/SiC composites have just been developed in recent years, the numerical characterization study is limited and systematical methods of the stress analysis of C/SiC composite structures are not discussed. In this chapter, the global/local analysis strategy is employed to determine local stresses in the 2-D woven C/SiC laminate structures. On the basis of the finite element analysis, the procedure is carried out sequentially from the homogenized composite structure of the macro-scale to the parameterized detailed fiber tow model of the micro-scale. The bridge between two scales is realized by mapping the global analysis result as the boundary conditions of the local tow model and hence the influence of the global model refinement on the computing accuracy of local stress is particularly addressed. To verify the computing results of such a global/local analysis, we use a refined finite element mesh of the laminate structure whose solution is considered as the standard of comparison.

## **4.2 Basis of global/local stress analysis**

The global/local stress analysis method is used to determine local detailed stress states by using the independent, refined local model which exploits results from the coarse global model. Here, the local model refers to a sub-region of the global model and the global model refers to the whole structure. Figure 4.1 explains the global/local model of a composite structure. In this sketch the shading identifies the element which will be analyzed further by using a local model. The local refined model for the detailed stress analysis is shown to be isolated from the rest of the global model. The methodology for a global/local analysis generally involves four key components which are discussed below. The development of a global/local stress analysis methodology requires an understanding of each key component and insight into their interaction.

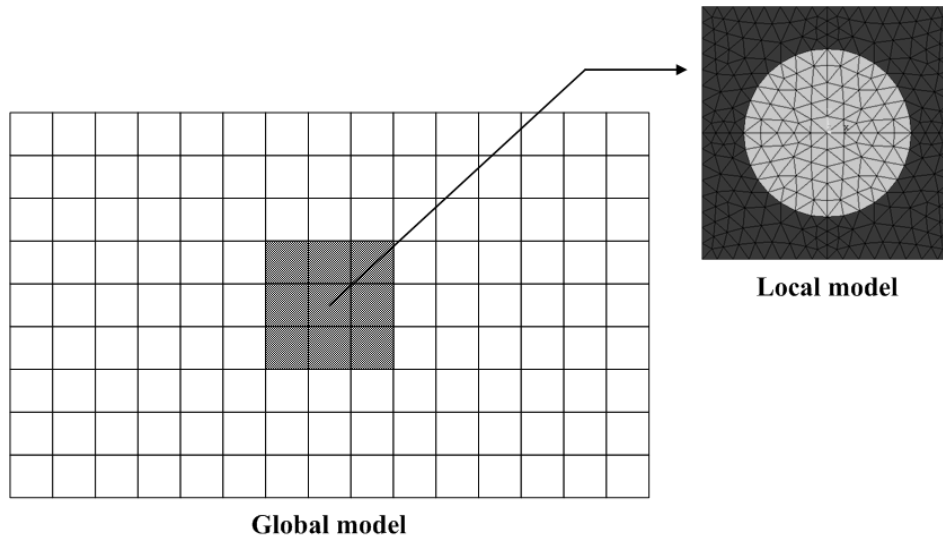


Figure 4.1 Global/local model of a composite structure

### 4.2.1 Global analysis

The first component is the global analysis. A finite element analysis of the global structure is performed to obtain its overall behavior and the global solutions will be used to obtain an applied displacement field along the boundary (i.e., boundary conditions) of an independent local model of the critical region. In a global analysis, the whole structure is discretized by using a coarse mesh. However, the coarse finite element modelling should be efficient to represent the global structural behavior.

### 4.2.2 Global/local interface boundary definition

The second component is an identification of regions requiring further study in the global model. In the definition of the global/local interface boundary, the location of the nodes of the local model on the interface boundary need not be coincident with any of the nodes in the global model. It is concluded [89] that the distance that the local model must extend away from a discontinuity is highly dependent upon the used global model. If the displacement field of the global model is more accurate then the boundary of the local model may be closer to discontinuity.



### 4.2.3 Global/local interpolation

The third component is an interpolation procedure that does not require that the nodes of the local model along the global/local interface boundary be coincident with the nodes of the global model. The global displacement field is interpolated to produce a local displacement field applied as boundary conditions on the local model. The interpolation problem can be stated as follows: given a set of function values  $F_i$  at  $n$  coordinates  $(x_i, y_i)$ , determine a "best-fit" surface for these data. Mathematically, this problem can be stated as

$$\left[ S(x_i, y_i) \right] \begin{Bmatrix} a_1 \\ a_2 \\ \vdots \\ a_n \end{Bmatrix} = \begin{Bmatrix} F_1 \\ F_2 \\ \vdots \\ F_n \end{Bmatrix} \quad (4.1)$$

where  $S(x_i, y_i)$  is a matrix of interpolation functions evaluated at  $n$  points, the vector  $\mathbf{a}$  defines the unknown coefficients of the interpolation functions, and the vector  $\mathbf{F}$  consists of known values of the field being interpolated based on  $n$  points in the global model. Common interpolation methods include bilinear interpolation, nearest-neighbor interpolation, bicubic interpolation and bicubic spline interpolation.

### 4.2.4 Local analysis

Finally, the fourth component is the local analysis. The local finite element modelling and analysis is performed to obtain a detailed analysis of the local structural region(s). The local model should accurately represent the geometry of the structure necessary to provide the local behavior and local stress state. The discretization requirement for the analysis is governed by the accuracy of the solution desired.

## 4.3 Global/local stress analysis strategy for 2-D woven C/SiC laminate panel structure

In the global/local stress analysis of 2-D woven C/SiC laminate panel structure, the global model concerns the homogenized laminate panel structure and the local model is defined by

the tow-scale RVC model of 2-D C/SiC composite. The global/local stress analysis procedure of 2-D woven C/SiC laminate panel structure is illustrated in Figure 4.2.

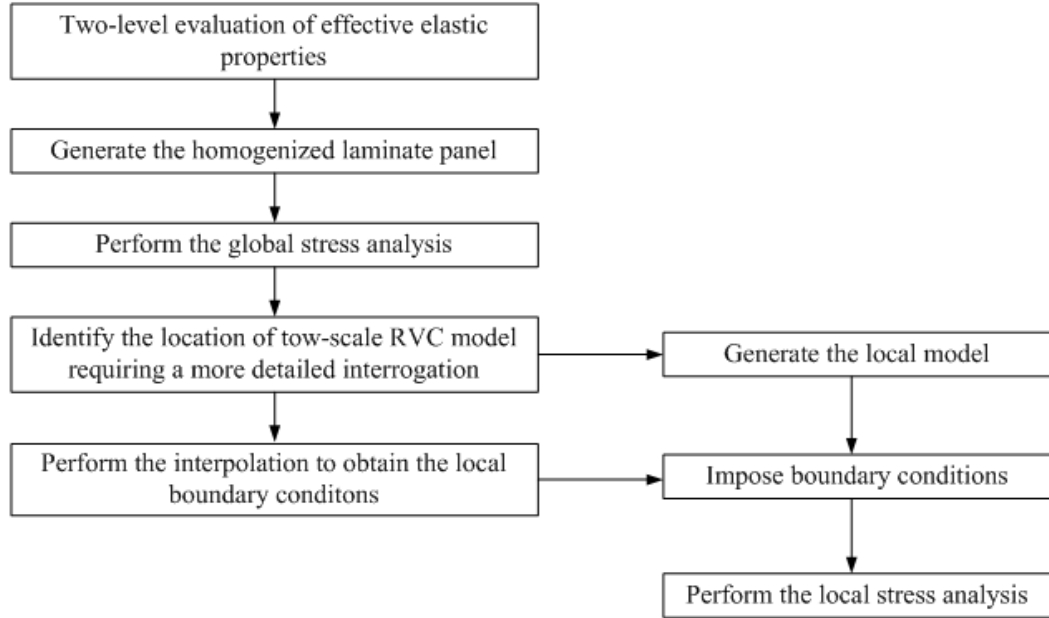


Figure 4.2 Global/local stress analysis procedure of 2-D woven C/SiC laminate panel structure

The effective elastic properties of composite are firstly calculated by using the two-level evaluation strategy which has been discussed in **Chapter. 3**. Homogenized material properties which macroscopically account for the heterogeneity in the composite are then used for the global analysis. The laminate panel is thus regarded as a homogenized structure and meshed with eight-node solid element SOLID45 of ANSYS software, as shown in Figure 4.3.

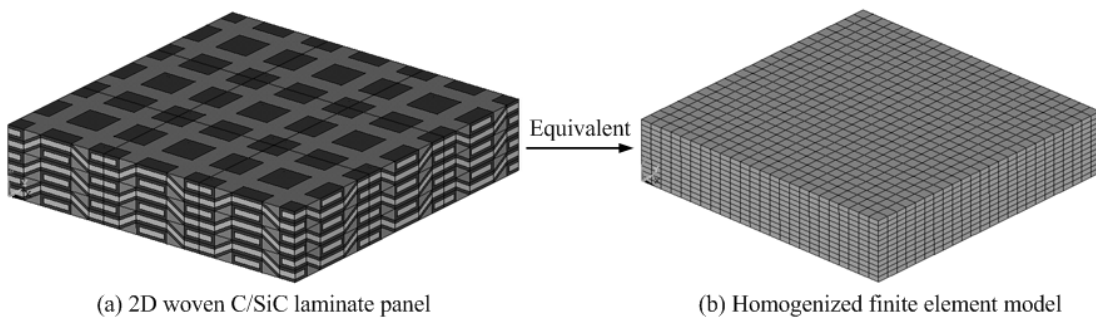


Figure 4.3 Homogenized finite element model of the laminate panel

The local stress analysis involves the generation of the finite element model of RVC on the

tow scale, the interpolation of boundary conditions of the local model and the finite element analysis of the local model. After the global stress analysis, the RVC model on the tow scale requiring a more detailed analysis is subsequently created, as shown in Figure 4.4. An interpolation region is then identified around the RVC model and an interpolation procedure is used to determine the boundary conditions for the RVC model. A surface to surface correspondence of global/local interface is illustrated in Figure 4.4.

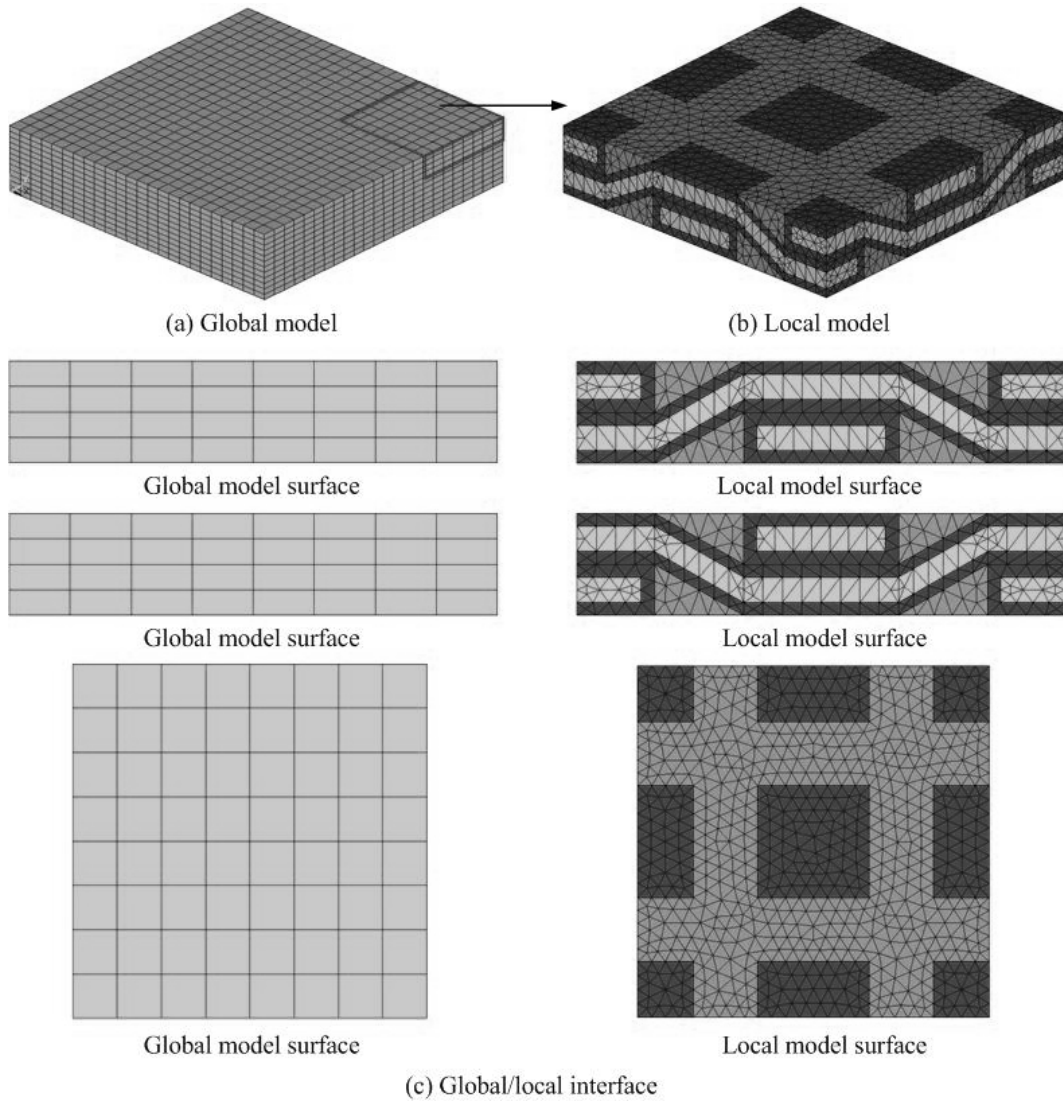


Figure 4.4 Local model and global/local interface

The displacement of each node on the global model surface is obtained after global analysis. The aim is now to construct an interpolation passing exactly through these nodes and thereby provide a functional description of the displacement field over the domain. Here, the bilinear

interpolation is used to interpolate the displacements from the global analysis. The bilinear interpolation is an extension of linear interpolation in two directions. Compared with other methods, the bilinear interpolation is quite simple in numerical implementation.

Consider the rectangular region illustrated in Figure 4.5, suppose the function value  $f$  at point  $P = (x, y)$  is the unknown to be evaluated while values of  $f$  are known at the four corners  $Q_{11} = (x_1, y_1)$ ,  $Q_{21} = (x_2, y_1)$ ,  $Q_{22} = (x_2, y_2)$  and  $Q_{12} = (x_1, y_2)$ .

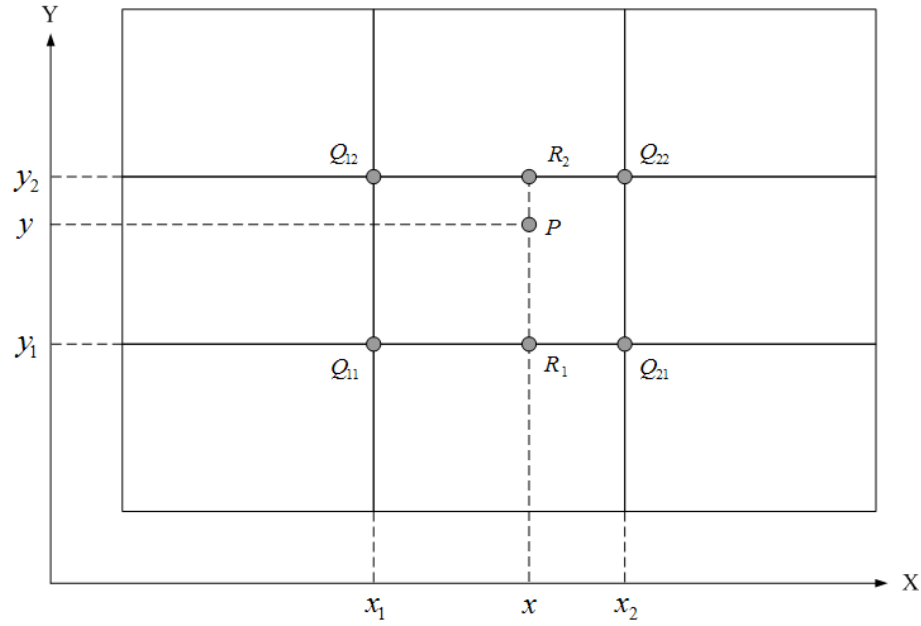


Figure 4.5 Illustration of bilinear interpolation

Linear interpolation along the x-direction then yields

$$f(R_1) \approx \frac{x_2 - x}{x_2 - x_1} f(Q_{11}) + \frac{x - x_1}{x_2 - x_1} f(Q_{21}) \quad (4.2)$$

$$f(R_2) \approx \frac{x_2 - x}{x_2 - x_1} f(Q_{12}) + \frac{x - x_1}{x_2 - x_1} f(Q_{22}) \quad (4.3)$$

where  $R_1 = (x, y_1)$  and  $R_2 = (x, y_2)$ .

Hence, linear interpolation between  $f(R_1)$  and  $f(R_2)$  in the y-direction yields

$$f(P) \approx \frac{y_2 - y}{y_2 - y_1} f(R_1) + \frac{y - y_1}{y_2 - y_1} f(R_2) \quad (4.4)$$

In detail, the following expression of  $f(x, y)$  holds

$$\begin{aligned} f(x, y) \approx & \frac{f(Q_{11})}{(x_2 - x_1)(y_2 - y_1)}(x_2 - x)(y_2 - y) \\ & + \frac{f(Q_{21})}{(x_2 - x_1)(y_2 - y_1)}(x - x_1)(y_2 - y) \\ & + \frac{f(Q_{12})}{(x_2 - x_1)(y_2 - y_1)}(x_2 - x)(y - y_1) \\ & + \frac{f(Q_{22})}{(x_2 - x_1)(y_2 - y_1)}(x - x_1)(y - y_1) \end{aligned} \quad (4.5)$$

In the present study, one such interpolation procedure is used to obtain the displacements on the global/local interface boundary, which is then applied as "boundary conditions" to get the detailed stresses on the tow scale in the complete finite element analysis of the local model.

## 4.4 Numerical tests

### 4.4.1 Problem description

As shown in Figure 4.6, a 2-D woven C/SiC laminate panel is considered. There are three layers of plies along the thickness direction and each layer consists of an array of 3×3 RVC models on the tow scale. The global model and local model are depicted in Figure 4.6c and Figure 4.6d, respectively.

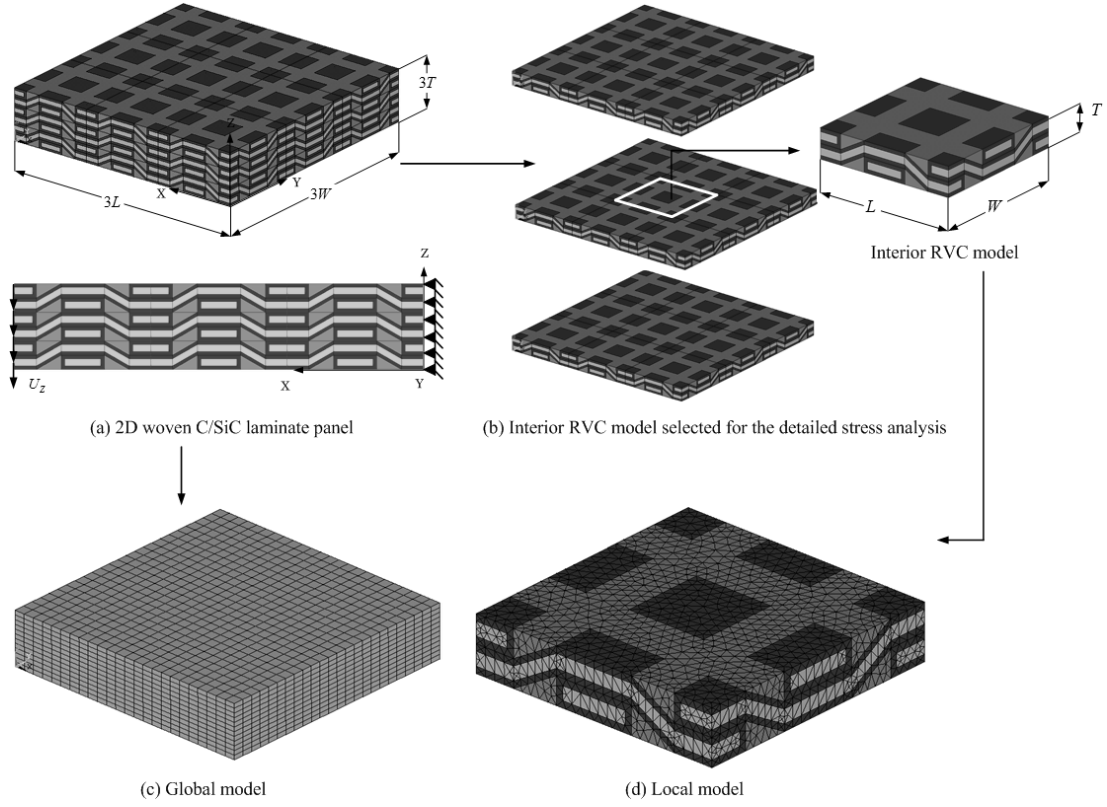


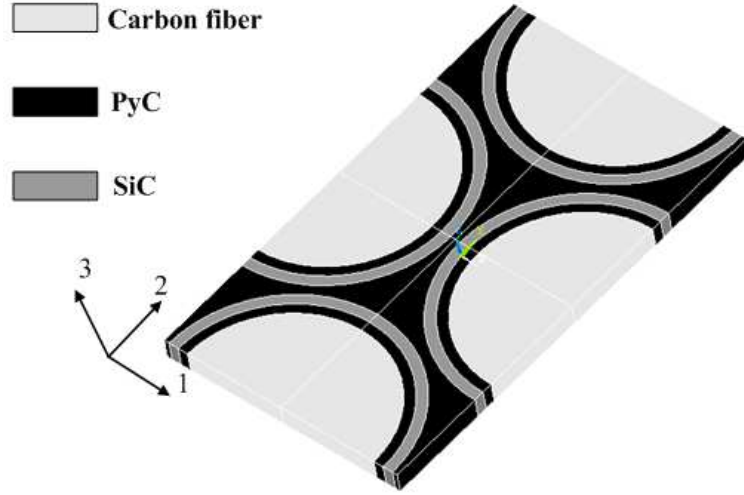
Figure 4.6 Global and local models of 2-D woven C/SiC laminate panel

The boundary conditions for the load case are as follows

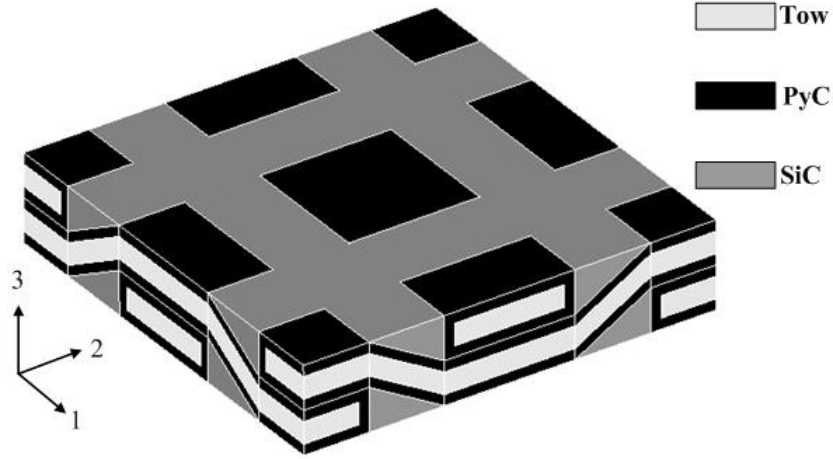
$$\begin{aligned}
 u(0, y, z) = v(0, y, z) = w(0, y, z) = 0 \\
 w(3L, y, z) = -0.3T
 \end{aligned}
 \tag{4.6}$$

where  $u$ ,  $v$  and  $w$  refer to the displacement along  $x$ ,  $y$  and  $z$  directions, respectively.  $T$  is the thickness of the ply as shown in Figure 4.6a.

The fiber-scale RVC model of the 2-D woven C/SiC composite, depicted in Figure 4.7a, consists of one layer of PyC interface and two layers of matrices made up of alternate SiC and PyC. On the tow scale, the RVC model depicted in Figure 4.7b consists of two layers of matrices made up of PyC and SiC.



(a) RVC model on the fiber scale



(a) RVC model on the tow scale

Figure 4.7 RVC models of the 2-D woven C/SiC composite

Engineering moduli data for each material phase are listed in Table 4.1 with the units of the moduli being all in GPa. Geometric parameters of RVC models on the two scales are assumed below.

***RVC model on the fiber scale***

$$\phi^f = 10\mu m, \quad d_1^i = 0.5\mu m, \quad d_1^m = 0.5\mu m, \quad d_2^m = 0.5\mu m$$

***RVC model on the tow scale***

$$a_f = a_w = 20mm, \quad h_f = h_w = 4mm, \quad \theta = 30^\circ, \quad t_1^m = 2.0mm$$

Table 4.1 Engineering modulus data for each material phase

	E <sub>11</sub>	E <sub>22</sub>	E <sub>33</sub>	G <sub>12</sub>	G <sub>23</sub>	G <sub>13</sub>	v <sub>12</sub>	v <sub>23</sub>	v <sub>13</sub>
Carbon fiber	22	22	220	7.75	4.8	4.8	0.42	0.12	0.12
PyC	12	12	30	4.3	2.0	2.0	0.4	0.12	0.12
SiC	350	-	-	145.8			0.2	-	-

#### 4.4.2 Evaluation of the elastic properties of the composite

Finite element models of fiber-scale and tow-scale RVC are established respectively and effective elastic properties of composite are obtained based on the sequential evaluation from the fiber-scale to the tow-scale.

The effective Hooke matrix of tow evaluated on the fiber scale is given below

$$[D]_{Tow} = \begin{bmatrix} 41.2425 & & & & & & & & \\ & 22.6036 & 41.2425 & & & & & & \\ & 40.9868 & 40.9868 & 257.8391 & & & & & \\ & 0 & 0 & 0 & 9.2668 & & & & \\ & 0 & 0 & 0 & 0 & 10.1662 & & & \\ & 0 & 0 & 0 & 0 & 0 & 10.1662 & & \end{bmatrix} \text{ GPa}$$

The effective elastic moduli of tow are listed in Table 4.2 and the units are all in GPa.

Table 4.2 Effective elastic moduli of tow

E <sub>11</sub>	E <sub>22</sub>	E <sub>33</sub>	G <sub>12</sub>	G <sub>23</sub>	G <sub>13</sub>	v <sub>12</sub>	v <sub>23</sub>	v <sub>13</sub>
27.27	27.27	205.22	9.27	10.17	10.17	0.46	0.085	0.085

The effective Hooke matrix of composite evaluated on the tow scale is evaluated as

$$[D]_{Composite} = \begin{bmatrix} 122.3959 & & & & & & & & \\ & 21.6225 & 122.3959 & & & & & & \\ & 23.5111 & 23.5111 & 84.6481 & & & & & \\ & 0 & 0 & 0 & 12.7512 & & & & \\ & 0 & 0 & 0 & 0 & 18.1985 & & & \\ & 0 & 0 & 0 & 0 & 0 & 18.1985 & & \end{bmatrix} \text{ GPa}$$

The effective elastic moduli of composite are listed in Table 4.3 and the units are all in GPa.



Table 4.3 Effective elastic moduli of composite

$E_{11}$	$E_{22}$	$E_{33}$	$G_{12}$	$G_{23}$	$G_{13}$	$\nu_{12}$	$\nu_{23}$	$\nu_{13}$
113.89	113.89	76.97	12.75	18.20	18.20	0.13	0.24	0.24

#### 4.4.3 Stress analysis results

In this study, the interior RVC model shown in Figure 4.6b is selected as the local region for the detailed stress analysis. The tows and multi-layer matrices of the local model as shown in Figure 4.6d are meshed with 35657 ten-node tetrahedral elements. The global model is depicted in Figure 4.6c. Generally, an "adequate" global analysis is required to provide accurate "boundary conditions" for the local model. In the present study, a parameter  $RATIO_{GL}$ , the ratio of the total number of global model surface nodes to local model surface nodes on the global/local interface is defined to characterize the global model refinement. To have a clear insight of the influence of the global model refinement on the solution accuracy, we start with a "coarse" mesh of 6912 eight-node brick elements for the discretization of global model and then systematically refine the global grid. The total number of elements and the value of  $RATIO_{GL}$  for each global grid are given in Table 4.4.

Table 4.4 Number of elements and value of  $RATIO_{GL}$  for each global grid

Global grid	1	2	3	4	5	6	7
Elements	6912	8748	13500	16335	23328	27378	37044
$RATIO_{GL}$	0.080	0.095	0.125	0.144	0.179	0.202	0.244

For a comparative study, stress distributions are determined using the proposed global/local analysis method and the direct finite element discretization, respectively. As the latter is based on a refined finite element model which accurately models the tows and multi-layered matrices without homogenization as illustrated in Figure 4.8, the corresponding result can be regarded as a reference.

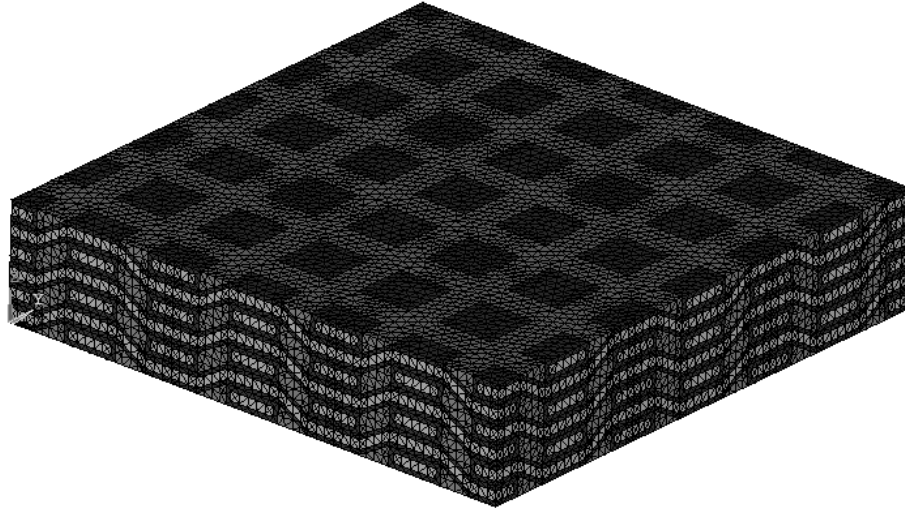


Figure 4.8 Reference finite element model of the 2-D woven C/SiC laminate panel

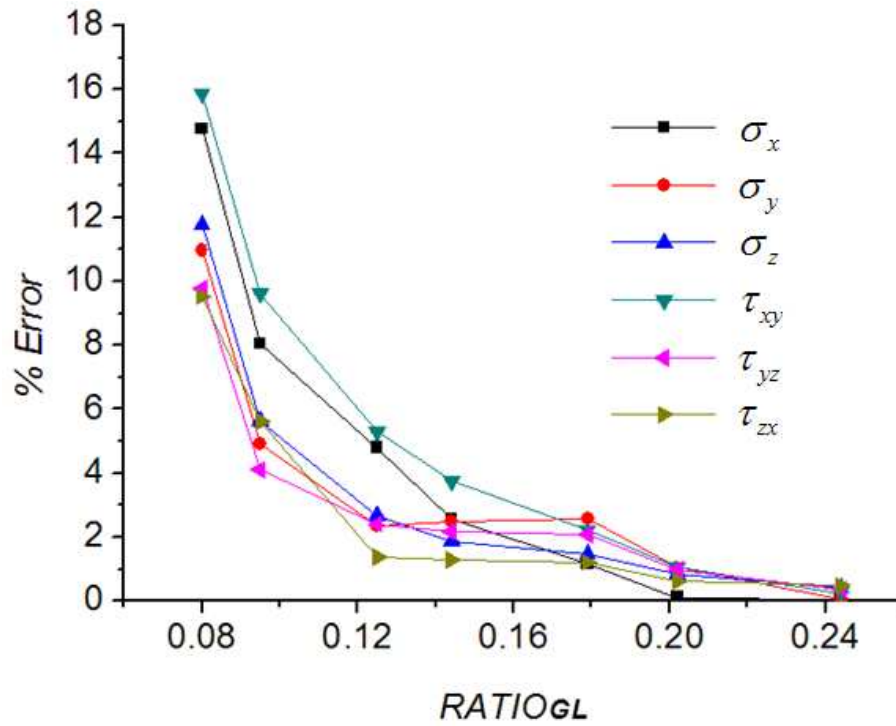


Figure 4.9 Convergence of the maximum stresses within the tows

The convergence of the maximum stresses within the tows of the RVC model is shown in Figure 4.9 along with the refinement of the global model. Clearly, the error decreases rapidly with the increase of  $RATIO_{GL}$ . As the value of  $RATIO_{GL}$  exceeds 0.2, the global/local solution shows a good agreement with the reference solution.

Furthermore, a comparison of the CPU computational cost between the global/local analysis and the conventional finite element analysis is given in Table 4.5. Note that each analysis is executed on a Core™2 Duo, 2.93 GHz machine. It can be seen that the global/local method improves greatly the efficiency of the detailed stress analysis of the 2-D woven C/SiC laminate panel. It takes only 38% of the CPU time required for the conventional finite element analysis.

Table 4.5 Comparison of the CPU time (seconds)

	1	2	3	4	5	6	7
Global analysis	40.4	60.6	135.2	183.3	382.4	457.9	801.8
Local analysis	146.8	146.8	146.8	146.8	146.8	146.8	146.8
Total	187.2	207.4	282.0	330.1	529.2	604.7	948.6
Conventional FE analysis	2483.6						

For the RVC model, peak stresses are listed in Table 4.6 for the tows, the first layer and second layer of matrix using different grid refinements. It can be seen that the agreement between global/local solution and the reference solution is satisfactory and that the more accurate peak stresses are obtained when the global model is refined.

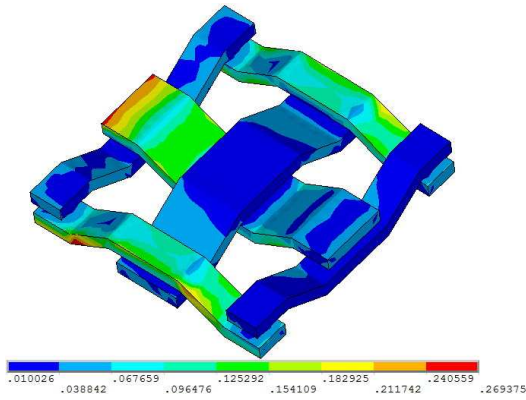
Table 4.6 Peak stresses of global/local solution and reference solution

Mesh		$\sigma_x$	$\sigma_y$	$\sigma_z$	$\tau_{xy}$	$\tau_{yz}$	$\tau_{zx}$
Global grid 3	Peak stresses within the tows (MPa)						
13500 elements	Global/local solution	-331.03	-44.094	-102.977	-49.633	36.14	-140.455
<b>RATIO<sub>GL</sub></b> =0.125	Reference solution	-315.861	-43.082	-105.795	-52.413	37.032	-138.544
	Error (%)	4.80	2.35	2.66	5.30	2.41	1.38
	Peak stresses within the first layer of matrix (MPa)						
	Global/local solution	109.878	-57.785	-40.186	-25.839	-11.765	-46.097
	Reference solution	118.657	-61.068	-42.324	-24.928	-11.444	-44.612
	Error (%)	7.40	5.38	5.05	3.65	2.80	3.33
	Peak stresses within the second layer of matrix (MPa)						
	Global/local solution	1229.0	-658.957	1092.0	413.732	326.217	-682.328
	Reference solution	1363.0	-696.401	1022.0	436.838	331.853	-633.244

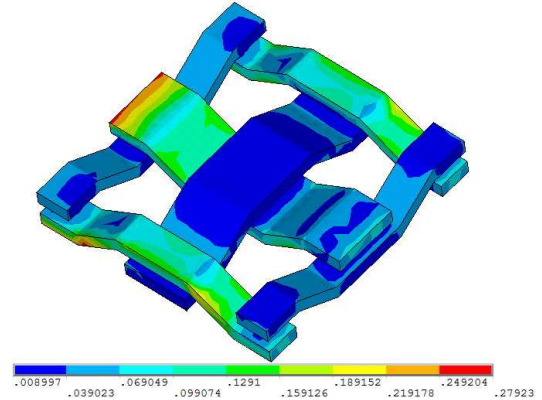
Error (%)		9.83	5.38	6.85	5.29	1.70	7.75
		Peak stresses within the tows (MPa)					
Global grid 5	Global/local solution	-319.479	-44.186	-107.364	-51.247	36.267	-140.229
	Reference solution	-315.861	-43.082	-105.795	-52.413	37.032	-138.544
	Error (%)	1.15	2.56	1.48	2.22	2.07	1.22
	Peak stresses within the first layer of matrix (MPa)						
23328 elements	Global/local solution	118.79	-60.298	-41.992	-25.039	-11.263	-44.836
<b>RATIO<sub>GL</sub></b> =0.179	Reference solution	118.657	-61.068	-42.324	-24.928	-11.444	-44.612
	Error (%)	0.11	1.26	0.78	0.45	1.58	0.50
		Peak stresses within the second layer of matrix (MPa)					
	Global/local solution	1361.0	-687.608	1004.0	423.682	326.217	-623.563
	Reference solution	1363.0	-696.401	1022.0	436.838	331.853	-633.244
	Error (%)	0.15	1.26	1.76	3.01	1.70	1.53
		Peak stresses within the tows (MPa)					
	Global/local solution	-315.732	-43.061	-106.234	-52.537	37.172	-139.209
	Reference solution	-315.861	-43.082	-105.795	-52.413	37.032	-138.544
	Error (%)	0.04	0.05	0.41	0.24	0.38	0.48
		Peak stresses within the first layer of matrix (MPa)					
Global grid 7	Global/local solution	118.498	-61.285	-42.447	-24.890	-11.475	-44.539
37044 elements	Reference solution	118.657	-61.068	-42.324	-24.928	-11.444	-44.612
<b>RATIO<sub>GL</sub></b> =0.244	Error (%)	0.13	0.36	0.29	0.15	0.27	0.16
		Peak stresses within the second layer of matrix (MPa)					
	Global/local solution	1361.0	-696.997	1023.0	438.544	334.747	-632.331
	Reference solution	1363.0	-696.401	1022.0	436.838	331.853	-633.244
	Error (%)	0.15	0.09	0.10	0.39	0.87	0.14

The examination of peak stresses gives only a limited view of the prediction accuracy. Figures 4.10-4.12 show further von Mises stress (the units are all in GPa) distributions evaluated by the global/local analysis based on global grid 3, 5, 7 and the direct finite element analysis over the tows, the first and second layer of matrix, respectively. Although the stress contours of global/local solution based on the global grid 3 are not as close as the reference solution, they seem to agree fairly well. As the global model refinement is “adequate” (global grid 5 and 7), the stress contours between the global/local analysis and the reference solution

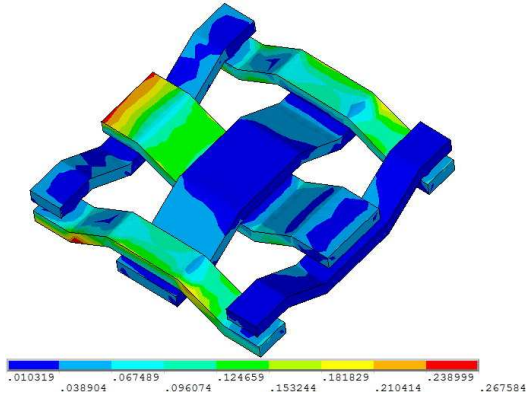
match very closely.



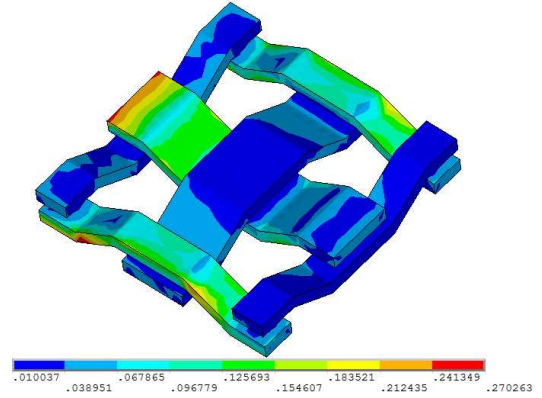
(a) Reference solution



(b) Global/local solution based on global grid 3

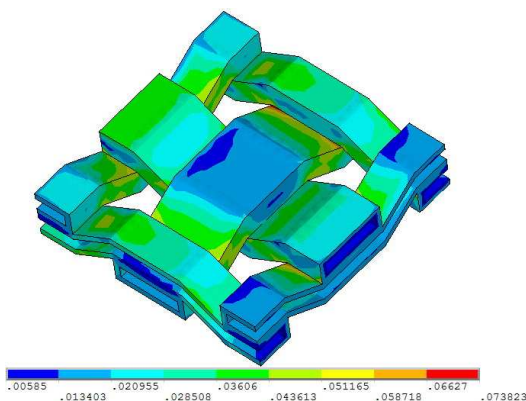


(c) Global/local solution based on global grid 5

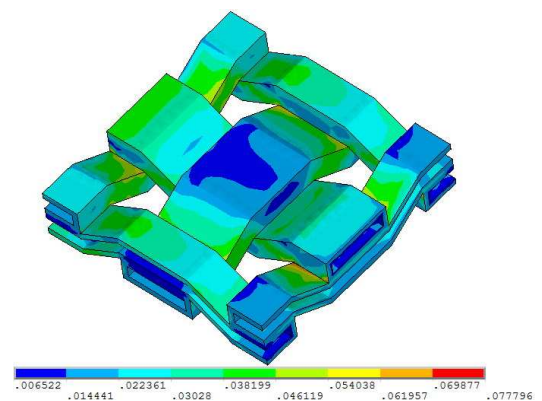


(d) Global/local solution based on global grid 7

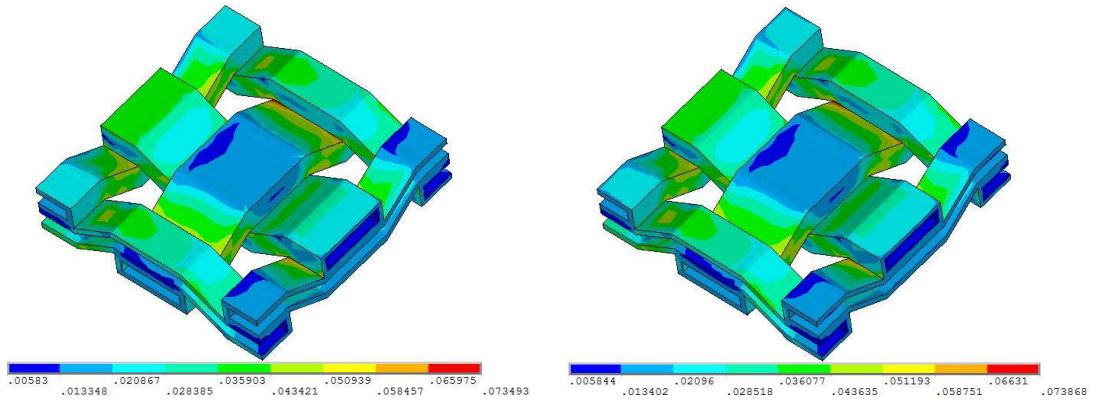
Figure 4.10 von Mises stress distributions over the tows



(a) Reference solution

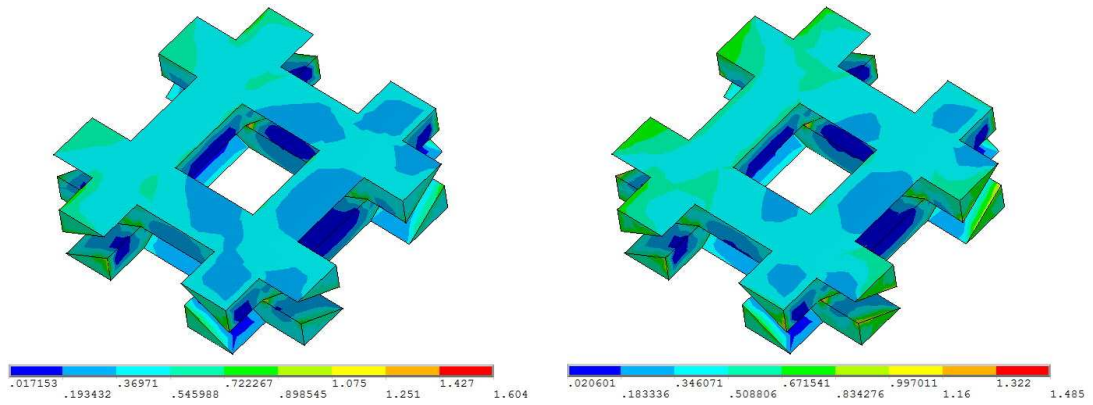


(b) Global/local solution based on global grid 3



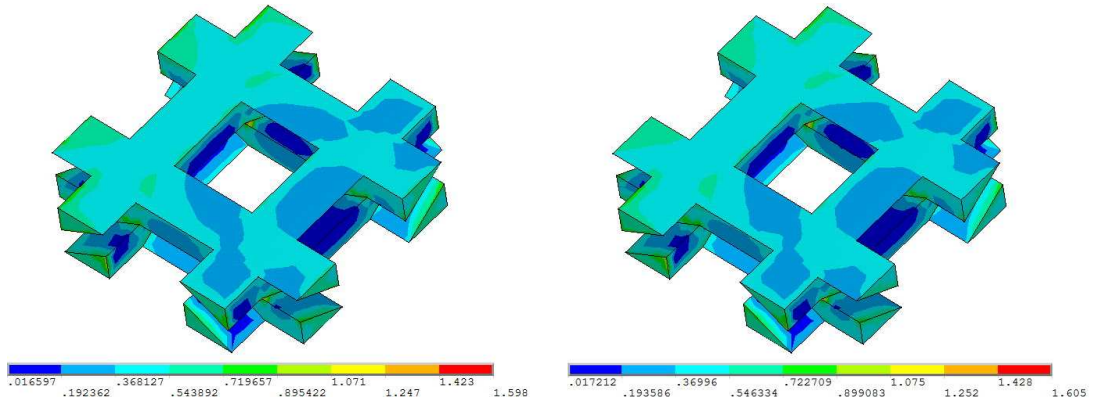
(c) Global/local solution based on global grid 5 (d) Global/local solution based on global grid 7

Figure 4.11 von Mises stress distributions over the first layer of matrix



(a) Reference solution

(b) Global/local solution based on global grid 3



(c) Global/local solution based on global grid 5 (d) Global/local solution based on global grid 7

Figure 4.12 von Mises stress distributions over the second layer of matrix

## 4.5 Conclusions

The global/local method is applied for the detailed stress analysis of 2-D woven C/SiC

laminate structures. A stress analysis problem of 2-D woven C/SiC laminate panel is discussed in this chapter. The stress results by global/local method are compared to those by conventional finite element analysis. Results indicate that the global/local method could be an efficient tool for the detailed stress analysis of C/SiC composite structures and the adequate refined global grid is required for accurate stress results.

# **Chapter 5: Minimizing thermal residual stresses of C/SiC composites by using particle swarm optimization algorithm**

## **5.1 Introduction**

In C/SiC composites with multi-layer interfaces and matrices, thermal residual stresses (TRS) are often generated upon cooling from processing to room temperatures due to extensive mismatch of the coefficients of thermal expansion (CTE) between the constituents (fiber, multi-layer interfaces and matrices). The distribution of TRS, resulting in the cracks and separations in the matrix and interfaces, has a significant influence on the mechanical behavior of C/SiC composites. Experimentally [95-100] or analytically [101-103], many researchers have studied the effect of TRS in C/SiC composites. The multiple concentric cylinder model [101-102] and finite element method [101-103] have been used for numerical computation of TRS in C/SiC composites. However, efforts to optimize the distribution of TRS in the multi-layer interfaces and matrix of C/SiC composites have not been made yet systematically. The multi-layer interfaces and matrices are usually obtained by using the chemical vapor infiltration (CVI) process. During the CVI process, the thicknesses of layers are controllable. To achieve an excellent thermal-mechanical performance of C/SiC composites, it is necessary to analyze and design the thicknesses of the multi-layer interfaces and matrices for an optimized TRS distribution. Motivated by this situation, the present chapter is directed at minimizing the TRS of C/SiC composites with multi-layer interfaces and matrices by coupling finite element analysis with a particle swarm optimization (PSO) algorithm.

The PSO algorithm belongs to the category of swarm intelligence techniques. In PSO, each solution of the optimization problem is regarded as a ‘particle’ in the search space, which adjusts its position in the search space according to its own flying experience and the flying experience of other particles [104]. The PSO algorithm has only a small number of



parameters which need to be adjusted and is easy to implement. Although the PSO algorithm has been applied to a wide range of engineering problems in the literature [104-113], few applications for composites and especially C/SiC composites are known.

The 1-D unidirectional C/SiC composites with multi-layer alternate PyC/SiC interfaces and single-layer SiC matrix are concerned in this chapter. The primary objective is the optimization of TRS distribution in the multi-layer interfaces and matrix from the point of view of the deposition thickness of each interface layer. Modeling study of the TRS of the 1-D unidirectional C/SiC composites is investigated by finite element method. Comparison with experimental data and other available numerical results have shown the validity of the present model. Then, the optimization is carried out using PSO algorithm. More details about the PSO algorithm are given in the fourth section.

## **5.2 Finite element analysis of TRS**

### **5.2.1 Finite element model**

The fabrication process of the studied 1-D unidirectional C/SiC composites is briefly introduced below. The architectures of the 1-D unidirectional C/SiC composites consist of arranged fibers. The components of the multi-layer alternate PyC/SiC interfaces and SiC matrix are infiltrated within the porous fiber preforms, according to the CVI process.

In the present study, square fiber arrays are used to model the 1-D unidirectional C/SiC composites. Four layers of interfaces and one layer of matrix are distributed around the fibers. Figure 5.1 shows the transverse cross-section of the 1-D unidirectional C/SiC composites. In the longitudinal direction, the fiber axes have been assumed to be parallel and of equal lengths.

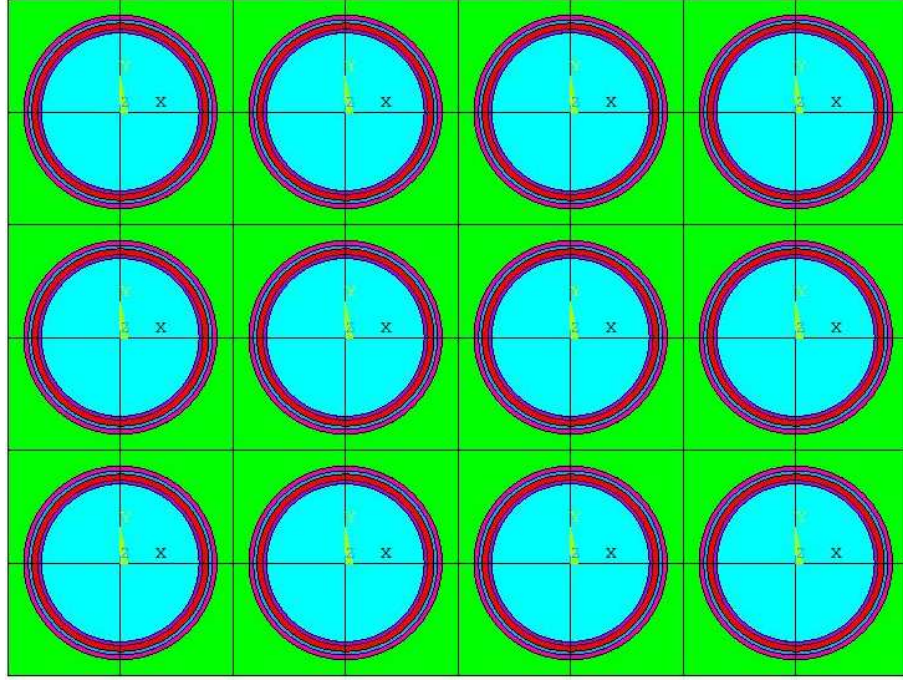
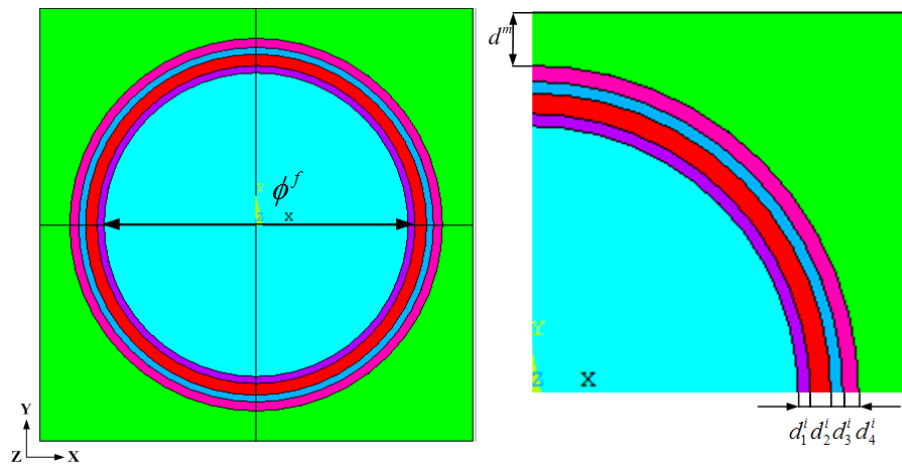
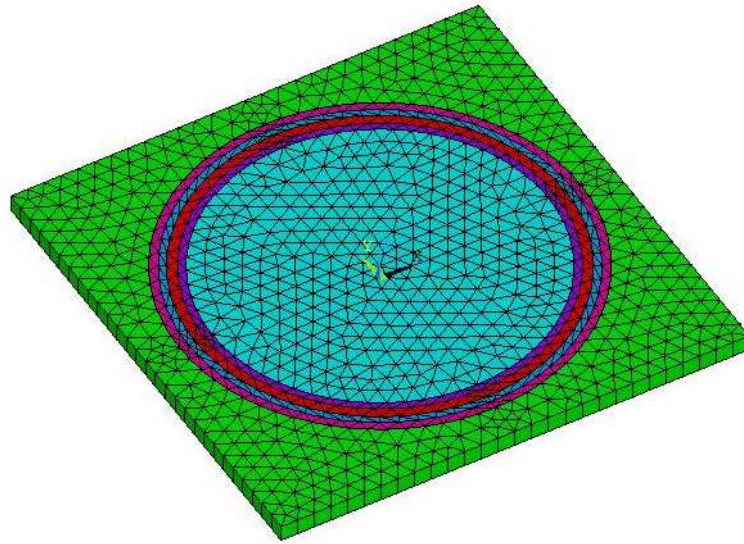


Figure 5.1 Transverse cross-section of the 1-D unidirectional C/SiC composites

The RVC model of composites (as seen in Figure 5.2a) is used in the present finite element analysis. Characteristic geometric parameters of the RVC model are given:  $\phi^f$  is fiber diameter;  $d_1^i \sim d_4^i$  are thicknesses of the interface layers;  $d^m$  is the thickness of the matrix layer. The RVC model is meshed using the 3D twenty-node, thermal-structural coupled element package (SOLID 96) of ANSYS finite element software, as depicted in Figure 5.2b. The number of elements and nodes is 3,840 and 3,986, respectively.



(a) Geometric model



(b) Finite element model

Figure 5.2 RVC model of the 1-D unidirectional C/SiC composites

The analytical model is assumed as a perfect elastic body without plastic deformation. The structural and thermal boundary conditions are given as follows:

- Nodes on the boundary surfaces are free to move but have to remain planar in a parallel way to preserve the compatibility with adjacent RVC models;
- The initial stresses of all nodes are assumed as zero at the sintering temperature, and TRS generated in the succedent cooling process;
- The model is assumed to cool from sintering temperature to room temperature, with a uniform temperature field. In practice, temperature of the model is decreased by  $\Delta T$  and *ANSYS* finite element software is used to calculate the TRS in the model.

### 5.2.2 Numerical tests

Due to the complexity of the CVI fabrication process of multi-layer interfaces and matrix, most of the available experimental results and numerical values evaluated by other numerical methods in the literature are focused on the C/SiC composites with single-layer interface and matrix. Hence, in this section, numerical tests are dealing with to evaluate TRS of C/SiC composites with single-layer interface and matrix. These results are compared with experimental data and other available numerical results to show the validity of the model.

A 1-D unidirectional carbon fiber reinforced SiC ceramic matrix composite with single-layer

MoSi<sub>2</sub> interface (C/MoSi<sub>2</sub>/SiC) is firstly studied. Residual axial and hoop thermal stresses in C/MoSi<sub>2</sub>/SiC composites fabricated with 8  $\mu\text{m}$  T300 carbon fiber have been measured experimentally [101]. Figure 5.3 shows the finite element model of the RVC of C/MoSi<sub>2</sub>/SiC composite with a 1/2.5 interface/matrix thickness ( $\mu\text{m}$ ). Similar finite element models are created for other interface/matrix thicknesses.

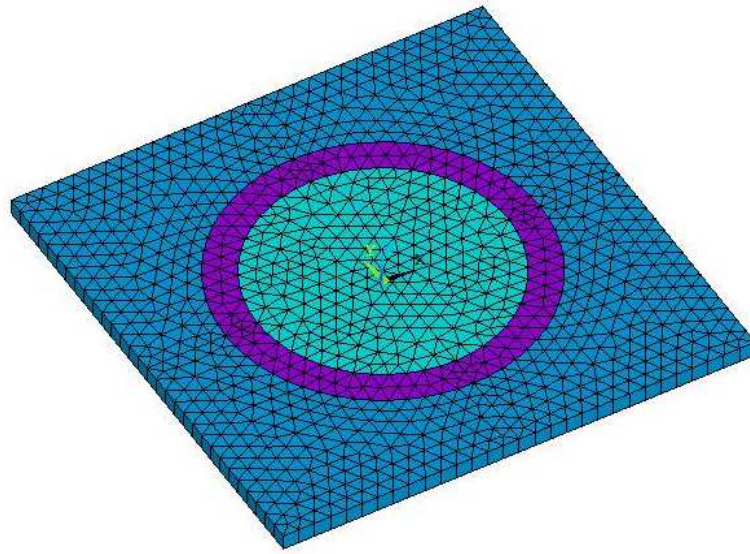


Figure 5.3 Finite element model of the RVC of C/MoSi<sub>2</sub>/SiC composite

Material properties of the constituents are taken from [101] and are given in Table 5.1.

Table 5.1 Properties of the constituents

	E <sub>11</sub> (GPa)	E <sub>33</sub> (GPa)	G <sub>12</sub> (GPa)	G <sub>23</sub> (GPa)	$\nu_{12}$	$\nu_{23}$	$\alpha_{11}$ ( $10^{-6}/^{\circ}\text{C}$ )	$\alpha_{33}$ ( $10^{-6}/^{\circ}\text{C}$ )
Carbon fiber	22	220	7.75	4.8	0.4	0.12	8.85	0
SiC fiber	200	200	80	80	0.12	0.12	3	3
MoSi <sub>2</sub> interface	310	310	124	124	0.25	0.25	8.4	8.4
PyC interface	12	30	4.3	2	0.4	0.12	28	2
SiC matrix	350	350	145.8	145.8	0.2	0.2	4.6	4.6

Two thermal loading states are prescribed. The unit cell is assumed initially at a uniform temperature of 1000°C (state 1). Then in state 2, the temperature is uniformly set to 0°C.

Table 5.2 lists the average values of the numerically obtained TRS against experimental results in [101]. It can be seen that the numerical results are globally in agreement with the

experimental ones.

Table 5.2 Comparison of numerical results with experimental ones

Interface/Matrix thickness ( $\mu m$ )		Axial stresses (MPa)		Hoop stresses (MPa)	
		Interface	Matrix	Interface	Matrix
0.3/2.1	Numerical analysis	1287	158	162	-910
	Experimental results	1190	140	230	-740
1/2.1	Numerical analysis	935	127	146	-903
	Experimental results	820	140	180	-670
0.3/2.5	Numerical analysis	1610	109	1548	232
	Experimental results	1490	120	1420	210
1/2.5	Numerical analysis	1026	87	1603	215
	Experimental results	890	120	1430	190

As the examination of residual axial and hoop thermal stresses of C/MoSi<sub>2</sub>/SiC gives only a limited view of the prediction accuracy, a 1-D unidirectional SiC fiber reinforced SiC ceramic matrix composite with MoSi<sub>2</sub> interface (SiC/MoSi<sub>2</sub>/SiC) studied in [102] is also taken into account. The diameter of SiC fiber is 14  $\mu m$ . The thicknesses of interface and matrix are 0.5  $\mu m$  and 1.6  $\mu m$ , respectively. Material properties of the constituents are given in Table 5.1. The RVC model is assumed to cool from 1000°C to 0°C, with a uniform temperature field. Figure 5.4 shows the residual radial thermal stresses (the units are all in GPa) for the RVC model of SiC/MoSi<sub>2</sub>/SiC. In addition, the present numerical results are compared with numerical values evaluated by cylinder model in [102], as illustrated in Figure 5.5. It can be seen that the predicted profiles coincide well with the numerical results reported in the literature.

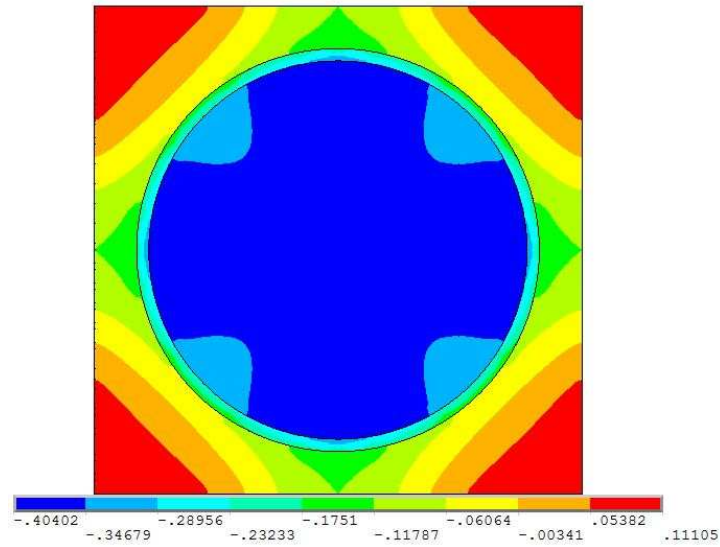


Figure 5.4 Residual radial thermal stresses distribution for RVC model of SiC/MoSi<sub>2</sub>/SiC

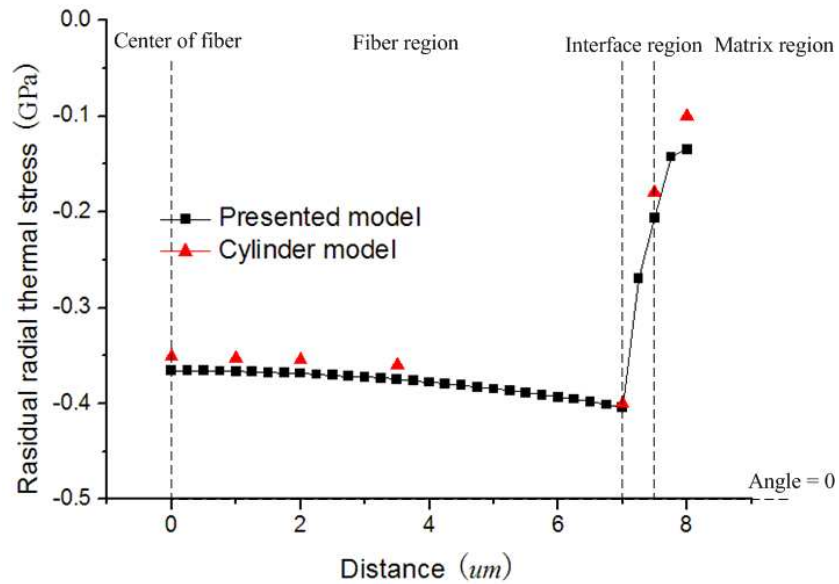


Figure 5.5 Computed residual radial thermal stress and the results of cylinder model

### 5.3 Optimization problem

In this chapter, an interface thicknesses design optimization of 1-D unidirectional C/SiC composites is presented. The primary objective is the optimization of TRS distribution in the multi-layer interfaces and matrix from the point of view of the deposition thickness of each interface layer. The diameter of the carbon fiber is 10  $\mu m$  and the thickness of the SiC

matrix layer is  $2\ \mu\text{m}$ . The upper bound of each interface layer thickness is  $0.6\ \mu\text{m}$ . Usually, the lower bounds of thicknesses of multi-layered interfaces should be bigger than  $0.1\ \mu\text{m}$  for oxidation resistance considerations [114] and reduction of the complexity of the CVI fabrication process. Therefore, in the present study the lower bound for each interface layer thickness is set to  $0.3\ \mu\text{m}$ . Material properties of the constituents are given in Table 5.1.

The optimization problems given in the present study include three cases, which include respectively the minimization of the maximum hoop TRS, radial TRS and axial TRS within the interfaces and matrix.

Mathematically, the above optimization problems can be formulated as

$$\begin{aligned} \text{Minimize } TRS &= f(X) \\ X &= (d_1^i, d_2^i, d_3^i, d_4^i) \\ 0.3 < d_j^i &< 0.6, \quad j=1, 2, 3, 4 \end{aligned} \quad (5.1)$$

where  $f(X)$  is the objective function, i.e., the maximum residual axial, radial or hoop thermal stress within the interfaces and matrix. The variables vector  $X$  represents a set of the design variables, i.e. the thicknesses of the interfaces.

The complicated and nonlinear optimization problem induces difficulty in using classical deterministic approaches for solutions. To solve this nonlinear optimization problem a particle swarm optimization algorithm is used.

## 5.4 Particle swarm optimization algorithm

### 5.4.1 Basis of particle swarm optimization algorithm

PSO is a stochastic optimization method which is based on simulation of social behavior. As in the evolutionary algorithms such as genetic algorithm (GA), PSO exploits a population of potential solutions to probe the search space. In contrast to the evolutionary algorithms in PSO no operators inspired by natural evolution are applied to extract a new generation of candidate solutions. Instead of mutation PSO relies on the exchange of information between individuals, called particles, of the population which is called swarm. In effect, each particle

adjusts its trajectory towards its own previous best position, and towards the best previous position attained by any member of its neighborhood [104]. In the global variant of PSO, the whole swarm is considered as the neighborhood. Thus, global sharing of information takes place and particles profit from the discoveries and previous experience of all other companions during the search for promising regions of the landscape.

Initially, let us define the notation adopted in this study: assuming that the search space is  $M$  dimensional, the  $i$ -th particle of the swarm is represented by a  $M$  dimensional vector  $X_i = (x_{i1}, x_{i2}, \dots, x_{iM})$  and the best particle of the swarm, i.e. the particle with the lowest function value, is denoted by index  $g$ . The best previous position (i.e. the position corresponding to the best function value) of the  $i$ -th particle is recorded and represented as  $P_i = (p_{i1}, p_{i2}, \dots, p_{iM})$ , and the position change (velocity) of the  $i$ -th particle is  $V_i = (v_{i1}, v_{i2}, \dots, v_{iM})$ .

The particles are manipulated according to the following equations (the superscript denotes the iteration number)

$$V_i^{k+1} = \omega V_i^k + c_1 r_1 (P_i^k - X_i^k) + c_2 r_2 (P_g^k - X_i^k) \quad (5.2)$$

$$X_i^{k+1} = X_i^k + V_i^{k+1} \quad (5.3)$$

where  $i = 1, 2, \dots, N$ , and  $N$  is the size of the population;  $r_1$  and  $r_2$  are two uniform random variables generated from the interval between 0 and 1;  $c_1$  and  $c_2$  are the stochastic acceleration constants (explained later in 4.2.2); and  $\omega$  is the inertia weight. Equation (5.2) is used to determine the  $i$ -th particle's new velocity, at each iteration, while Equation (5.3) provides the new position of the  $i$ -th particle, adding its new velocity, to its current position. The performance of each particle is measured according to a fitness function, which is problem dependent and usually identical with the objective function under consideration.

The basic procedure of the PSO algorithm is constructed as follows:

**Step1:** Initialize a set of particles positions and velocities randomly distributed throughout the design space bounded by specified limits.

**Step2:** Evaluate the objective function values using the design space positions.



**Step3:** Update the optimum particle position and global optimum particle position at current iteration.

**Step4:** Update the current velocity vector and modify the position of each particle in the swarm using Equations (5.2) and (5.3).

**Step5:** Repeat from **Step 2** until the stop criterion is achieved. For the current implementation the stopping criteria is defined based on the number of iterations reached.

## 5.4.2 Parameter selection

There are several guidelines about the selection of the key parameters in PSO available in the literature.

### 5.4.2.1 The number of particles

The typical range for the number of particles is 20-40. For most of the problems, 10 particles are large enough to get good results. For some difficult or special problems, 100-200 particles can be tried as well. In this work, a swarm size of 20 particles is chosen.

### 5.4.2.2 The acceleration constants

The acceleration constants  $c_1$  and  $c_2$  indicate the stochastic acceleration terms which pull each particle towards the best position attained by the particle or the best position attained by the swarm. Low values of  $c_1$  and  $c_2$  allow the particles to wander far away from the optimum regions before being tugged back, while the high values pull the particles toward the optimum or make the particles to pass through the optimum abruptly. In this work,  $c_1 = 2$  and  $c_2 = 2$  are chosen.

### 5.4.2.3 The inertia weight

The role of the inertia weight  $\omega$  is important for the convergence behavior of PSO. The inertia weight is employed to control the impact of the previous history of velocities on the current velocity. Thus, the parameter  $\omega$  regulates the trade off between the global (wide ranging) and the local (nearby) exploration abilities of the swarm. A large inertia weight

facilitates exploration (searching new areas), while a small one tends to facilitate exploitation, i.e. fine tuning the current search area. A proper value for the inertia weight  $\omega$  provides balance between the global and local exploration ability of the swarm, and thus results in better solutions. Experimental results imply that it is preferable to initially set the inertia to a large value, to promote global exploration of the search space, and gradually decrease it in order to obtain refined solutions [104]. Thus, a dynamic variation of inertia weight proposed in [105] is used in this paper.  $\omega$  is decreased dynamically based on a fraction multiplier  $k_\omega$  as shown in Equation (5.4)

$$\omega_{k+1} = k_\omega \omega_k \quad (5.4)$$

#### 5.4.2.4 The termination condition

The stop criterion can be adopted as the number of iterations the PSO algorithm execute and the minimum error requirement. In this work, after about 100 iterations the improvement in the objective function is not significant and this value is taken as the maximum number of iterations that the algorithm can execute.

### 5.4.3 Variable limits handling strategy

Most structural optimization problems include the problem-specific constraints and the variable limits. According to Equation (5.1), it can be known that the presented optimization of TRS distribution belongs to quasi unconstrained problems. Hence, only the variable limits, i.e. the design bounds of the interfaces thicknesses, are needed to be effectively handled to make sure that all of the particles fly inside the variable boundaries. A method introduced by Li and Huang [112] which was derived from the harmony search (HS) algorithm [115] dealing with the particles that fly outside the variables boundary is used in the present study. HS algorithm is based on natural musical performance process that occur when a musicians searcher for a better state of harmony, such as during jazz improvisation [115]. The engineers seek for a global solution as determined by an objective function, just like the musicians seek to find musically pleasing harmony as determined by an aesthetic [116]. The HS algorithm includes a number of optimization operators, such as the harmony memory size, the harmony

memory rate, and the pitch adjusting rate. In the study of Li and Huang [112], the harmony memory concept has been used in the PSO algorithm to avoid convergence into local solutions.

In the HS algorithm, the harmony memory stores the feasible vectors, which are all in the feasible space. The harmony memory size determines how many vectors can be stored. A new vector is generated by selecting the components of different vectors randomly in the harmony memory. Undoubtedly, the new vector does not violate the variables boundaries. When it is generated, the harmony memory will be updated by accepting this new vector if it gets a better solution and deleting the worst vector.

Similarly, the PSO stores the feasible and “good” vectors (particles) in the *pbest* swarm, as does the harmony memory in the HS algorithm. Hence, the vector (particle) violating the variables boundaries can be generated randomly again by such a selection technique for the components of different vectors in the *pbest* swarm. There are two different ways to apply this technique to the PSO when any one of the components of the vector violates its corresponding variables boundary. In the first method all the components of this vector should be replaced by selecting the corresponding components of the particle from *pbest* swarm randomly. In the second method only the violated component of the vector should be generated again by such a technique. In the experiments of Li and Huang [112], the results show that the first method makes the particles moving to the local solution easily, and in the second method the particles can reach the global solution in relatively less number of iterations.

To highlight the presentation, a schematic diagram is given in Figure 5.6 to illustrate this strategy.

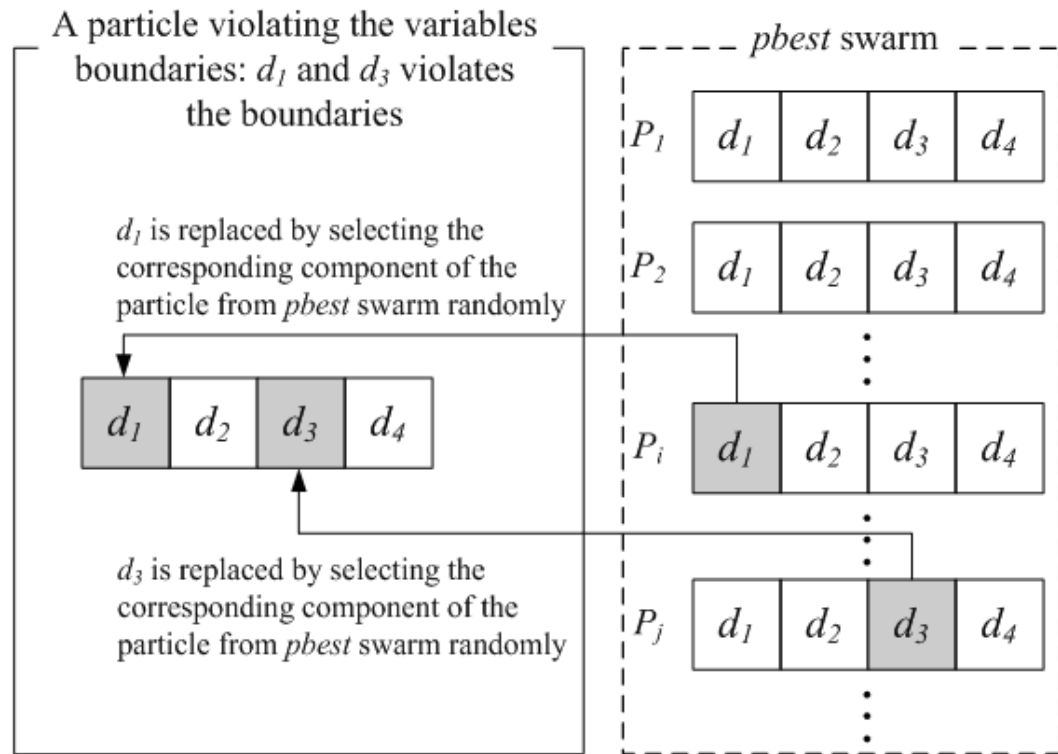


Figure 5.6 Illustration of the variable limits handling strategy

#### 5.4.4 Algorithm description

Based on the basic PSO algorithm and variable limits handling strategy as explained above, the pseudo-code for the presented PSO algorithm is listed in Table 5.3.

Table 5.3 The pseudo-code for the present PSO algorithm

---

Set  $k = 0$ ;

Randomly initialize positions and velocities of all particles distributed throughout the design space.

Calculate the objective function  $f(X_i^k)$  of the initialized particle.

Generate local best: Set  $P_i^k = X_i^k$ .

Generate global best: Find  $\min f(X_i^k)$ ,  $P_g^k$  is set to the position of  $X_{\min}^k$ .

WHILE (the maximum number of iterations are not met)

    FOR (each particle  $i$  in the swarm)

        Generate the velocity and update the position of the current particle  $X_i^k$ .

        Variable limit handling: Check whether each component of the current particle violates its corresponding boundary or not. If it does, select the corresponding component of the vector from  $pbest$  swarm randomly.

        Calculate the objective function  $f(X_i^k)$  of the current particle.

        Update  $pbest$ : Compare the function value of  $pbest$  with  $f(X_i^k)$ . If the  $f(X_i^k)$  is better than the function value of  $pbest$ , set  $pbest$  to the current position  $X_i^k$ .

        Update  $gbest$ : Find the global best position in the swarm. If the  $f(X_i^k)$  is better than the function value of  $gbest$ ,  $gbest$  is set to the position of the current particle  $X_i^k$ .

    END FOR

    Set  $k = k + 1$

END WHILE

---

## 5.5 Results and discussion

The optimization problems introduced in section 3 are implemented by using the above PSO algorithm. For all these optimization problems, a population of 20 individuals is used. The maximum number of iterations is limited to 100.

### 5.5.1 Case 1: Minimization of the maximum hoop TRS

Figure 5.7 provides a convergence rate of the optimization procedure for case 1. It can be seen that the algorithm achieves the best solution after about 80 iterations. The maximum hoop TRS has been decreased to 0.22GPa. The convergence of the design variables during the iterations is shown in Figure 5.8. It can be observed that the thicknesses of the first, second and last layer of interface increase steadily up to their upper bounds, while the thickness of the third layer of interface decreases dramatically to its lower bound. The final optimized interphases thicknesses are:  $0.6 \mu m$ ,  $0.6 \mu m$ ,  $0.3 \mu m$ ,  $0.6 \mu m$ .

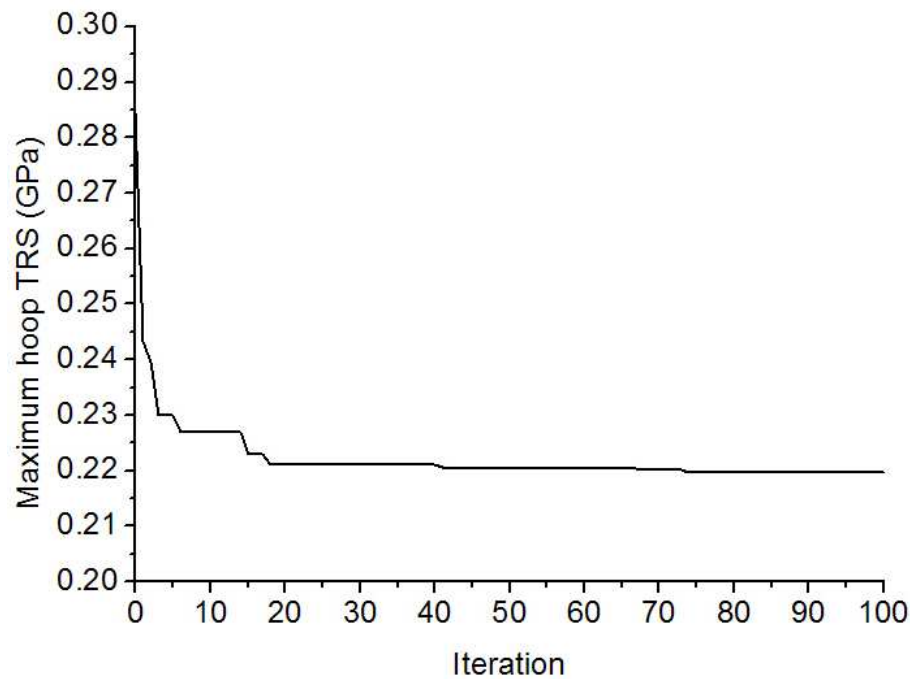


Figure 5.7 Convergence rate for the optimization of hoop TRS

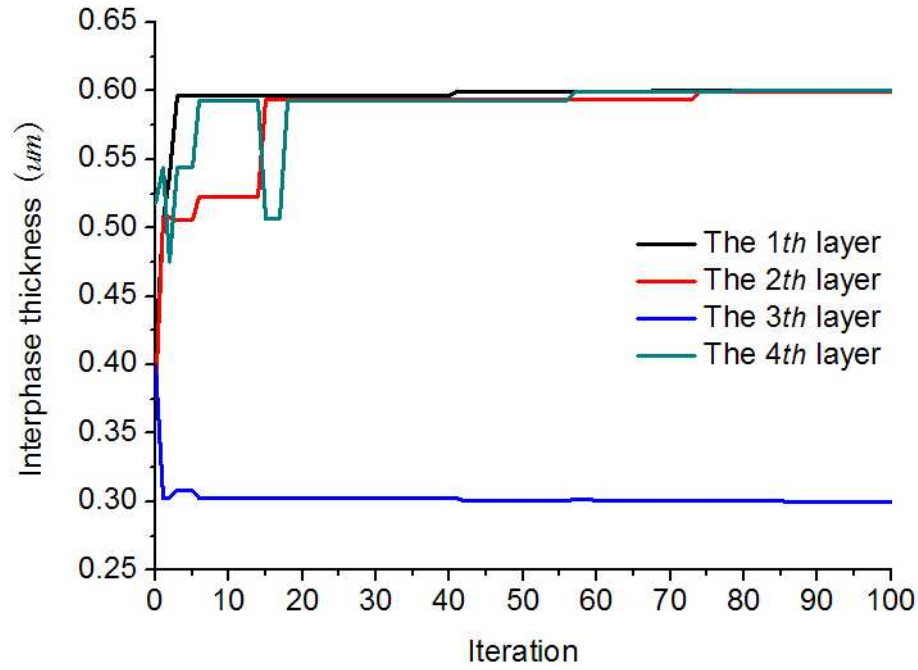


Figure 5.8 Iterations of the design variables for the case 1

### 5.5.2 Case 2: Minimization of the maximum radial TRS

Figure 5.9 provides a convergence rate of the optimization procedure for case 2. The algorithm achieves the best solution after about 70 iterations. The maximum radial TRS has been decreased to -0.068GPa. Correspondingly, iterations of the design variables are shown in Figure 5.10. The thicknesses of the first and third layer of interface increase rapidly up to their upper bounds. The thickness of the second layer of interface increases steadily up to  $0.5 \mu m$ . The thickness of the last layer of interface decreases dramatically to its lower bound.

The final optimized interphases thicknesses are:  $0.6 \mu m$ ,  $0.5 \mu m$ ,  $0.6 \mu m$ ,  $0.3 \mu m$ .

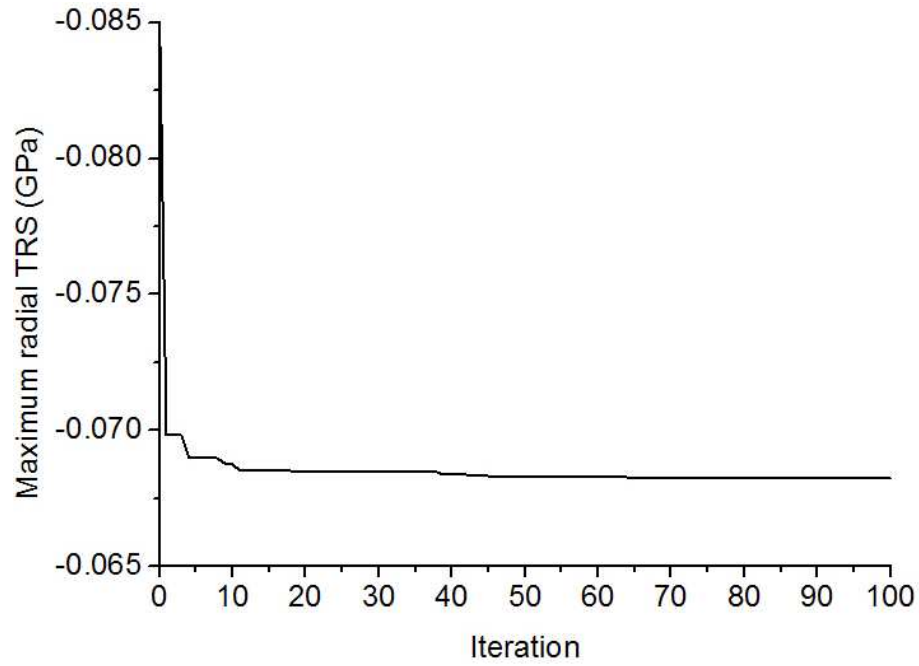


Figure 5.9 Convergence rate for the optimization of radial TRS

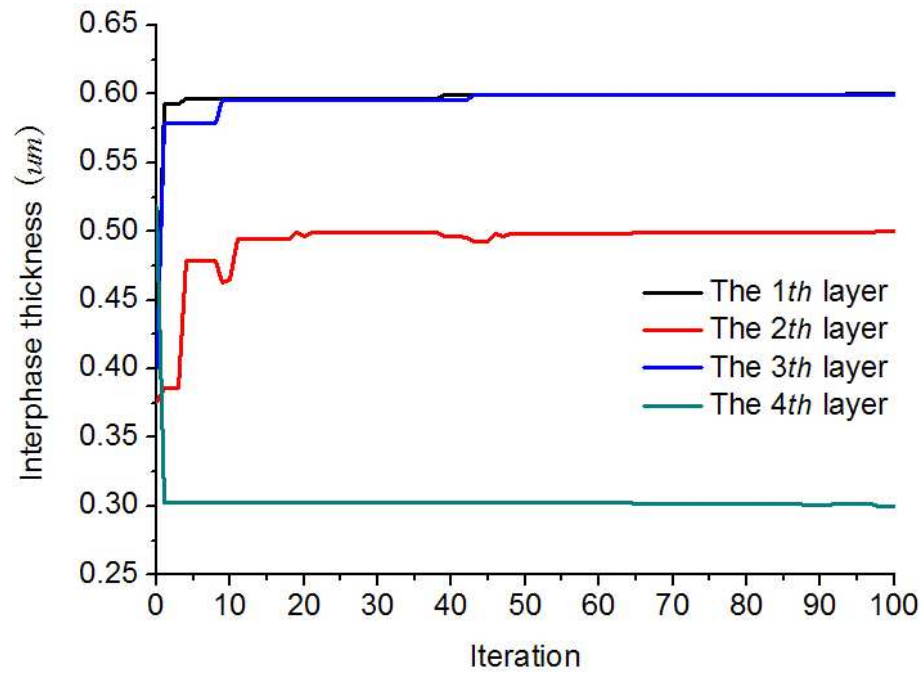


Figure 5.10 Iterations of the design variables for the case 2

### 5.5.3 Case 3: Minimization of the maximum axial TRS

Figure 5.11 provides a convergence rate of the optimization procedure for optimization case 3. It can be seen that the algorithm achieves the best solution after about 50 iterations. The



maximum axial TRS has been decreased to 0.12GPa. Figure 5.12 illustrates the iterations of the design variables. It can be observed that the thicknesses of the first, second and last layer of interface increase steadily up to their upper bounds, while the thickness of the third layer of interface decrease steadily to its lower bound. The final optimized interphases thicknesses are:  $0.6\ \mu m$ ,  $0.6\ \mu m$ ,  $0.3\ \mu m$ ,  $0.6\ \mu m$ .

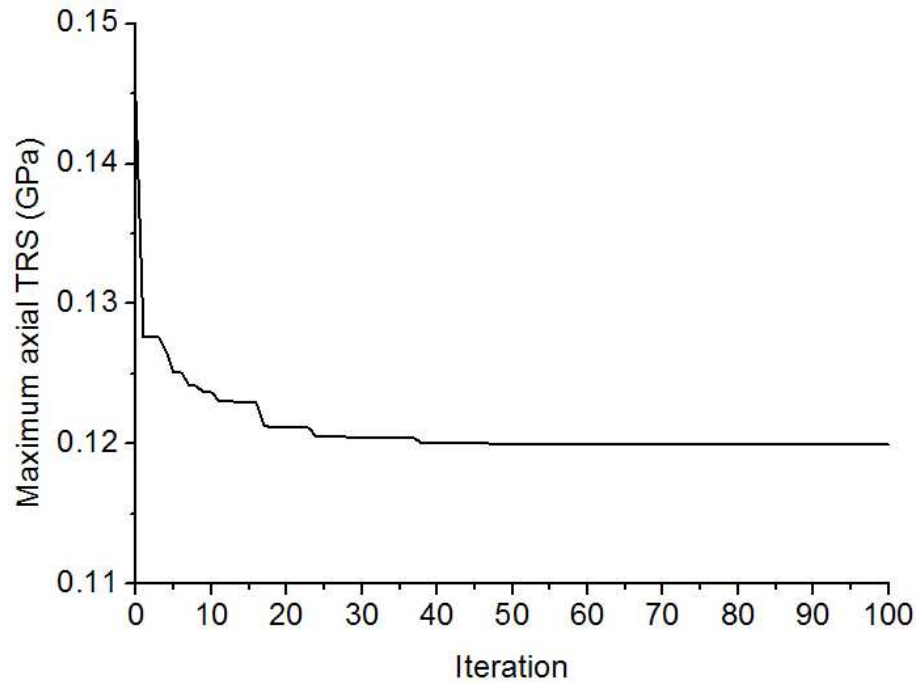


Figure 5.11 Convergence rate for the optimization of axial TRS

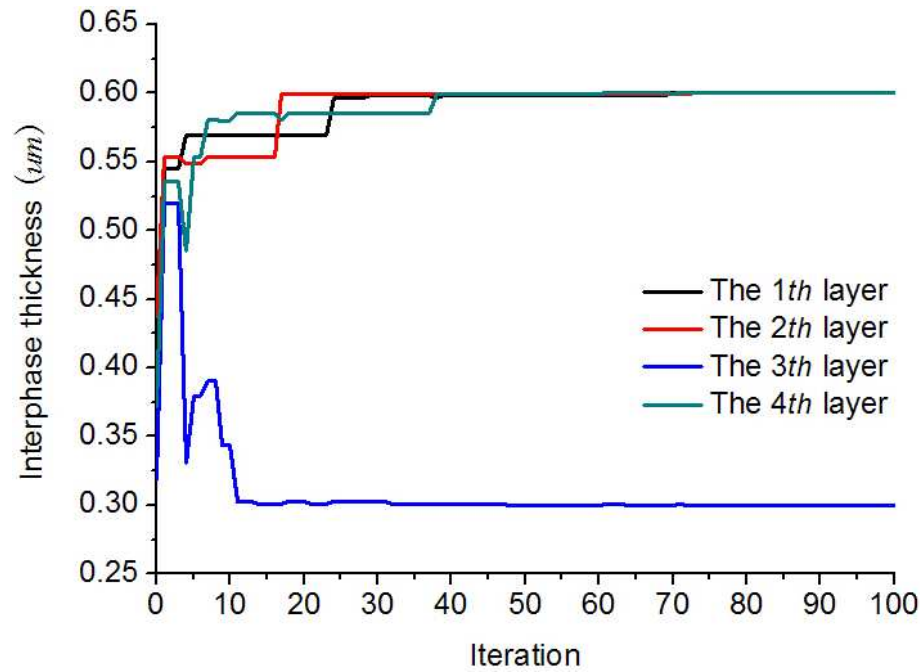


Figure 5.12 Iterations of the design variables for the case 3

## 5.6 Conclusions

Optimal design of 1-D unidirectional C/SiC composites with multi-layer interfaces with respect to the induced TRS when cooling down from the processing temperature is obtained by the use of the optimization algorithm PSO described in this chapter. The finite element models of RVC of 1-D unidirectional C/SiC composites with multi-layer interfaces are firstly generated and finite element analysis is realized to determine the TRS distributions. Then, an optimization scheme which combines a PSO algorithm with the finite element analysis is used to reduce the TRS in the C/SiC composites by designing the multi-layer interfaces thicknesses.

PSO algorithm does not use the gradient information of the optimization problem. This means that it does not require for the optimization problem to be differentiable and convex as is required by classical optimization methods such as gradient descent or quasi-Newton methods. The PSO algorithm is a population-based algorithm which means that it converges rather to a global optimum in opposite to the gradient methods which can find only local optima. This advantage of PSO algorithm and their ability to accurately satisfy the objective function guarantees reliable solutions of complicated engineering problems like those analyzed here.

Considering most previous applications of PSO for composites, one can state that they are focused on ply thicknesses and orientation angles optimization of composites laminates. The present extension to C/SiC composites thereby extends the applicability of PSO algorithm.

## **Chapter 6: Numerical simulation of the oxidation of C/SiC composites exposed to intermediate temperature oxidizing environments**

### **6.1 Introduction**

Many typically C/SiC components, e.g. combustor liners for gas turbine engines and filters for the energy and chemical industries, would be applied in intermediate and elevated temperature oxidizing environments over periods of time that are measured in hundreds of hours. However, the susceptibility of the carbon phases (carbon interfaces and fibers) to oxidation in such environments has hindered the long-term reusable applications of C/SiC composites. Due to extensive mismatch of the coefficients of thermal expansion (CTE) between the constituents (carbon fiber, carbon interface and SiC matrix), the tensile stresses are generated upon cooling from processing to room temperatures and result in the formation of micro-cracks in the SiC matrix. These micro-cracks act as oxygen transport paths, the exposed carbon interfaces and fibers are susceptible to the oxidation, which leads to degradation of the properties of composites and failure of components. Thus, the successful implementation of C/SiC components in the envisioned applications will depend on assessing the oxidation mechanisms and kinetics of C/SiC composites and on the availability of design methodologies to predict their properties degradation over periods of time comparable to their expected service life.

In this regard, many experimental works have been done to study the oxidation behavior of C/SiC composites and describe the influence of degradation of interfaces and fibers by oxidation on the mechanical behaviors of composites [60-65]. Numerical models [66-70] have also been developed to study the physics of the oxidation process in C/SiC composites and evaluate the influence of environment on the weight loss behavior of composites. Although these numerical models have provided insight into the physics of oxidation of C/SiC composite, the following limits still exist. Firstly, these models are not readily

applicable to model the complex morphologies of oxidized material microstructures and thus can not provide an intuitive visualization of the oxidation effect on CMC-SiC. Secondly, these approaches are mostly limited to the weight loss evaluation and unable to predict the degraded stiffness and strength of oxidized materials as a function of time and environment parameters. Especially as far as an accurate evaluation of degraded properties is concerned, an accurate modelling of the oxidized microstructure morphology and the efficient prediction of the degradation of material properties become a challenging topic.

Motivated by such situations, a numerical model which incorporates the modeling of oxidized microstructure and computing of degraded elastic modulus is presented in this chapter to simulate the oxidation behaviors of 2-D woven C/SiC composites at intermediate temperature ( $T < 900^{\circ}\text{C}$ ). Due to the complexity in simulating the oxidation kinetics of multi-layer materials, the present study only concerns the C/SiC composites with single-layer interface and matrix, just as the other existed models. Considering the fact that the oxidation of carbon phases in the C/SiC composite is uniform as the temperature is below  $900^{\circ}\text{C}$ , the oxidized microstructure morphology is modeled in the representative volume cell (RVC) of composites. Meanwhile, the strain energy method is adopted to evaluate the residual stiffness of oxidized material. Note that the oxidation simulation of C/SiC composite at higher temperature ( $T > 900^{\circ}\text{C}$ ) is not taken into account in this study, since modelling accurately the complicated oxidized microstructure morphology and non-uniform degradation of carbon phases from the material surface to the interior is very cumbersome and impractical at present.

This chapter is organized as follows. In the first section, the material microstructure of 2-D woven C/SiC composites at room temperature is analyzed and modeled on microscopic and macroscopic scales. In the second section, the oxidation process of carbon phases in the composite materials is simulated on microscopic scale; the oxidized RVC microstructure is then modeled on microscopic scale and compared with the experimentally observed morphology. In the third section, the two-level evaluation strategy involved environment parameters is presented to predict the elastic properties of oxidized composite. In the last section, the elastic properties of a 2-D woven C/SiC composite in air oxidizing environment are evaluated and validated in comparison to experimental data presented in [65]. Moreover,

the environmental parameters, i.e., temperature and pressure are studied to show their influences upon the oxidation behavior of 2-D woven C/SiC composite.

## **6.2 Modelling of the microstructure with cracks of 2-D woven C/SiC composites**

First, a brief introduction is given about the fabrication process of 2-D woven C/SiC composites with single-layer interface and matrix. The architecture of a 2-D woven C/SiC composite consists of carbon fibers arranged in tows. These tows are basically used in the construction of a 2-D plain weave to form a single lamina. Several such laminas are then assembled to form a composite sheet. The laminate stack is then infiltrated with one layer of carbon interface and one layer of SiC matrix around the carbon fibers.

Due to extensive mismatch of the coefficients of thermal expansion (CTE) between the constituents (carbon fiber, carbon interface and SiC matrix), the tensile stresses are generated upon cooling from processing to room temperatures and result in the formation of micro-cracks in the SiC matrix. These cracks embedded in the matrix and perpendicular to the fiber axes appear to be homogeneously distributed with an average spacing according to the scanning electron microscope (SEM) observation [117-118]. In fact, these matrix cracks provide an path for oxygen ingress that further leads to the oxidation of the carbon fibers and interfaces and thus have direct impacts on the properties of composite. Therefore, an exact microstructure modelling including the cracks within the composites should be established before the oxidation simulation. Notice that in order to simplify the modelling of the RVC microstructure and improve the computational efficiency, the cracks in C/SiC composites with multi-layer interfaces and matrices are not concerned in other chapters, which have been proved reasonable in the simulation of non-oxidized composites by comparing the numerical results with the experimental ones.

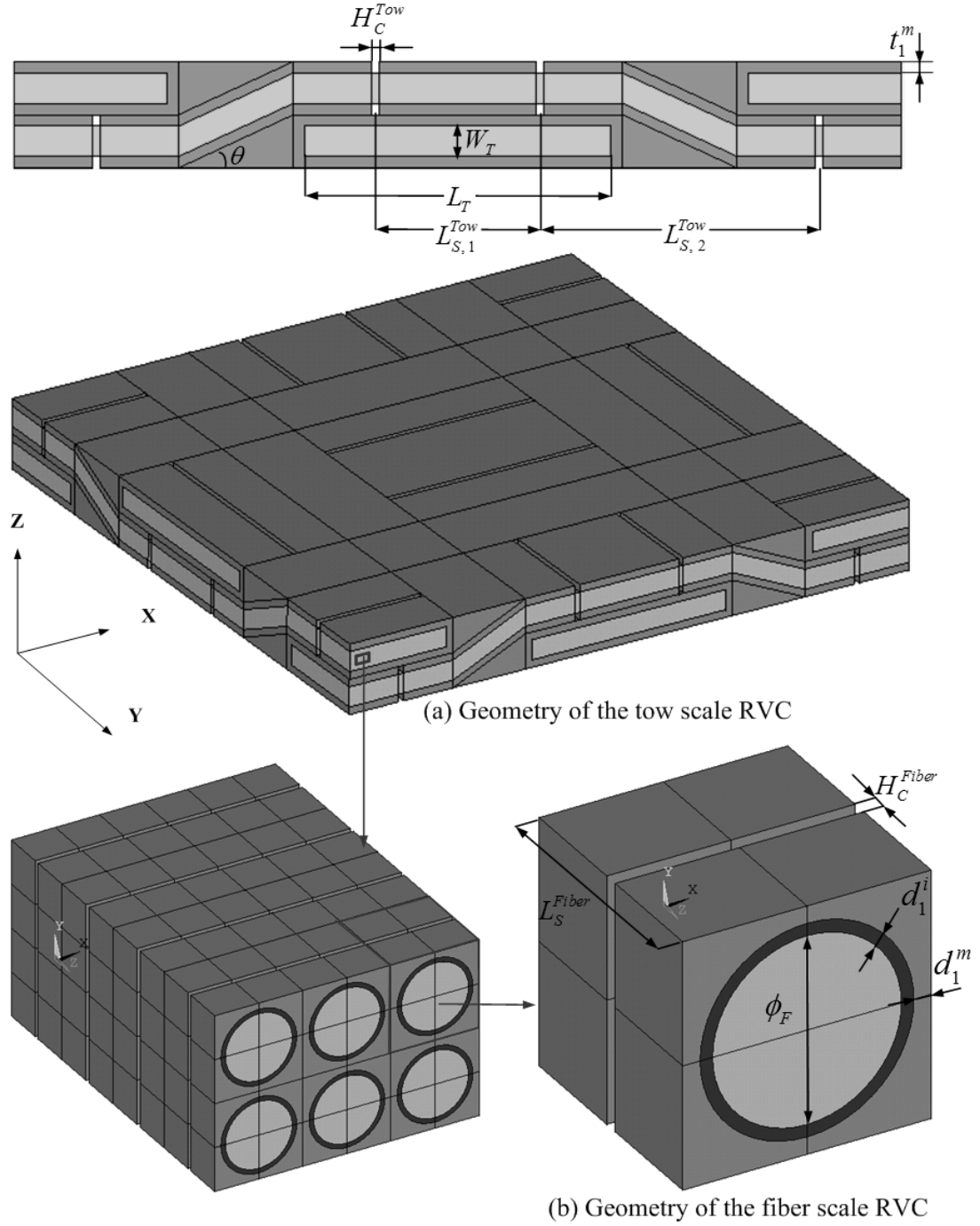


Figure 6.1 Geometry of the RVC microstructure with cracks of 2-D woven C/SiC composites

Regarding the multi-scale characteristics, the microstructure modelling of the RVC related to the 2-D woven C/SiC composites is carried out on fiber scale and tow scale, respectively. In Figure 6.1a, geometric parameters of tow scale RVC are given:  $L_T$  and  $W_T$  are sizes of the cross section of tow;  $L_{S,1}^{Tow}$  and  $L_{S,2}^{Tow}$  are crack separations on the tow scale;  $t_1^m$  is thickness of the SiC matrix;  $H_C^{Tow}$  is crack length on the tow scale and  $\theta$  is average undulation angle

with the horizontal plane. Related parameters of the RVC on the fiber scale are illustrated in Figure 6.1b:  $\phi_F$  is fiber radius;  $L_S^{Fiber}$  is crack separation on the fiber scale;  $d_1^i$  is thickness of the carbon interface;  $d_1^m$  is thickness of the SiC matrix and  $H_C^{Fiber}$  is crack length on the fiber scale.

### 6.3 Modelling of the microstructure of oxidized 2-D woven C/SiC composites

Experimental researches of the reaction mechanisms/kinetics and oxidized microstructure characteristics show that the oxidation kinetics of C/SiC composites can be divided into three domains [60-62]:

- $400^\circ\text{C} < T < 900^\circ\text{C}$ : intermediate temperatures. The rate of the reaction between carbon and oxygen controls the oxidation kinetics and associates with a uniform degradation of carbon reinforcement.
- $900^\circ\text{C} < T < 1100^\circ\text{C}$ : high temperatures. The oxidation is controlled by gas diffusion through the matrix micro-cracks, resulting in a non-uniform degradation of carbon phases.
- $T > 1100^\circ\text{C}$ : extreme high temperature. Micro-crack is sealed by silica and the oxidation is controlled by oxygen diffusion through  $\text{SiO}_2$  scale and the oxidation mainly takes place on materials surfaces.

This study concerns the oxidation of 2-D woven C/SiC composites at intermediate temperatures in a gas oxidizing environment in which oxygen is present. The oxygen achieves access to the interior of the composites via an interconnected network of passageways formed by the matrix cracks. Oxygen attacks the carbon phases (fibers and interfaces) in C/SiC composites both on the surface and in the interior of the composites. The modeling of oxidized microstructure morphology is hence carried out on the fiber scale RVC. In the present study, the oxidized microstructure morphology of 2-D C/SiC composite is modeled by means of an oxidized RVC at microscopic scale. Figure 6.2 gives a schematic presentation of the 2-D computational model in polar coordinate system at microscopic scale.



The oxygen firstly achieves the surface of the carbon interface via the matrix crack. Subsequently, the oxygen diffuses from the pole (point  $O$ ) into the interior of composites and reacts with the carbon interface and fiber. In Figure 6.2,  $r_I$  and  $r_F$  denote respectively the oxidation lengths within the interface and fiber;  $\theta$  is the inclined angle between the oxidation orientation and horizontal direction. The thick solid curve in Figure 6.2 represents the contour of oxidation void at instant  $t$ . After a time increment of  $dt$ , the oxidation of the carbon phase generates a new void contour marked by a dashed curve.

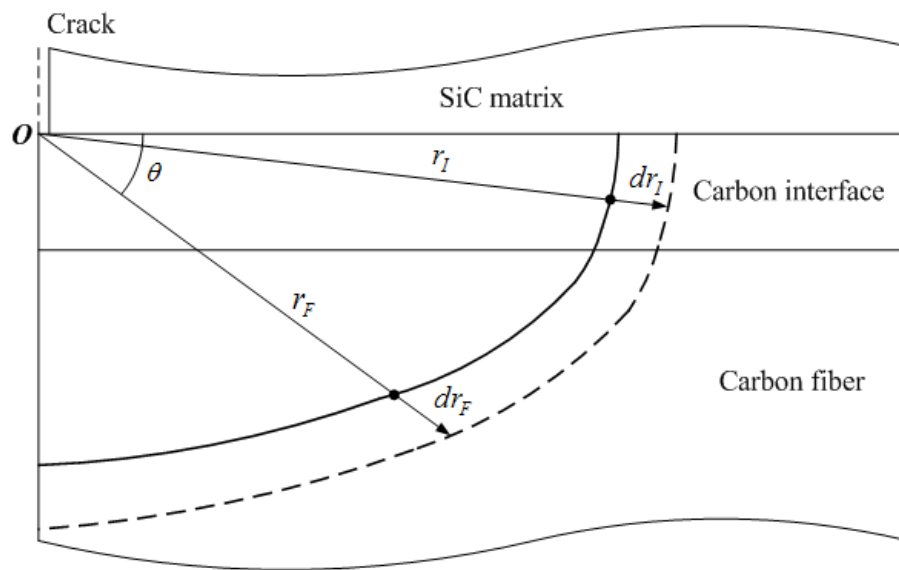


Figure 6.2 The schematic representation of the oxidation of 2-D C/SiC composite

The modelling of oxidized microstructure thus focuses on the determination of the curve function of the oxidation void contour. To this end, two steps are used in this study:

- The oxidation rates of carbon interface and fiber are firstly calculated.
- The oxidation lengths within the interface and fiber are then computed and the oxidation void contour is obtained.

### 6.3.1 Determination of oxidation rates of carbon phases

In the presence of oxygen, the oxidation reaction of carbon leads to a carbon oxide, then to a carbon dioxide. Finally, the reaction being modeled is



The oxidation rate  $R_C$ , i.e. the rate at which carbon recedes can be written as

$$R_C = K_C C_{O_2} \quad (6.2)$$

where  $K_C$  is the reaction rate constant of the oxidation reaction of carbon.  $C_{O_2}$  is the oxygen concentration at the  $C-O_2$  reaction interface. Since the oxygen reaction with carbon is so slow at intermediate temperatures, oxygen is able to completely diffuse from the surface into the interior of composites. The oxygen concentration at the  $C-O_2$  reaction boundary is found to be equal to the oxygen concentration at the composite surface and can be calculated from the ideal gas law

$$C_{O_2} = \frac{P_{O_2}}{RT} \quad (6.3)$$

where  $R$  is the gas constant and  $T$  is the absolute temperature.  $P_{O_2}$  is the partial pressure of oxygen calculated via Dalton's law of partial pressure

$$P_{O_2} = P_{air} f_{O_2} \quad (6.4)$$

where  $P_{air}$  is the air pressure and  $f_{O_2}$  is the mol fraction of the oxygen in the air.

The reaction rate constant  $K_C$  can be calculated by

$$K_C = k_0 \exp(-E_a/RT) \quad (6.5)$$

where  $k_0$  is the pre-exponential coefficient;  $E_a$  is the activation energy of the oxidation reaction.

From the above equation, it can be found that the activation energy and the temperature have direct influences on  $K_C$ . The reaction rate constant  $K_C$  depends on also the surface porosity and crystal structure of the carbon [68]. The experimental observation [119] shows that the carbon interface is homogenous while the carbon fiber is more crystalline in the interior than on the edge. Therefore, the reaction rate constant of carbon interface is isotropic and the oxidation rate of carbon interface can be easily obtained with the substitution of

Equations (6.3) and (6.5) into Equation (6.2)

$$R_C^I = k_0 \exp\left(-E_a^I/RT\right) \frac{P_{O_2}}{RT} \quad (6.6)$$

where  $R_C^I$  is the oxidation rate of carbon interface and  $E_a^I$  is the activation energy of the oxidation reaction of carbon interface.

Concerning the carbon fiber, it is known that the reaction rate constant of carbon fiber increases from the interior to the edge. Namely, the interior of carbon fiber is more oxidation resistant than the edge. Usually the carbon fiber edges are removed via oxidation approximately 10 times faster than the carbon fiber centers [120]. In this paper, following assumptions are made to describe the variation of the reaction rate constant over a carbon fiber:

- The material architecture of the carbon fiber consists of multi micro material-layers with homogeneous depth  $dh$ , as shown in Figure 6.3 and the reaction rate constant decreases linearly layer by layer from edge to center and is isotropic within each layer.
- The interface and the edge of carbon fiber contacted with the former have the same reaction rate constant, while the reaction rate constant of the centre is one tenth of that of the edge.

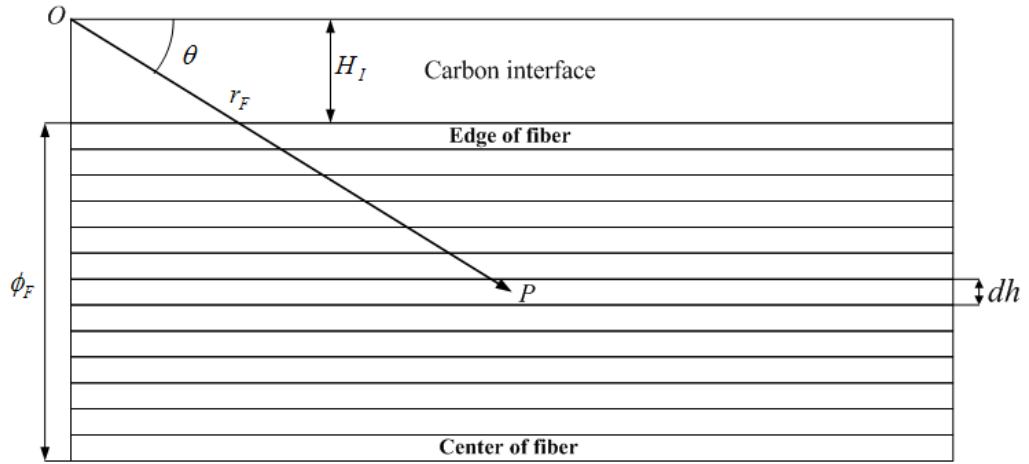


Figure 6.3 The computational model of the reaction rate constant of carbon fiber

Finally, the oxidation rate at an arbitrary point  $P$  along the direction  $O \rightarrow P$  shown in Figure 6.2 can be written as

$$\begin{aligned}
 R_C^F(P) &= \left[ K_C^{FE} - \frac{(r_F \sin \theta - H_I)}{\phi_F} (K_C^{FE} - K_C^{FC}) \right] \frac{P_{O_2}}{RT} \\
 &= \left[ K_C^{FE} - \frac{(r_F \sin \theta - H_I)}{\phi_F} (K_C^{FE} - K_C^{FE}/10) \right] \frac{P_{O_2}}{RT} \\
 &= K_C^{FE} \left[ 1 - 0.9(r_F \sin \theta - H_I)/\phi_F \right] \frac{P_{O_2}}{RT} \\
 &= k_0 \exp(-E_a^I/RT) \left[ 1 - 0.9(r_F \sin \theta - H_I)/\phi_F \right] \frac{P_{O_2}}{RT}
 \end{aligned} \tag{6.7}$$

Note that  $K_C^{FE}$  and  $K_C^{FC}$  represent the reaction rate constant of the edge and center of carbon fiber, respectively.  $R_C^F$  is the oxidation rate of carbon fiber.

### 6.3.2 Determination of oxidation void contour

According to Equations (6.6) and (6.7), it can be known that carbon interface has a homogenous oxidation rate while the oxidation rate of carbon fiber decreases gradually from edge to the center. In the present study, two models are developed for the determination of the void contour curves over the interface and fiber, respectively. Since at intermediate temperatures a reaction controlled regime is attained, the oxygen concentration is equal everywhere within the microstructure and the kinetic of gas diffusion is not involved in both two models.

#### 6.3.2.1 Modelling of the oxidation void contour in interface

For the computation model illustrated in Figure 6.2, the following differential equation can be obtained by considering the fact that the oxidation rate is equal to the ablation rate of carbon (in mol per unit time per area) [66]

$$R_C^I = \frac{1}{S} \times \frac{S \rho_C^I dr_I}{M_C^I dt} = \frac{\rho_C^I}{M_C^I} \times \frac{dr_I}{dt} \tag{6.8}$$

where  $S$  is the carbon interface/oxygen reaction surface area along the oxidation orientation;  $\rho_C^I$  and  $M_C^I$  are the density and molar mass of carbon interface, respectively.

The substitution of Equation (6.6) into Equation (6.8) yields

$$dr_I = k_0 \exp(-E_a^I/RT) \frac{P_{O_2} M_C^I}{RT \rho_C^I} dt \quad (6.9)$$

The integration of Equation (6.9) gives the oxidation length within the carbon interface

$$r_I = k_0 \exp(-E_a^I/RT) \frac{P_{O_2} M_C^I}{RT \rho_C^I} t \quad (6.10)$$

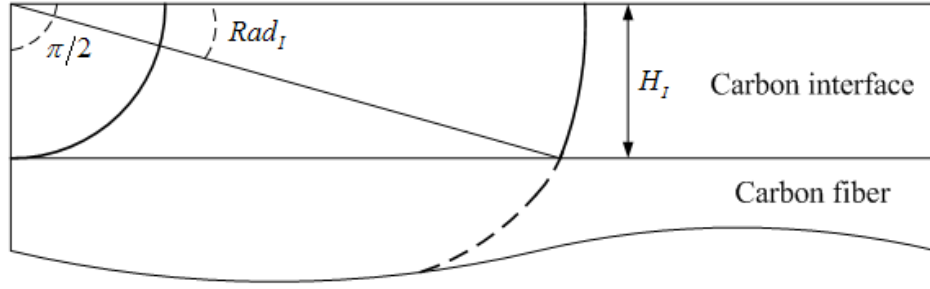


Figure 6.4 The void contour formed within the interface

The void contour is hence a circular arc. Obviously, the oxidation time has a direct influence on the void contour geometry. As shown in Figure 6.4,  $Rad_I$ , the radius of the circular arc can be expressed by the following relation

$$Rad_I = \arcsin \left( \frac{H_I RT \rho_C^I}{k_0 \exp(-E_a^I/RT) P_{O_2} M_C^I t} \right) \quad (6.11)$$

where  $H_I$  is the thickness of carbon interface. When the oxidation attaches the carbon interface, the critical time duration  $t_c$  can be calculated as

$$t_c = \frac{RT \rho_C^I H_I}{k_0 \exp(-E_a^I/RT) P_{O_2} M_C^I} \quad (6.12)$$

When the oxidation time exceeds  $t_c$ , the oxygen firstly reacts with the carbon interface and then oxidizes the carbon fiber.

Therefore, the oxidation void contour formed within the carbon interface can be expressed by the following equation in polar coordinate system

When  $t \leq t_c$ :

$$r_I = k_0 \exp(-E_a^I/RT) \frac{P_{O_2} M_C^I}{RT \rho_C^I} t \quad \text{with } 0 \leq \theta \leq \pi/2 \quad (6.13)$$

When  $t > t_c$  :

$$r_I = k_0 \exp(-E_a^I/RT) \frac{P_{O_2} M_C^I}{RT \rho_C^I} t \quad \text{with } 0 \leq \theta \leq \arcsin \left( \frac{H_I RT \rho_C^I}{k_0 \exp(-E_a^I/RT) P_{O_2} M_C^I t} \right) \quad (6.14)$$

### 6.3.2.2 Modelling of the oxidation void in fiber

Concerning the oxidation void formed within the fiber, it is known that the oxidation time exceeds  $t_c$  when the oxygen begins to react with the fiber. As shown in Figure 6.2, the oxidation length  $r_F$  consists of two parts: the length formed due to the oxidation in the interface and the length formed due to the oxidation in the fiber. The first part, i.e. the oxidation length within the interface can be easily calculated as

$$r_F' = H_I / \sin \theta \quad (6.15)$$

and the time duration of the oxidation within the interface can be obtained by means of Equation (6.10)

$$t' = \frac{RT \rho_C^I H_I}{k_0 \exp(-E_a^I/RT) P_{O_2} M_C^I \sin \theta} \quad (6.16)$$

Subsequently, the following differential equation can be derived by considering the equivalency of the oxidation rate and the ablation rate of carbon fiber

$$R_C^F = \frac{1}{S} \times \frac{S \rho_C^F dr_F}{M_C^F dt} = \frac{\rho_C^F}{M_C^F} \times \frac{dr_F}{dt} \quad (6.17)$$

where  $S$  is the carbon fiber/oxygen reaction surface area along the oxidation orientation;  $\rho_C^F$  and  $M_C^F$  are the density and molar mass of carbon fiber, respectively.

The substitution of Equation (6.7) into Equation (6.17) yields

$$\frac{1}{[1 - 0.9(r_F \sin \theta - H_I)/\phi_F]} dr_F = k_0 \exp\left(\frac{-E_a^I}{RT}\right) \frac{P_{O_2} M_C^F}{RT \rho_C^F} dt \quad (6.18)$$

Based on the boundary condition of Equation (6.16), the integration of Equation (6.18) gives the oxidation void contour formed within the carbon fiber

$$r_F = \frac{10R_F}{9\sin\theta} + \frac{H_I}{\sin\theta} - \exp\left(\ln\frac{10R_F}{9\sin\theta} - \frac{10\sin\theta M_C^F}{9\phi_F\rho_C^F}\left(k_0\exp\left(\frac{-E_a^I}{RT}\right)\frac{P_{O_2}}{RT}t - \frac{\rho_C^I H_I}{M_C^I \sin\theta}\right)\right)$$

$$\text{with } \arcsin\left(\frac{H_I RT \rho_C^I}{k_0 \exp(-E_a^I/RT) P_{O_2} M_C^I t}\right) < \theta \leq \pi/2 \quad (6.19)$$

### 6.3.3 Numerical simulation of oxidized microstructure morphology

So far, the complete contour curve of the oxidation void within the microscopic RVC has been obtained as

$$\text{When } t \leq \frac{RT \rho_C^I H_I}{k_0 \exp(-E_a^I/RT) P_{O_2} M_C^I} :$$

$$r = k_0 \exp(-E_a^I/RT) \frac{P_{O_2} M_C^I}{RT \rho_C^I} t \quad \text{with } 0 \leq \theta \leq \pi/2 \quad (6.20)$$

$$\text{When } t > \frac{RT \rho_C^I H_I}{k_0 \exp(-E_a^I/RT) P_{O_2} M_C^I} :$$

$$r = \begin{cases} k_0 \exp(-E_a^I/RT) \frac{P_{O_2} M_C^I}{RT \rho_C^I} t & \text{with } 0 \leq \theta \leq \arcsin\left(\frac{H_I RT \rho_C^I}{k_0 \exp(-E_a^I/RT) P_{O_2} M_C^I t}\right) \\ \frac{10R_F}{9\sin\theta} + \frac{H_I}{\sin\theta} - \exp\left(\ln\frac{10R_F}{9\sin\theta} - \frac{10\sin\theta M_C^F}{9\phi_F\rho_C^F}\left(k_0\exp\left(\frac{-E_a^I}{RT}\right)\frac{P_{O_2}}{RT}t - \frac{\rho_C^I H_I}{M_C^I \sin\theta}\right)\right) & \\ \text{with } \arcsin\left(\frac{H_I RT \rho_C^I}{k_0 \exp(-E_a^I/RT) P_{O_2} M_C^I t}\right) < \theta \leq \pi/2 \end{cases} \quad (6.21)$$

Figure 6.5 gives the computed oxidation void contours for an oxidized 2-D woven C/SiC composite exposed to 100KPa pressure air at 550°C at different instants. It can be observed that the size of oxidation void increases while the section of fiber exhibits a gradual diameter reduction as the oxidation time increases. Besides, from Equations (6.20) and (6.21), it can be easily found that the environment parameters, i.e., temperature and pressure, have direct influences on the morphologies of the oxidized microstructures. A detailed discussion about the influences will be made at the end of section 6.5.

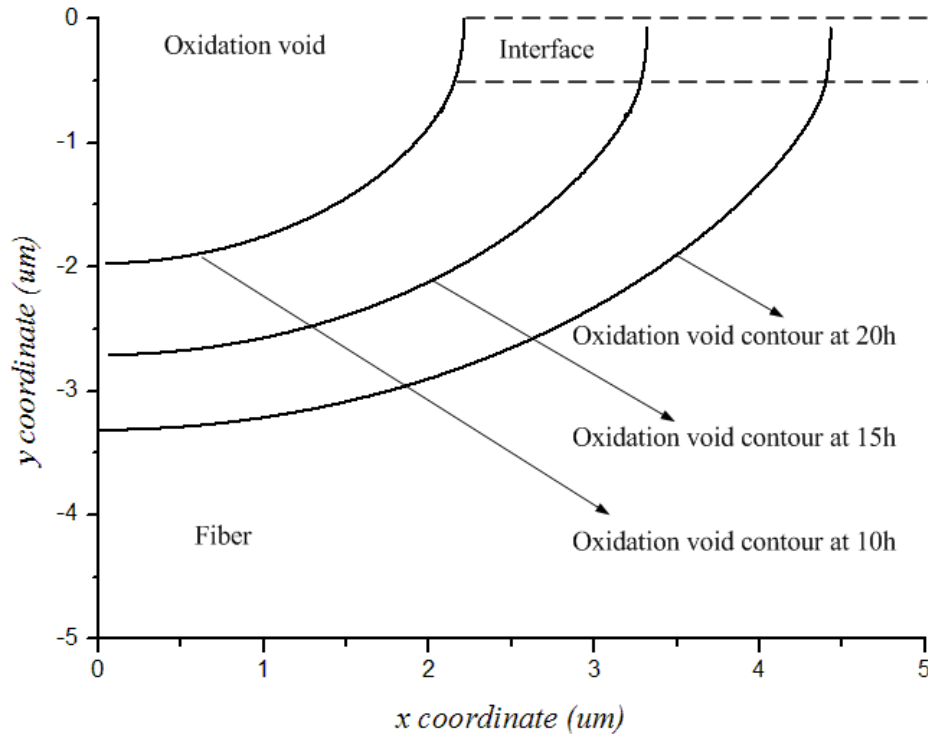


Figure 6.5 Computed oxidation void contours at different instants

Based on the obtained oxidation void contour, Figure 6.6 gives the computed microstructure morphologies of the 3D RVC for an oxidized 2-D C/SiC composite at different instants. Note that only 1/2 portion of the RVC is used to indicate the internal microstructure morphology. Since the micro cracks acted as oxygen diffusion paths, carbon fibers along the diffusion paths are ablated. It can be observed that the sections of carbon fibers that bridge the cracks have a reduced cross section due to oxidation, which is consistent with the experimental observation [65] as shown in Figure 6.6c. In addition, it can be seen that the ablations of carbon fiber and interface are gradually aggravated as the oxidation time increases. After about 56 hours of oxidization, the fiber is broken and attains a needle shape as shown in Figure 6.6e.



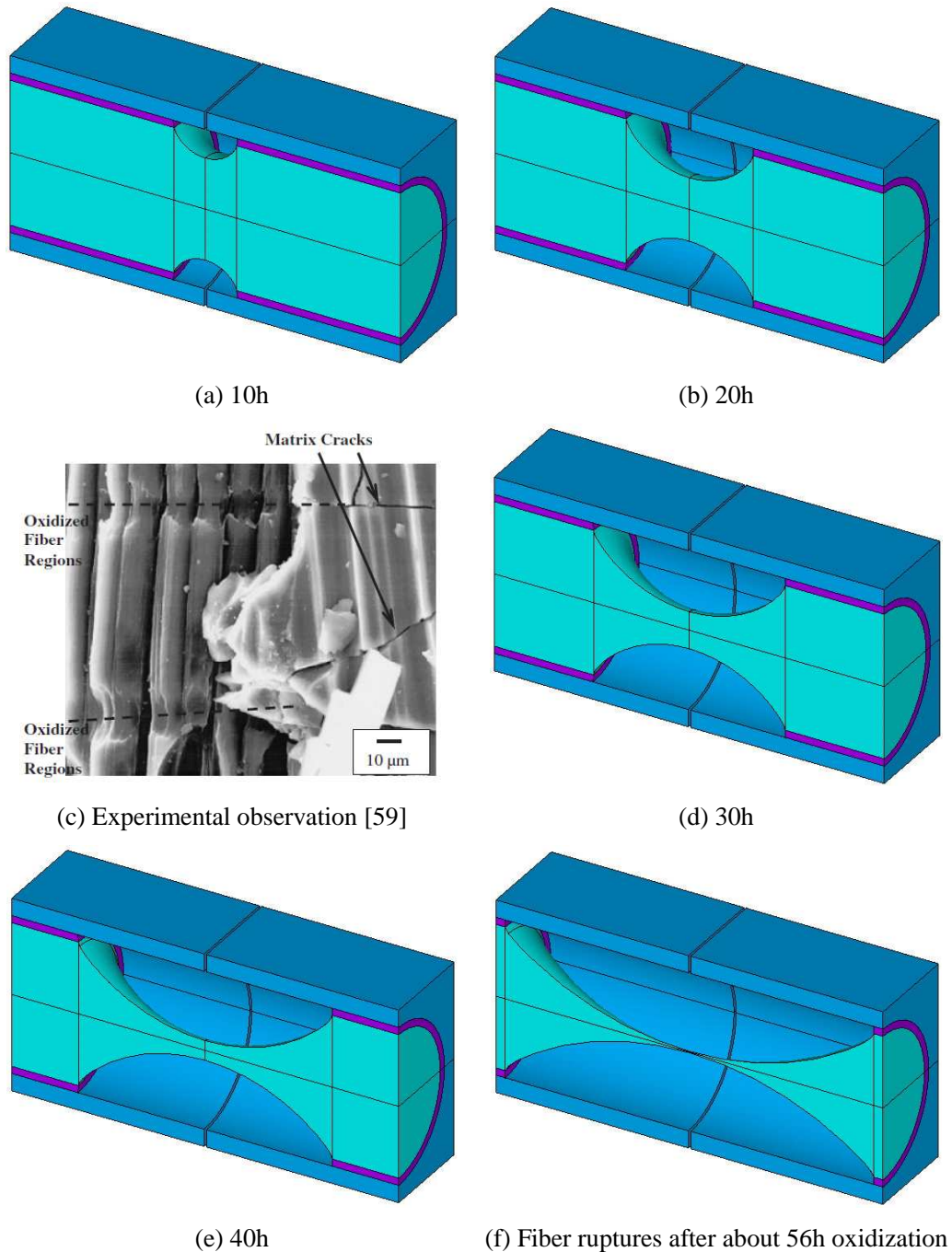


Figure 6.6 Morphologies of fiber scale RVC at different oxidation time

## 6.4 Two-level evaluation strategy of the degraded elastic properties

Considering the two-scale characteristics of the RVC microstructures of 2-D C/SiC composites, the two-level evaluation strategy is used for the prediction of the degraded elastic properties in oxidizing environment. To highlight the presentation, a flowchart is shown in Figure 6.7 to illustrate the stages involved in the multi-scale evaluation procedure. Here, RVC models of two scales are both established using ANSYS finite element software.

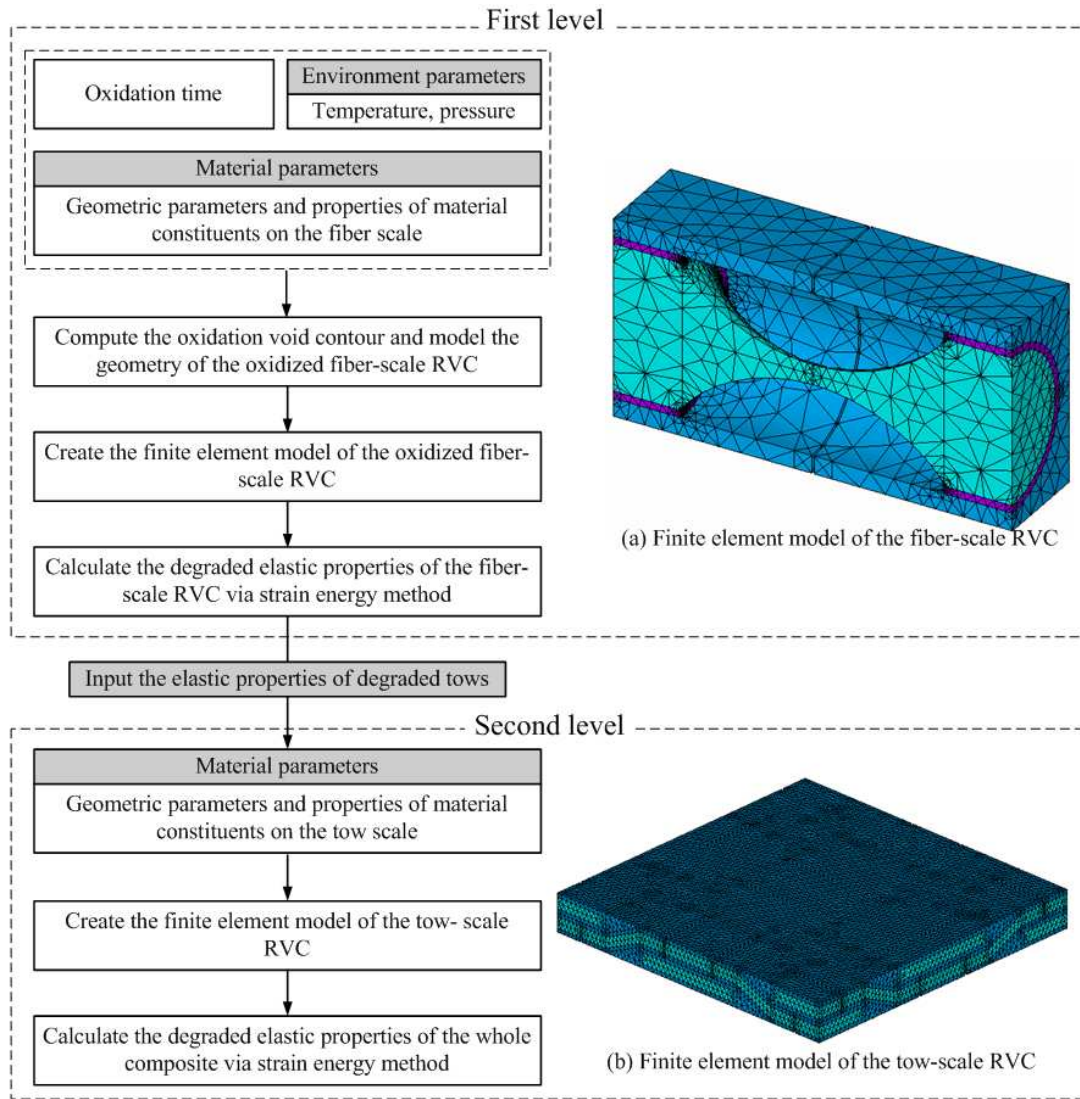


Figure 6.7 Illustration of the two-level evaluation procedure

(a) On the fiber scale, finite element model of the oxidized RVC is created according to the oxidation time, environment parameters (temperature and pressure) and material parameters (geometrical parameters and properties of constituents) as shown in Figure 6.7a. The strain energy method is then adopted to calculate the degraded elastic properties as a function of oxidation time and environment parameters. The results are further used for the fiber tows that are treated as a homogeneous transversely isotropic material.

(b) Based on the obtained elastic properties of fiber tows and the material parameters, finite element model of the RVC on the tow scale, as shown in Figure 6.7b, is created to evaluate effective elastic properties of the whole composite.

## 6.5 Numerical examples

### 6.5.1 Comparison with experimental results

In order to validate the present model, a numerical prediction of the degraded elastic properties is firstly investigated for an oxidized 2-D woven C/SiC composite exposed to 100KPa pressure air at 550°C for 25h and compared with the experimental data [65].

Table 6.1 Material constant values used for the numerical simulation

	Elastic properties					Oxidation reaction properties		
	$E_{xx}$ (GPa)	$E_{zz}$ (GPa)	$G_{xz}$ (GPa)	$\nu_{xy}$	$\nu_{zx}$	$\rho$ (kg/m <sup>3</sup> )	$M$ (kg/mol)	$E_a$ (kJ/mol)
Carbon fiber	22.0	220.0	4.8	0.42	0.12	2267.0	0.012	118.3
Carbon interface	12.0	30.0	2.0	0.4	0.12	2267.0	0.012	118.3
SiC matrix	350.0	-	145.8	0.2	-	-	-	-

The material constants used for the numerical simulation are given in Table 6.1. Table 6.2 lists the geometrical parameters of the RVC before oxidation, which are evaluated according to the experimental data.

Table 6.2 Geometrical parameters of the RVC before oxidation

Fiber-scale RVC ( $\mu m$ )							Tow-scale RVC (mm)				
$\phi_F$	$L_S^{Fiber}$	$d_1^i$	$d_1^m$	$H_C^{Fiber}$	$L_T$	$W_T$	$L_{S,1}^{Tow}$	$L_{S,2}^{Tow}$	$t_1^m$	$H_C^{Tow}$	$\theta$
5	25	0.5	1.25	0.15	4.0	0.4	2.0	3.94	0.15	0.1	20

The in-plane extensional modulus between the numerical solution and the experimental measurement is compared versus the time step in Figure 6.8. A close agreement is found between both. Here, the RVC microstructure morphologies after an oxidation of 5h, 15h and 25h are clearly indicated. It can be seen that as the oxidation time progresses, the ablation of carbon fibers and interfaces are gradually aggravated, which therefore leads to the degradation of effective elastic modulus.

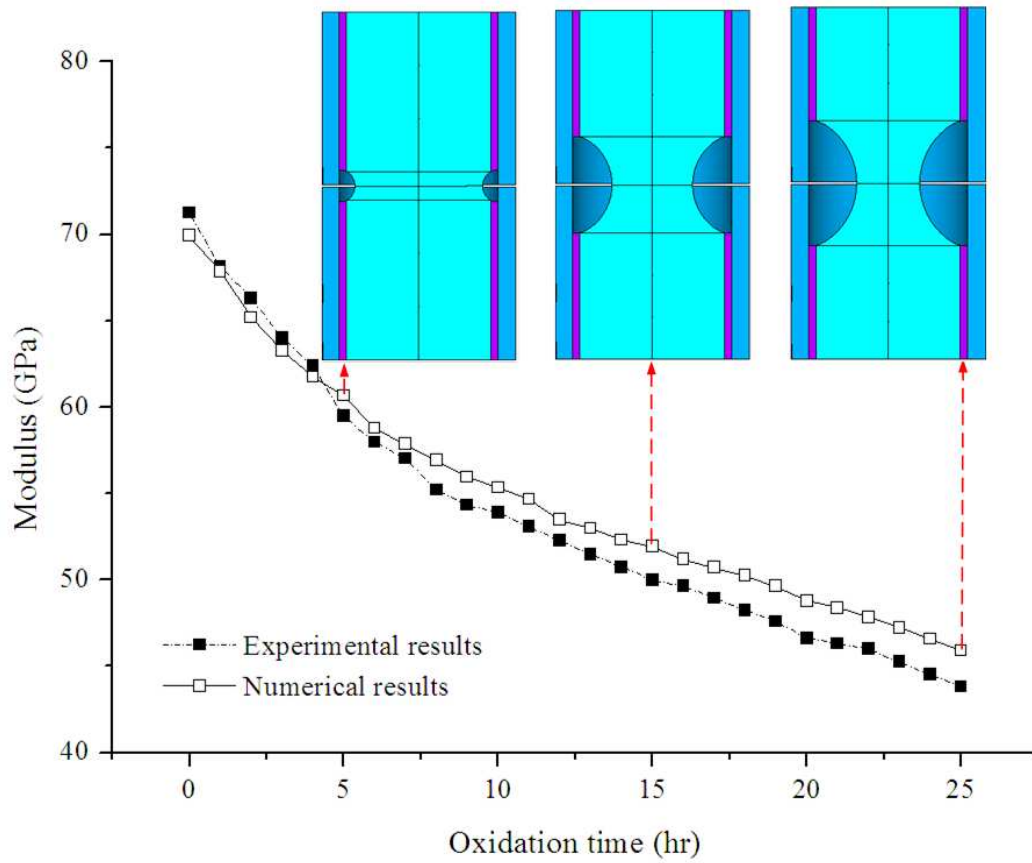


Figure 6.8 Elastic modulus versus oxidation time

### 6.5.2 Influence of temperature and pressure

Firstly, the microstructure morphology and effective elastic modulus of composite exposed to 100KPa pressure air are modeled by increasing the environmental temperature from 500°C to 650°C. Figure 6.9 shows the degraded in-plane extensional modulus and oxidized microstructure morphology as a function of the temperature after 5h oxidation. Then, the oxidation of composite exposed to pure oxygen at 550°C is simulated by increasing the pressure from 10KPa to 150KPa. The oxidized microstructure morphology and degraded in-plane extensional modulus of composite oxidized for 5h are shown in Figure 6.10.

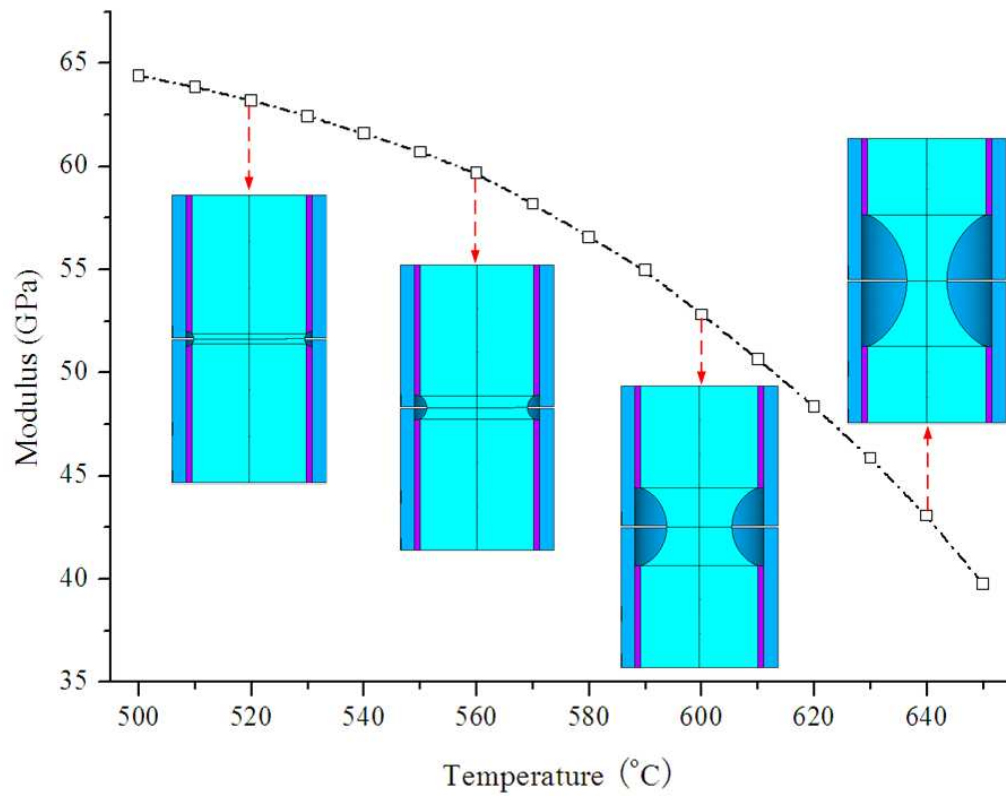


Figure 6.9 Elastic modulus versus temperature

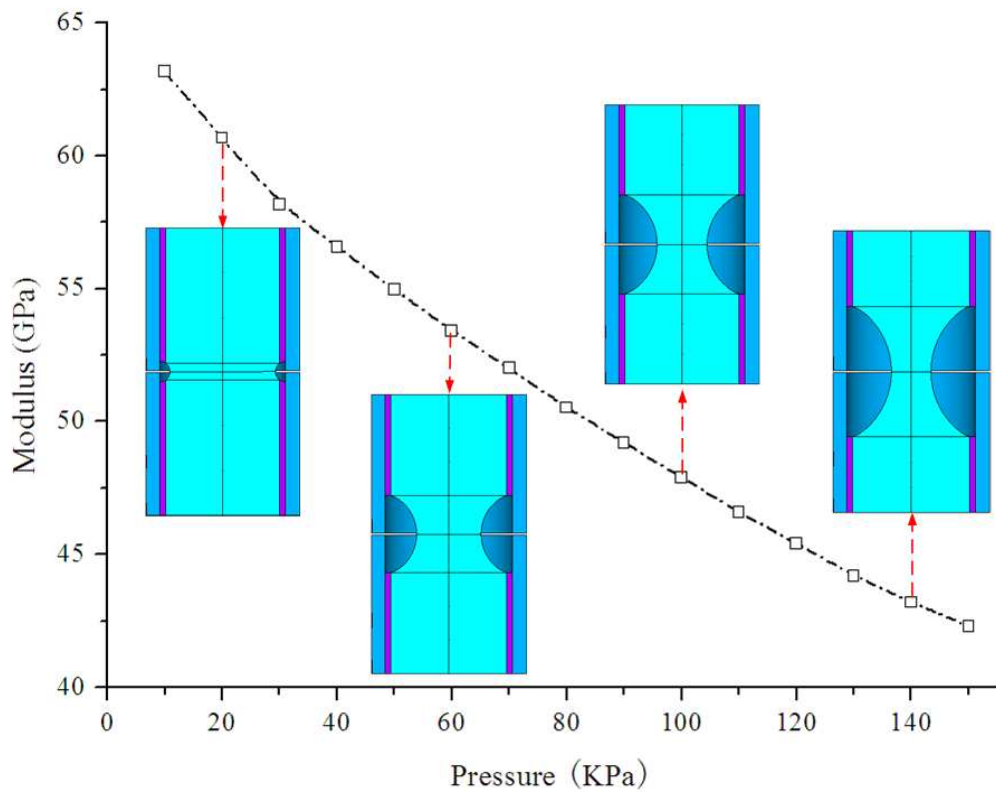


Figure 6.10 Elastic modulus versus pressure

It concludes that the environment parameters have a great influence on the composite degradation. The ablation of carbon phases is aggravated with the increase of temperature and pressure and therefore the elastic modulus of composite decreases gradually. In practical application, this is essential to determine the critical service life of a 2-D C/SiC composite structure from related environment parameters. When a lower bound of the degraded modulus is required, one can directly derive the maximum allowable oxidation time. In this example, although experimental data are not available for a systematic validation of the numerical predictions, the trends shown by Figures 6.9 and 6.10 are in good agreement with experimental observations.

## **6.6 Conclusions**

Numerical simulation and computing schemes have been developed to predict the properties degradation of 2-D woven C/SiC composite in gas oxidizing environments below 900°C. They are applied to simulate the microstructure oxidation and to predict the degraded elastic properties of 2-D woven C/SiC composite specimens studied experimentally by Halbig et al. [65]. It is found that the computed in-plane extensional moduli after oxidation are in good agreement with experimental data over the oxidation time. In addition, numerical results show that the temperature and pressure have a profound influence upon the oxidation results.

## Chapter 7: Conclusions and future works

### 7.1 Conclusions

1. An alternative finite element-based method called “strain energy method” is proposed for the numerical prediction of the effective elastic modulus and coefficients of thermal expansion (CTEs) of 3-D orthotropic composite materials. This method derives the effective elastic tensors and CTEs by analyzing the relationships between the strain energy of the microstructure and that of the homogenized equivalent model under specific thermo-elastic boundary conditions. Compared with the widely used homogenization method and finite element analysis method, the advantages of strain energy method rely on the simplicity of numerical implementation and the explicitly establishing of the closed-form expressions between the effective CTEs and the elastic tensors.
2. The two-scale RVC microstructures of 2-D woven and 3-D braided C/SiC composites with multi-layer interfaces and matrices are modelled. Compared with the traditional composites, the microstructures of C/SiC composites are very complex due to the multi-layer architecture in their geometrical configuration and the large heterogeneity of multi-phase materials. Geometrical descriptions and finite element modelling of the RVC microstructures are detailedly presented in the thesis. Mathematical relations among different geometrical parameters of the RVC microstructures are derived. A two-level evaluation strategy incorporated strain energy method is then proposed for the prediction of the effective properties of C/SiC composites.
3. The global/local analysis method is employed to determine the detailed stresses in the 2D woven C/SiC composite structures. Owing to the complex fiber-tow geometry of C/SiC composites, a reasonably discrete finite element model often requires a large number of three-dimensional elements even for a small portion of the composite structures, which leads to a very cumbersome computation process of the detailed stress analysis. Fortunately, the application of global/local method in the detailed stress analysis of

C/SiC composite structures has greatly improved the computational efficiency. In this thesis, the determination of the detailed stresses in the 2D woven C/SiC laminate structures is carried out sequentially from the homogenized composite structure of the macro-scale (global model) to the parameterized detailed fiber tow model of the micro-scale (local model). The bridge between two scales is realized by mapping the global analysis results as the boundary conditions for the local tow model. The stress results by global/local method are compared to those obtained by conventional finite element analyses. Results indicate that the global/local method could be an efficient tool for the detailed stress analysis of C/SiC composite structures and the adequate refined global mesh is required for accurate stress results.

4. Optimal design of 1D unidirectional C/SiC composites with multi-layer interfaces with respect to the induced TRS when cooling down from the processing temperature is studied. The finite element models of RVC of 1D unidirectional C/SiC composites with multi-layer interfaces are generated and finite element analysis is implemented to determine the TRS distributions. An optimization scheme which combines a modified particle swarm optimization (PSO) algorithm and the finite element analysis is used to reduce the TRS in the C/SiC composites by controlling the multi-layer interfaces thicknesses.
5. A numerical model which incorporates the modelling of oxidized microstructure and computing of degraded elastic moduli is presented for simulation of the oxidation behaviors of 2D woven C/SiC composites at intermediate temperature ( $T < 900^{\circ}\text{C}$ ). The morphologies of the RVC microstructure of oxidized composites are modelled based on the simulation of the void contours formed due to the oxygen diffusion through the matrix crack and subsequent oxidation. Considering the two-scale characteristics of the RVC microstructures of 2D woven C/SiC composites, a two-level evaluation strategy is used for the prediction of the degraded elastic properties in oxidizing environment. Numerical results show that: (1) as the oxidation time progresses, the ablation of carbon fibers and interfaces are gradually aggravated, which therefore leads to the degradation of effective elastic modulus. (2) The environment parameters have a great influence on the composite degradation. The ablation of carbon phases is aggravated with the increase



of temperature and pressure and therefore the elastic modulus of composite decreases gradually.

## 7.2 Future works

Several suggestions are offered here for potential future work that may be completed to extend the current body of the work, both in terms of further development and in terms of useful application.

1. Firstly, the presented RVC model and evaluation strategy can be employed to perform a parametric study of the effect of the microstructure geometry on the properties of C/SiC composites. For example, successive characterizations of a 3-D braided C/SiC composite with varying braiding angle, or thicknesses of interface and matrix layers could provide a useful insight into the effect which these parameters have on the elastic moduli and CTEs of the composite. This could also potentially lead to the ability to optimize the microstructure to a specific application.
2. Developing a model of progressive failure analysis of C/SiC composites represents another potential issue for future consideration. The progressive property degradation induced by a continued loading can be simulated within the finite element model of RVC. Failure is checked in each element against a given failure criterion. If the failure criterion is exceeded, the element is considered to have failed. The material of the failed element is assumed to be linearly elastic but with degraded stiffness. To simplify the simulation, a simple technique consisting of a reduction of the element stiffness to zero can be adopted when the element failure occurs.
3. In the current work, the modified PSO algorithm has been used to optimize the TRS distributions in C/SiC composites. This algorithm can be further applied in the optimization of C/SiC composites with other objective functions and constraints, such as the effective elastic and thermal properties, detailed stresses and oxidation behaviors.
4. In this thesis, a numerical model is proposed to simulate the oxidation behaviors of 2-D woven C/SiC composites in gas oxidizing environments. An immediate perspective is to address other composite architectures such as the 3-D braided C/SiC composite and to

extend the developed oxidation model to other oxidizing environments, like water or gas-water environments. Incorporating the progressive failure analysis with the oxidation model could be another potential future study. Many typically C/SiC components, e.g. combustor liners for gas turbine engines and filters for the energy and chemical industries, would be subjected to loadings in intermediate and elevated temperature oxidizing environments over periods of time. The successful implementation of C/SiC components in the envisioned applications will depend on assessing the effect of oxidation on the failure behavior over their service life and on the availability of design methodologies to predict their life under the expected service conditions.

## References

- [1] Herbell TP, Eckel AJ. Ceramic Matrix for Rocket Engine Turbine Applications. *Trans. ASME* 1993; 115: 64-69.
- [2] Effinger MR, Koenig JR, Halbig MC. C/SiC Mechanical and Thermal Design Data for a Turbopump Blisk. *Proceedings of the 21st annual Conference on Composites, Materials, and Structures*, Cocoa Beach, FL, 1997.
- [3] Hisaichi O, Masaki S, Masakazu O, Kaoru M, Tadashi S. Potential application of ceramic matrix composites to aero-engine components. *Composites: Part A* 1999; 30: 489-496.
- [4] Christin F. Design, Fabrication, and Application of Thermostructural Composites (TSC) Like C/C, C/SiC, and SiC/SiC Composites. *Advanced Engineering Materials* 2002; 4: 903-912.
- [5] Bouquet C, Fischer R, Larrieu JM, Uhrig G, Thebault J. Composite Technologies Development Status for Scramjet Applications. *Proceedings of the 12th AIAA International Space Planes and Hypersonic Systems and Technologies Conference*, Norfolk, VA, 2003.
- [6] Ortelt M, Weihs H, Fischer I, Dogigli M. Thermo-Mechanical Qualification Tests of Complex CMC Re-entry Structures. *Ceramic Engineering and Science Proceedings* 2003; 24: 81-87.
- [7] Krenkel W, Berndt F. C/C-SiC composites for space applications and advanced friction systems. *Materials Science and Engineering A* 2005; 412: 177-181.
- [8] Spriet P, Habarou G. Application of CMCs to Turbojet Engines: An Overview of the SEP Experience. *Key Engineering Materials* 1997; 127-131: 1267-1276.
- [9] Naslain R. Design, preparation and properties of non-oxide CMCs for application in engines and nuclear reactors: an overview. *Composites Science and Technology* 2004; 64: 155-170.
- [10] Zhang Y, Xu Y, Lou J, Zhang L, Cheng L, Lou J, Chen Z. Braking Behavior of C/SiC Composites Prepared by Chemical Vapor Infiltration. *International Journal of Applied*

- Ceramic Technology 2005; 2: 114-121.
- [11] Folsom G, Zok FW, Lange FF. Flexural properties of brittle multilayer materials: II experiments. *Journal of the American Ceramic Society* 1994; 77: 2081-2087.
- [12] Naslain R. The design of the fiber-matrix interfacial zone in ceramic matrix composites. *Composites Part A* 1998; 29: 1145-1155.
- [13] Han XF. Microstructure and properties of matrix modified C/SiC composites by pyrocarbon. Master Degree Thesis, Northwestern Polytechnical University, Department of Material Science, 2006.
- [14] Besmann TM, McLaughlin JC, Lin HT. Fabrication of Ceramic Composites: Forced CVI. *Journal of Nuclear Materials* 1995; 219: 31-35.
- [15] Ishikawa T, Chou TW. Stiffness and strength behavior of woven fabric composites. *Journal of Materials Science* 1982; 71: 3211-3220.
- [16] Ishikawa T, Chou TW. One-dimensional micromechanical analysis of woven fabric composites. *AIAA Journal* 1983; 21: 1714-1721.
- [17] Ishikawa T, Chou TW. In-plane thermal expansion and thermal bending coefficients of fabric composites. *Journal of Composite Materials* 1983; 17: 92-104.
- [18] Ishikawa T, Matsushima M, Hayashi Y, Chou TW. Experimental confirmation of the theory of elastic moduli of fabric composites. *Journal of Composite Materials* 1985; 19: 443-458.
- [19] Chou TW. Microstructural design of fiber composites. New York: Cambridge University Press, 1992.
- [20] Scida D, Aboura Z, Benzeggagh ML, Bocherens E. A micromechanics model for 3D elasticity and failure of woven-fibre composite materials. *Composites Science and Technology* 1999; 59: 505-517.
- [21] Tabiei A, Jiang Y. Woven fabric composite material model with material nonlinearity for nonlinear finite element simulation. *International Journal of Solids and Structures* 1999; 36: 2757-2771.
- [22] Tabiei A, Jiang Y, Yi W. A novel micromechanics-based plain weave fabric composite constitutive model with material nonlinear behavior. *AIAA Journal* 2000; 38(5).
- [23] Tabiei A, Jiang Y, Simitses J. Micromechanics-based plain weave fabric composites

- constitutive equations for local and global analysis. *Composites Science and Technology* 2000; 60: 1825-1833.
- [24] Tanov R, Tabiei A. Computationally efficient micro-mechanical woven fabric constitutive. *Journal of Applied Mechanics* 2001; 68: 553-560.
- [25] Tabiei A, Yi W. Comparative study of predictive methods for woven fabric composite elastic properties. *Composite Structures* 2002; 58: 149-164.
- [26] Yang JM, Ma CL, Chou TW. Fiber inclination model of three-dimensional textile structural composites. *Journal of Composite Materials* 1986; 20: 472-484.
- [27] Sun HY, Qiao X. Prediction of the mechanical properties of three-dimensionally braided composites. *Composites Science and Technology* 1997; 57: 623-629.
- [28] Whyte DW. On the structure and properties of 3-D braid reinforced composites. Ph.D. thesis, Drexel University, 1986.
- [29] Kalidindi SR, Abusafieh A. Longitudinal and transverse moduli and strengths of low angle 3-D braided composites. *Journal of Composite Materials* 1996; 30: 885-905.
- [30] Kalidindi SR, Franco E. Numerical evaluation of isostrain and weighted-average models for elastic moduli of three-dimensional composites. *Composites Science and Technology* 1997; 57: 293-305.
- [31] Zhang YC, Harding J. A numerical micromechanics analysis of the mechanical properties of a plain weave composite. *Computers & Structures* 1990; 36: 839-844.
- [32] Tang ZX, Postle R. Mechanics of three-dimensional braided structures for composite Materials-Part II: prediction of the elastic moduli. *Composite Structures* 2001; 51: 451-457.
- [33] Tang ZX, Postle R. Mechanics of three-dimensional braided structures for composite materials-part III: nonlinear finite element deformation analysis. *Composite Structures* 2002; 55: 307-317.
- [34] Tang XD, Whitcomb JD, Kelkar AD, Tate J. Progressive failure analysis of 2×2 braided composites exhibiting multiscale heterogeneity. *Composites Science and Technology* 2006; 66: 2580-2590.
- [35] Xu K, Xu XW. Finite element analysis of mechanical properties of 3D five-directional braided composites. *Materials Science and Engineering A* 2008; 487: 499-509.

- [36] Fang GD, Liang J, Wang BL. Progressive damage and nonlinear analysis of 3D four-directional braided composites under unidirectional tension. *Composite Structures* 2009; 89: 126-133.
- [37] Whitcomb JD, Srirengan K, Chapman C. Evaluation of homogenization for global-local stress-analysis of textile composites. *Composite Structures* 1995; 31: 137-149.
- [38] Srirengan K, Whitcomb JD, Chapman C. Model technique for three-dimensional global/local stress analysis of plainweave composites. *Composite Structures* 1997; 39: 145-156.
- [39] Hassani B, Hinton E. A review of homogenization and topology optimization. I-homogenization theory for media with periodic structure. *Computers & Structures* 1998; 69: 707-717.
- [40] Chung PW, Tamma KK, Namburu RR. A micro/macro homogenization approach for viscoelastic creep analysis with dissipative correctors for heterogeneous woven-fabric layered media. *Composites Science and Technology* 2000; 60: 2233-2253.
- [41] Chung PW, Tamma KK, Namburu RR. Asymptotic expansion homogenization for heterogeneous media: computational issues and applications. *Composite Part A* 2001; 32: 1291-1301.
- [42] Dasgupta A, Agarwal RK, Bhandarkar SM. Three-dimensional modeling of woven-fabric composites for effective thermo-mechanical and thermal properties. *Composites Science and Technology* 1996; 56: 209-223.
- [43] Carvelli V, Poggi C. A homogenization procedure for the numerical analysis of woven fabric composites. *Composites: Part A* 2001, 32: 1425-1432.
- [44] Feng ML, Wu CC. A study of three-dimensional four-step braided piezoceramic composites by the homogenization method. *Composites Science and Technology* 2001; 61: 1889-1898.
- [45] Dong JW, Feng ML. Asymptotic expansion homogenization for simulating progressive damage of 3D braided composites. *Composite Structures* 2010; 92: 873-882.
- [46] Camus G, Guillaumat L, Baste S. Development of damage in a 2D woven C/SiC composite under mechanical loading: I. Mechanical characterization. *Composites Science and Technology* 1996; 56: 1363-1372.

- [47] Bouazzaoui REI, Baste S, Camus G. Development of damage in a 2D woven C/SiC composite under mechanical loading: II. Ultrasonic characterization. *Composites Science and Technology* 1996; 56: 1373-1382.
- [48] Inghels E, Lamon J. An approach to the mechanical behavior of C/SiC and SiC/SiC ceramic matrix composites, part 1 experimental results. *Journal of Material Science* 1991; 20: 5403-5410.
- [49] Inghels E, Lamon J. An approach to the mechanical behavior of C/SiC and SiC/SiC ceramic matrix composites, part 2 theoretical approach. *Journal of Material Science* 1991; 20: 5411-5419.
- [50] Wang YQ, Zhang LT, Cheng LF, Mei H, Ma JQ. Characterization of tensile behavior of a two-dimensional woven carbon/silicon carbide composite fabricated by chemical vapor infiltration. *Materials Science and Engineering A* 2008; 497: 295-300.
- [51] Ji GC, Qiao SR, Du SM, Han D, Li M. Three-point bending fracture characteristics of three-dimensional-C/SiC with single-edge notch beam specimens. *Materials Science and Engineering A* 2008; 483-484: 123-126.
- [52] Cheng LF, Xu YD, Zhang LT, Zhang Q. Effect of heat treatment on the thermal expansion of 2D and 3D C/SiC composites from room temperature to 1400°C. *Carbon* 2003; 41: 1666-1670.
- [53] Zhang Q, Cheng LF, Zhang LT, Xu YD. Thermal expansion behavior of carbon fiber reinforced chemical-vapor-infiltrated silicon carbide composites from room temperature to 1400 °C. *Materials Letters* 2006; 60: 3245-3247.
- [54] Kumar S, Kumar A, Shukla A, Rohini Devi G, Gupta AK. Investigation of thermal expansion of 3D-stitched C-SiC composites. *Journal of the European Ceramic Society* 2009; 29: 2849-2855.
- [55] Sheikh MA, Taylor SC, Hayhurst DR, Taylor R. Microstructural finite-element modelling of a ceramic matrix composite to predict experimental measurements of its macro thermal properties. *Modelling and Simulation in Materials Science and Engineering* 2001; 9: 7-23.
- [56] Farooqi JK, Sheikh MA. Finite element modelling of thermal transport in ceramic matrix composites. *Computational Materials Science* 2006; 37: 361-373.

- [57] Lamouroux F, Bourrat X, Naslain R, Sevely J. Structure/oxidation behavior relationship in the carbonaceous constituents of 2D C/PyC/SiC composites. *Carbon* 1993; 31(8): 1273-1288.
- [58] Cheng LF, Xu YD, Zhang LT, Yin XW. Effect of carbon interlayer on oxidation behavior of C/SiC composites with a coating from room temperature to 1500°C. *Materials Science and Engineering A* 2001; 300: 219-225.
- [59] Yin XW, Cheng LF, Zhang LT, Xu YD, Li JZ. Oxidation behavior of 3D C/SiC composites in two oxidizing environments. *Composites Science and Technology* 2001; 61: 977-980.
- [60] Lamouroux F, Camus G. Kinetics and mechanisms of oxidation of 2D woven C/SiC composites: I, Experimental approach. *Journal of the American ceramic society* 1994; 77(8): 2049-2057.
- [61] Lamouroux F, Naslain R, Jouin J. Kinetics and mechanisms of oxidation of 2D woven C/SiC composites: II, Theoretical approach. *Journal of the American ceramic society* 1994; 77(8): 2058-2068.
- [62] Naslain R, Guette A, Rebillat F, Le Gallet S, Lamouroux F, Filipuzzi L, Louchet C. Oxidation mechanisms and kinetics of SiC-matrix composites and their constituents. *Journal of Materials Science* 2004; 39: 7303-7316.
- [63] Singh S, Srivastava VK. Effect of oxidation on elastic modulus of C/C-SiC composites. *Materials Science and Engineering A* 2008; 486: 534-539.
- [64] Halbig MC, Eckel AJ. Oxidation of continuous carbon fibers within a silicon carbide matrix under stressed and unstressed conditions. NASA/TM-2000-210224, 2000.
- [65] Halbig MC, McGuffin-Cawley JD, Eckel AJ, Brewer DN. Oxidation kinetics and stress effects for the oxidation of continuous carbon fibers within a microcracked C/SiC ceramic matrix composite. *Journal of the American ceramic society* 2008; 91(2): 519-526.
- [66] Zhang WG, Cheng HM, Xie TS, Shen ZH, Zhou BL, Sano H, Uchiyama Y, Kobayashi K. Oxidation kinetics and mechanisms of ceramic-carbon composites I. Modelling for the nonreactive ceramic layer type. *Carbon* 1998; 36(7-8): 991-995.



- 
- [67] Eckel AJ, Cawley JD, Parthasarathy TA. Oxidation kinetics of a continuous carbon phase in a nonreactive matrix. *Journal of the American ceramic society* 1995; 78(4): 972-80.
- [68] Halbig MC, Eckel AJ. Modelling the environmental effects on carbon fibers in a ceramic matrix at oxidizing conditions. NASA/TM/2000-210223, 2000.
- [69] Halbig MC, Cawley JD. Modeling the Oxidation Kinetics of Continuous Carbon Fibers in a Ceramic Matrix. NASA/TM/2000-209651, 2000.
- [70] Sullivan RM. A model for the oxidation of carbon silicon carbide composite structures. *Carbon* 2005; 43: 275-285.
- [71] Lachaud J, Bertrand N, Vignoles GL, Bourget G, Rebillat F, Weisbecker P. A theoretical/experimental approach to the intrinsic oxidation reactivities of C/C composites and of their components. *Carbon* 2007; 45: 2768-2776.
- [72] J. Lachaud, Y. Aspa, G.L. Vignoles. *International Journal of Heat and Mass Transfer* 2008; 51: 2614-2627.
- [73] Vignoles GL, Lachaud J, Aspa Y, Goyh  n  che JM. Ablation of carbon-based materials: Multiscale roughness modelling. *Composites Science and Technology* 2009; 69: 1470-1477.
- [74] Sun CT, Chen JL. A simple flow rule for characterizing nonlinear behavior of fiber composites. *Journal of Composite Material* 1989; 23: 1009-1020.
- [75] Aboudi J. Micromechanical analysis of composites by the method of cells. *Applied Mechanics Review* 1989; 42: 193-221.
- [76] Nemat-Nasser S, Hori M. *Micromechanics: overall properties of heterogeneous materials*. Amsterdam: Elsevier Science Publishers, 1993.
- [77] Kim SJ, Shim ES. A thermoviscoplastic theory for composite materials by using a matrix-partitioned unmixing-mixing scheme. *Journal of Composite Materials* 1996; 30: 1647-1699.
- [78] Yu XG, Cui JZ. A two-scale method for identifying mechanical parameters of composite materials with periodic configuration, *Acta Mechanica Sinica* 2006; 22: 581-594.
- [79] Haktan-Karadeniz Z, Kumlutas D. A numerical study on the CTE of fiber reinforced

- composite materials. *Composite Structures* 2007; 78: 1-10.
- [80] Dupel P, Langlais F, Pailler R. Pulse chemical vapour deposition and infiltration of pyrocarbon in model pores with rectangular cross-sections. Part 1-study of the pulsed process of deposition. *Journal of Materials Science* 1994; 29: 1341-1347.
- [81] Krenkel W. Microstructure Tailoring of C/C-SiC Composites. *Ceramic Engineering and Science Proceedings* 2003; 24: 471-476.
- [82] Wang YQ, Wang ASD. On the topological yarn structure of 3-D rectangular and tubular braided preforms. *Composites Science and Technology* 1994; 54: 575-586.
- [83] Wang YQ, Wang ASD. Microstructure/property relationships in three dimensional braided fiber composites. *Composites Science and Technology* 1995; 53: 213-222.
- [84] Pandey R, Hahn HT. Designing with 4-step braided fabric composites. *Composites Science and Technology* 1996; 56: 623-634.
- [85] Chen L, Tao XM, Choy CL. On the microstructure of three dimensional braided preforms. *Composites Science and Technology* 1999; 59: 391-404.
- [86] Tang ZX, Postle R. Mechanics of three-dimensional braided structures for composite materials-part I: fabric structure and fibre volume fraction. *Composite Structures* 2000; 49: 451-459.
- [87] Han XF. Microstructure and properties of matrix modified C/SiC composites by pyrocarbon. Master Degree Thesis, Northwestern Polytechnical University, Department of Material Science, 2006.
- [88] Ransom JB, Knight NF. Global/Local stress analysis of composite panels. *Computers and Structures* 1990; 37 (4): 375-395.
- [89] Luo J, Sun CT. Global-local methods for thermo-elastic stress analysis of thick fiber-wound cylinders. *Journal of Composite Materials* 1991; 25: 453-468.
- [90] Whitcomb JD, Sreirengan K, Chapman C. Evaluation of homogenization for global/local stress analysis of textile composites. *Composite Structures* 1995; 31: 137-149.
- [91] Srinivasan S, Biggers SB, Latour RA. Analysis of composite structures using the 3-D global/3-D local method. *Journal of Reinforced Plastics and Composites* 1997; 16: 353-371.

- [92] Srirengan K, Whitcomb JD, Chapman C. Modal technique for three-dimensional global/local stress analysis of plain weave composites. *Composite Structures*, 1997, 39: 145-156.
- [93] Vandeurzen PH, Ivens J, Verpoest I. Micro-stress analysis of woven-fabric composites by multi level decomposition. *Journal of Composite Materials*, 1998, 32: 623-651.
- [94] Woo K, Whitcomb JD. A post-processor approach for stress analysis of woven textile composites. *Composites Science and Technology* 2000; 60: 693-704.
- [95] Bobet JL, Naslain R, Guette A, Ji N, Lebrun JL. Thermal residual stresses in ceramic matrix composites-II: experimental results for model materials. *Acta Metallurgica et Materialia* 1995; 43(6): 2255-2268.
- [96] Bobet JL, Lamon J. Study of thermal residual stresses in ceramic matrix composites. *J Alloys Compounds* 1997; 259: 260-264.
- [97] Steen M. Tensile mastercurve of ceramic matrix composites: significance and implications for modeling. *Materials Science and Engineering: A* 1998; 250: 241-248.
- [98] Broda M, Pyzalla A, Reimers W. X-ray analysis of residual stresses in C/SiC composites. *Applied Composite Materials* 1999; 6: 51-66.
- [99] Bertrand S, Droillard C, Pailler R, Bourrat X, Naslain R. TEM structure of (PyC/SiC)<sub>n</sub> multi-layered interphases in SiC/SiC composites. *Journal of the European Ceramic Society* 2000; 20: 1-13.
- [100] Mei H. Measurement and calculation of thermal residual stress in fiber reinforced ceramic matrix composites. *Composites Science and Technology* 2008; 68: 3285-3292.
- [101] Bobet JL, Lamon J. Thermal residual stresses in ceramic matrix composites-I: axisymmetrical model and finite element analysis. *Acta Metallurgica et Materialia* 1995; 43(6): 2241-2253.
- [102] Bobet JL, Lamon J. Study of thermal residual stresses in ceramic matrix composites. *Journal of Alloys and Compounds* 1997; 259: 260-264.
- [103] Vena P. Thermal residual stresses in graded ceramic composites: a microscopic computational model versus homogenized models. *Meccanica* 2005; 40: 163-179.
- [104] Kennedy J, Eberhart RC. Particle swarm optimization. *Proceedings of the fourth IEEE international conference on neural networks*, 1995.

- [105] Fourie P, Groenwold A. The particle swarm optimization algorithm in size and shape optimization. *Structural and Multidisciplinary Optimization* 2002; 23(4): 259-267.
- [106] Trelea IC. The particle swarm optimization algorithm: convergence analysis and parameter selection. *Information Processing Letters* 2003; 85: 317-325.
- [107] Venter G, Sobieszczanski-Sobieski J. Multidisciplinary optimization of a transport aircraft wing using particle swarm optimization. *Structural and Multidisciplinary Optimization* 2004; 26(12): 121-131.
- [108] Elegbede C. Structural reliability assessment based on particles swarm optimization. *Struct Safety* 2005; 27(2):171-186.
- [109] Lee K, Geem Z. A new meta-heuristic algorithm for continuous engineering optimization: harmony search theory and practice. *Computer Methods in Applied Mechanics and Engineering* 2005; 194: 3902-3933.
- [110] Kathiravan R, Ganguli R. Strength design of composite beam using gradient and particle swarm optimization. *Composite Structures* 2007; 81: 471-479.
- [111] Suresh S, Sujit PB, Rao AK. Particle swarm optimization approach for multi-objective composite box-beam design. *Composite Structures* 2007; 81: 598-605.
- [112] Li L J, Huang ZB, Liu F, Wu QH. A heuristic particle swarm optimizer for optimization of pin connected structures. *Computers & Structures* 2007; 85: 340-349.
- [113] Chang N, Wang W, Yang W, Wang J. Ply stacking sequence optimization of composite laminate by permutation discrete particle swarm optimization. *Structural and Multidisciplinary Optimization* 2010; 41: 179-187.
- [114] Noda T, Araki H, Abe F, Okada M. Microstructure and mechanical properties of CVI carbon fiber/ SiC composites. *Journal of Nuclear Materials* 1992; 191-194: 539-543.
- [115] Geem ZW, Kim JH, Loganathan GV. A new heuristic optimization algorithm: harmony search. *Simulation* 2001; 76: 60-68.
- [116] Lee KS, Geem ZW. A new structural optimization method based on the harmony search algorithm. *Computers & Structures* 2004; 82: 781-798.
- [117] Puglia PD, Sheikh MA, Hayhurst DR. Classification and quantification of initial porosity in a CMC laminate. *Composites Part A* 2004; 35: 223-230.
- [118] Sheikh MA, Farooqi JK. Finite element modelling of thermal transport in ceramic

- matrix composites. Computational Materials Science 2006; 37: 361-373.
- [119] Lamouroux F, Bourrat X, Nasalain R, Sevely J. Structure/oxidation behavior relationship in the carbonaceous constituents of 2D C/PyC/SiC composites. Carbon 1993; 31: 1273-1288.
- [120] Clime WH, Cawley JD. Oxidation of carbon fibers and films in ceramic matrix composites: a weak link process. Carbon 1995; 33: 1053-1060.

## Scientific Publications

- [1] **Y. J. Xu**, W. H. Zhang, H. B. Wang. Prediction of Effective Elastic Modulus of Plain Weave Multi-phase and Multi-layer Silicon Carbide Ceramic Matrix Composite. *Materials Science and Technology*, 2008, 24(4): 435-442.
- [2] **Y. J. Xu**, W. H. Zhang, D. Bassir. Stress analysis of multi-phase and multi-layer plain weave composite structure using global-local approach. *Composite Structures*, 2010, 92(5): 1143-1154.
- [3] **Y. J. Xu**, W. H. Zhang, M. Domaszewski. Microstructure modelling and prediction of effective elastic properties of 3D multiphase and multilayer braided composite. *Materials Science and Technology*, accepted, in press.
- [4] H. B. Wang, W. H. Zhang, **Y. J. Xu**, Zeng QF. Numerical computing and experimental validation of effective elastic properties of 2D multilayered C/SiC composite. *Materials Science and Technology*, 2008, 24(11): 1385-1398.
- [5] T. Gao, W. H. Zhang, J. H. Zhu, **Y. J. Xu**, D. Bassir. Topology Optimization of Heat Conduction Problem Involving Design-dependent Heat Load Effect. *Finite Elements in Analysis and Design*, 2008, 44(14): 805-813.
- [6] **Y. J. Xu**, W. H. Zhang, D. Chamoret, M. Domaszewski. Minimizing Thermal Residual Stresses in Ceramic Matrix Composites by using Particle Swarm Optimization Algorithm. *The Second International Conference on Soft Computing Technology in Civil, Structural and Environmental Engineering*, Crete, Greece, 2011.
- [7] **Y. J. Xu**. Microstructure modeling and prediction of effective elastic properties of multi-phase and multi-layer woven/braided composite. *First Joint French-Dutch-Chinese Workshop on Composites Materials and Structures*, Delft, The Netherlands, 2009.
- [8] **Y. J. Xu**, W. H. Zhang, D. Bassir. Multi-objective optimization of thermal-elastic properties for multi-phase and multi-layer composite. *8th World Congress on Structural and Multidisciplinary Optimization*, Lisbon, Portugal, 2009.